

DOT/FAA/AR-xx/xx

Federal Aviation Administration
William J. Hughes Technical Center
Aviation Research Division
Atlantic City International Airport
New Jersey 08405



Annex C: Task A14 UAS Ground Collision Severity Evaluation, Ohio State University Final Report

Date 24 May 2019

Final Report

This document is available to the U.S. public through the National Technical Information Services (NTIS), Springfield, Virginia 22161.

This document is also available from the Federal Aviation Administration William J. Hughes Technical Center at actlibrary.tc.faa.gov.



U.S. Department of Transportation
Federal Aviation Administration

NOTICE

This document is disseminated under the sponsorship of the U.S. Department of Transportation in the interest of information exchange. The U.S. Government assumes no liability for the contents or use thereof. The U.S. Government does not endorse products or manufacturers. Trade or manufacturers' names appear herein solely because they are considered essential to the objective of this report. The findings and conclusions in this report are those of the author(s) and do not necessarily represent the views of the funding agency. This document does not constitute FAA policy. Consult the FAA sponsoring organization listed on the Technical Documentation page as to its use.

This report is available at the Federal Aviation Administration William J. Hughes Technical Center's Full-Text Technical Reports page: actlibrary.tc.faa.gov in Adobe Acrobat portable document format (PDF).

Legal Disclaimer: The information provided herein may include content supplied by third parties. Although the data and information contained herein has been produced or processed from sources believed to be reliable, the Federal Aviation Administration makes no warranty, expressed or implied, regarding the accuracy, adequacy, completeness, legality, reliability or usefulness of any information, conclusions or recommendations provided herein. Distribution of the information contained herein does not constitute an endorsement or warranty of the data or information provided herein by the Federal Aviation Administration or the U.S. Department of Transportation. Neither the Federal Aviation Administration nor the U.S. Department of Transportation shall be held liable for any improper or incorrect use of the information contained herein and assumes no responsibility for anyone's use of the information. The Federal Aviation Administration and U.S. Department of Transportation shall not be liable for any claim for any loss, harm, or other damages arising from access to or use of data or information, including without limitation any direct, indirect, incidental, exemplary, special or consequential damages, even if advised of the possibility of such damages. The Federal Aviation Administration shall not be liable to anyone for any decision made or action taken, or not taken, in reliance on the information contained herein.

ACKNOWLEDGEMENTS

OSU would like to acknowledge the significant help and support provided by research teams at the Injury Biomechanics Research Center and the Aerospace Research Center. The Ohio State research team acknowledges Zach Eshelman, Arrianna Willis, Dr. Yun-Seok Kang and Yadetsie Zaragoza-Rivera for their support during testing and cleanup days. Additionally, Angela Harden and Dr. Amanda Agnew of the Skeletal Biology Research Lab provided technical insight on fracture patterns and injury severities observed during testing. Finally, OSU would also like to recognize Dr. Matt McCrink, Josh Gueth and Noah Eckstein for their assistance in designing, installing and calibrating the UAS launcher.

TABLE OF CONTENTS

| | Page |
|--|------|
| 1. Introduction..... | 1 |
| 2. Materials & methods..... | 1 |
| 2.1 PMHS Subject Selection..... | 1 |
| 2.2 Test Matrix..... | 3 |
| 2.3 Instrumentation | 6 |
| 2.3.1 Subject Instrumentation | 6 |
| 2.3.1.1 Head Instrumentation..... | 7 |
| 2.3.1.2 Spine and Thorax Instrumentation..... | 9 |
| 2.3.2 Test Article Instrumentation | 10 |
| 2.4 Test Setup..... | 11 |
| 2.5 Data Collection & Analysis | 13 |
| 2.5.1 Hardware..... | 13 |
| 2.5.2 Data Processing..... | 13 |
| 2.5.3 Injury Criteria Selection..... | 15 |
| 2.5.4 Autopsy | 17 |
| 2.5.4.1 Abbreviated Injury Scale (AIS) Background..... | 18 |
| 3. Results..... | 20 |
| 3.1 Injuries | 20 |
| 3.2 Head Kinematics..... | 22 |
| 3.3 Head & Brain Injury Risk..... | 27 |
| 4. Discussion..... | 33 |
| 4.1 PMHS Injuries | 33 |
| 4.2 Head Injury Risk Thresholds & Limits..... | 33 |
| 4.3 Concussion Risk Assessment..... | 34 |
| 4.4 UAS Vehicle Risk Comparison | 34 |
| 4.5 UAS Impact Variation | 35 |
| 4.6 Skull Deformation..... | 39 |
| 5. Limitations | 42 |
| 6. Conclusions & Recommendations..... | 42 |
| APPENDIX A— Impact Response Still Images | 45 |

APPENDIX B— Subject Head Kinematic Time Histories 48
APPENDIX C— UAS Impact Orientation Angles 60
APPENDIX D— Faro Measurment Locations..... 61

LIST OF FIGURES

| Figure | Page |
|--|------|
| Figure 1 – Head anthropometrical measurements taken from CT scan data | 2 |
| Figure 2 – Subject instrumentation overview | 6 |
| Figure 3 – PMHS cranial strain gage locations | 7 |
| Figure 4 – PMHS cranial Vicon marker locations..... | 7 |
| Figure 5 – 6a ω tetrahedron sensor array (a) mounted, (b) close-up..... | 8 |
| Figure 6 – 6a ω tetrahedron & 3a ω array mounted on PMHS03 | 9 |
| Figure 7 – (a) “Cinch” instrumentation technique on C-spine of PMHS03 (b) “Cinch” technique schematic..... | 10 |
| Figure 8 – Chalk paint on (a) drone pre-test, (b) PMHS post-test..... | 10 |
| Figure 9 – Chair and subject setup..... | 11 |
| Figure 10 – (a) Test setup representation, (b) UAS launcher | 12 |
| Figure 11 – Pre-test lateral X-Ray images of subject #4 (a) skull, and (b) cervical spine | 13 |
| Figure 12 – Original and “corrected” Vicon coordinate system on DJI Phantom 3..... | 14 |
| Figure 13 – Vertebral body local coordinate system | 15 |
| Figure 14 – Head CG measurement schematic..... | 17 |
| Figure 15 – Example AIS 3+ injury risk curve..... | 19 |
| Figure 16 – PMHS03, 5.1 inch linear skull fracture | 20 |
| Figure 17 – Strain rate time histories for all tests conducted on PMHS02, and PMHS03 | 21 |
| Figure 18 – Skeletal injuries sustained by PMHS05, (a) comminuted fracture of frontal bone, (b) comminuted fractures of the temporal and parietal bones, (c) lateral wall fracture of right orbit, (d) basilar skull fracture, viewed from inferior to superior..... | 21 |
| Figure 19 – Impact response of PMHS and Phantom 3 during a 71 ft/s, 0-degree, right side impact, [10 millisecond time steps] (Test: OSU #4)..... | 23 |
| Figure 20 – Resultant CG head linear acceleration time histories in 0-degree, side impact scenarios..... | 23 |
| Figure 21 – Resultant head angular velocity time histories in 0-degree, side impact scenarios... .. | 24 |
| Figure 22 – Resultant head angular acceleration time histories in 0-degree, side impact scenarios Note: Wood Block time history not included due to its high angular acceleration magnitude | 24 |
| Figure 23 – HIC values for all impacts. Note: Injurious HIC values are tests in which impacts resulted in an AIS2+ skull fracture | 27 |
| Figure 24 – BrIC values for all impacts..... | 28 |

Figure 25 – VT-CP values for all impacts 29

Figure 26 – Comparison of AIS 2+ level skull fracture risk and PMHS test data..... 31

Figure 27 – Comparison of AIS 3+ level head injury risk and PMHS test data..... 31

Figure 28 – Comparison of AIS 3 level brain injury risk and PMHS test data 32

Figure 29 – Comparison of concussion risk gradients and PMHS test data..... 32

Figure 30 – Impact location variation relative to PMHS CG for 58-degree, Phantom 3 impacts 36

Figure 31 – Impact location variation relative to PMHS CG for 90-degree, Phantom 3 impacts 37

Figure 32 – UAS impact pitch angle variation for 58-degree, Phantom 3 impacts 38

Figure 33 – UAS impact yaw angle variation for 58-degree, Mavic Pro impacts..... 38

Figure 34 – Comparison between $6a\omega$ tetrahedron array and redundant $3a\omega$ array (a) from smallest to largest percent difference, (b) averaged by impact direction 40

Figure 35 – Approximate locations of $6a\omega$ array and $3a\omega$ for PMHS tests 41

Figure 36 – Comparison of UAS impacts to previously published head injury studies 42

Figure 37 - Impact response of PMHS and Phantom 3 during a 58 degree, 71 ft/s, frontal impact, [5 millisecond time steps] (Test: OSU #9) 45

Figure 38 - Impact response of PMHS and Phantom 3 during a 90 degree, 71 ft/s, top impact, [10 millisecond time steps] (Test: OSU #15)..... 45

Figure 39 - Impact response of PMHS and Inspire 2 (Parachute) during a 0 degree, 30 ft/s, right side impact, [10 millisecond time steps] (Test: OSU #30) 46

Figure 40 - Impact response of PMHS and eBee+ during a 0 degree, 71 ft/s, right side impact, [10 millisecond time steps] (Test: OSU #25) 46

Figure 41 - Impact response of PMHS and Mavic Pro during a 58 degree, 71 ft/s frontal impact, [10 millisecond time steps] (Test: OSU #21) 47

Figure 42 - Impact response of PMHS and Wood Block during a 0 degree, 40 ft/s right side impact, [5 millisecond time steps] (Test: OSU #33)..... 47

Figure 43 – Head resultant linear acceleration time histories in 58-degree, Phantom 3 frontal impact scenarios..... 48

Figure 44 – Head resultant angular velocity time histories in 58-degree, Phantom 3 frontal impact scenarios..... 48

Figure 45 – Head resultant angular acceleration time histories in 58-degree, Phantom 3 frontal impact scenarios..... 49

Figure 46 – Head resultant linear acceleration time histories in 58-degree, Mavic Pro frontal impact scenarios..... 49

Figure 47 – Head resultant angular velocity time histories in 58-degree, Mavic Pro frontal impact scenarios..... 50

Figure 48 – Head resultant angular acceleration time histories in 58-degree, Mavic Pro frontal impact scenarios..... 50

Figure 49 – Head resultant linear acceleration time histories in 58-degree, Phantom 3 right side impact scenarios..... 51

Figure 50 – Head resultant angular velocity time histories in 58-degree, Phantom 3 right side impact scenarios..... 51

Figure 51 – Head resultant angular acceleration time histories in 58-degree, Phantom 3 right side impact scenarios..... 52

Figure 52 – Head resultant linear acceleration time histories in 58-degree, eBee+ left side impact scenarios..... 52

Figure 53 – Head resultant angular velocity time histories in 58-degree, eBee+ left side impact scenarios..... 53

Figure 54 – Head resultant angular acceleration time histories in 58-degree, eBee+ left side impact scenarios..... 53

Figure 55 – Head resultant linear acceleration time histories in 0-degree, low speed, right side impact scenarios..... 54

Figure 56 – Head resultant angular velocity time histories in 0-degree, low speed, right side impact scenarios..... 54

Figure 57 – Head resultant angular acceleration time histories in 0-degree, low speed, right side impact scenarios..... 55

Figure 58 – Head resultant linear acceleration time histories in 0-degree, wood & foam block side impact scenarios 55

Figure 59 – Head resultant angular velocity time histories in 0-degree, wood & foam block side impact scenarios..... 56

Figure 60 – Head resultant angular acceleration time histories in 0-degree, wood & foam block side impact scenarios 56

Figure 61 – Head resultant linear acceleration time histories in 90-degree, Phantom 3, top impact scenarios..... 57

Figure 62 – Head resultant angular velocity time histories in 90-degree, Phantom 3, top impact scenarios..... 57

Figure 63 – Head resultant angular acceleration time histories in 90-degree, Phantom 3, top impact scenarios..... 58

Figure 64 – Head resultant linear acceleration time histories in 90-degree, Vendor 1, top impact scenarios..... 58

Figure 65 – Head resultant angular velocity time histories in 90-degree, Vendor 1, top impact scenarios..... 59

Figure 66 – Head resultant angular acceleration time histories in 90-degree, Vendor 1, top impact scenarios..... 59

LIST OF TABLES

| Table | Page |
|---|------|
| Table 1 – PMHS summary information..... | 2 |
| Table 2 – PMHS head anthropometry | 3 |
| Table 3 – Test article impact matrix | 4 |
| Table 4 – Test matrix | 5 |
| Table 5 – Head kinematic normalization factors | 15 |
| Table 6 – AIS Severity Scale | 18 |
| Table 7 – Summary of PMHS injuries..... | 22 |
| Table 8 – Peak head kinematics for all tests articles, categorized by impact direction..... | 26 |
| Table 9 – Injury criteria values for Phantom 3 impacts..... | 30 |
| Table 10 – Average (SD) injury criteria values by UAS vehicle | 35 |
| Table 11 – Comparison between UAS impact orientation/location and head kinematics..... | 39 |
| Table 12 – Change in UAS orientation between its release from the launcher and impact | 60 |

LIST OF ACRONYMS

| | |
|-------------|---|
| 3a ω | Three linear accelerometers and three angular rate sensors in an orthogonal array |
| 6a ω | Six linear accelerometers and three angular rate sensors attached to a tetrahedron fixture, used to measure linear acceleration, angular velocity, and used to algebraically calculate angular acceleration |
| aBMD | Areal bone mineral density |
| AIS | Abbreviated Injury Scale |
| BrIC | Brain Injury Criterion |
| CG | Center of Gravity |
| CT | Computed tomography scan, also known as CAT scan |
| HIC | Head injury Criterion |
| KE | Kinetic energy of the UAS vehicle just prior to impact |
| OSU | The Ohio State University |
| PMHS | Post Mortem Human Surrogate |
| UAS | Unmanned Aerial System |
| VT-CP | Virginia Tech Combined Probability of Concussion |

EXECUTIVE SUMMARY

As a part of the Task A14 UAS Ground Collision Severity Evaluation, the Injury Biomechanics Research Center at Ohio State University conducted full body PMHS-UAS impact tests. PMHS testing was conducted to evaluate the risk of injury associated with UAS impacts of the human cranium. A total of 41 impact tests were conducted on five PMHS subjects over the course of the project. Impacts were conducted at multiple angles and impact locations with five different UAS vehicles, both quadcopter and fixed wing. PMHS subjects were instrumented with sensors to measure impact response. These impact dynamics were related to injuries observed in testing using published injury criteria. Of the 35 impacts carried out with UAS vehicles, one skeletal injury was observed: a skull fracture of the frontal bone. Additionally, according to published injury criteria, many impacts had a high probability of causing skeletal injury, yet only one was observed. These results indicate that UAS impacts in “worst-case” scenarios may result in serious injury. Additionally, more investigation is needed to develop an appropriate criterion for predicting the severity of head injuries in UAS impact scenarios.

1. INTRODUCTION

To investigate the risk of physical injury associated with UAS-human impacts, A series of five whole body Post-Mortem Human Surrogate (PMHS) tests, with 41 total impacts were conducted over the duration of this project. Testing involved accelerating multiple UAS vehicle models in to PMHS craniums, followed by autopsy to identify injury. Additionally, PMHS were instrumented with sensors to measure accelerations and stresses which occurred due to the impacts. These tests served as the basis for validating the human body modeling work conducted in Tasks B and C as well as for validating the injury thresholds established as a part of Task A. Additionally, test data were compared to published injury metrics to assess the efficacy of previously derived criteria in this particular impact scenario.

2. MATERIALS & METHODS

Five separate PMHS were used for testing, with each PMHS receiving between 6 and 11 impacts, yielding a total of 41 individual test points. Impacts were carried out with 5 different UAS vehicles and 2 payloads, these included: the DJI Phantom 3, DJI Mavic Pro, DJI Inspire 2, Sensefly eBee+, Vendor 1, Wood Block and Foam Block. Impacts were carried out at either 0, 58 or 90-degree trajectory angles, with impacts directed to either the front, side or top of each subject's head. Further detail regarding PMHS subject selection, sensor instrumentation, and data reduction is given in the following sections.

2.1 PMHS Subject Selection

Subjects selected for the study were approximately 50th percentile males with height and weight inclusion limits set between 65-73 inches and 165-218 lbs, respectively. Subjects meeting the height and weight criteria were subsequently scanned for their areal bone mineral density (aBMD) using dual-energy x-ray absorptiometry. Accepted subjects were restricted to be within the average to above-average range for total body aBMD scores (t-score: -1.0 to 2.0). Upon completion of the aBMD scans, subjects were inspected for other pre-existing injuries or abnormalities using a full-body computed tomography (CT) scan. Finally, CT scan data were used to take several head anthropometrical measurements to ensure average characteristics were met. These measurements included: head height, head circumference, and skull bone thickness of the frontal, parietal and occipital regions. A summary of each subject's age, anthropometrical measurements, and aBMD score are given in the Table 1 and

Table 2.

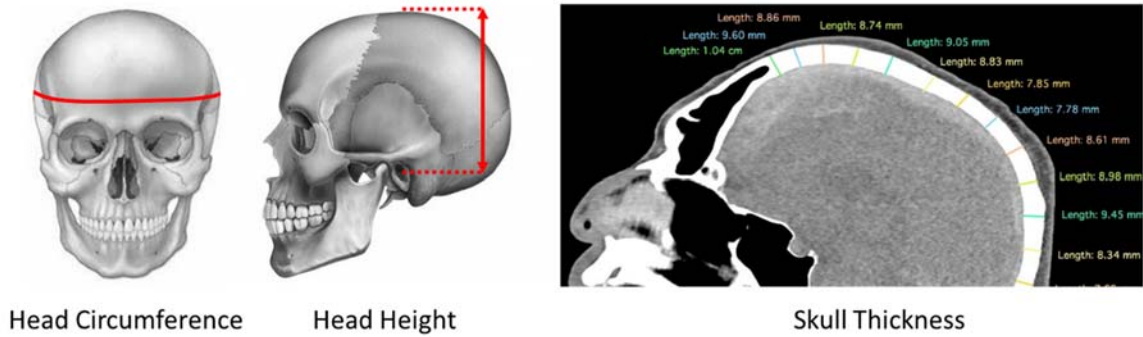


Figure 1 – Head anthropometrical measurements taken from CT scan data

Table 1 – PMHS summary information

| Subject # | Age | Standing Height (inch) | Body Mass (lb) | Total Body aBMD t-Score |
|-----------------------------------|-----------------|------------------------|------------------------|-------------------------|
| 01 | 60 | 70 | 170 | -0.2 |
| 02 | 73 | 66 | 163 | 0.3 |
| 03 | 67 | 71 | 143 | 1.2 |
| 04 | 67 | 72 | 193 | 1.1 |
| 05 | 74 | 74 | 195 | 0.4 |
| Average | 68 ± 5.6 | 70.6 ± 3.0 | 172.8 ± 21.8 | 0.56 ± 0.6 |
| 50th Percentile | 45 | 69^a | 172^a | 0 |

^aMertz, H. J., Jarrett, K., Moss, S., Salloum, M., & Zhao, Y. (2001). *The Hybrid III 10-year-old dummy* (No. 2001-22-0014). SAE Technical Paper.

Table 2 – PMHS head anthropometry

| Subject # | Head Circ. (inch) | Head Height (inch) | Skull Thickness Frontal Bone (inch) | Skull Thickness Parietal Bone (inch) | Skull Thickness Occipital Bone (inch) |
|---------------------------------------|-------------------------|------------------------|---|--|---|
| 01 | 22.7 | 5.3 | 0.33 | 0.30 | 0.35 |
| 02 | 22.7 | 5.1 | 0.39 | 0.28 | 0.28 |
| 03 | 22.1 | 5.3 | 0.34 | 0.37 | 0.44 |
| 04 | 22.3 | 5.1 | 0.36 | 0.31 | 0.37 |
| 05 | 22.9 | 5.2 | 0.35 | 0.31 | 0.33 |
| Average | 22.5 ± 0.3 | 5.20 ± 0.1 | 0.35 ± 0.03 | 0.32 ± 0.03 | 0.36 ± 0.06 |
| 50th Percentile | 22.6^b | 5.2^b | 0.36^c | 0.32^c | 0.36^c |

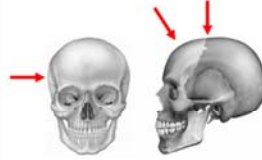
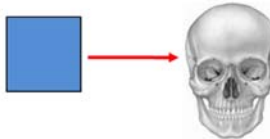
^bPaquette, S., Gordon, C., & Bradtmiller, B. (2009). *Anthropometric survey (ANSUR) II pilot study: methods and summary statistics*. Anthrotech Yellow Springs, OH.

^cOhio State internal study of ten 50th percentile male subjects within the lab's CT database.

2.2 Test Matrix

Seven different test articles were selected for PMHS testing, these included five UAS vehicles and two payloads. The UAS vehicle tests included: 21 DJI Phantom 3 tests, 4 DJI Mavic Pro tests, 5 Sensefly eBee+ tests, 4 Vendor 1 tests, 1 DJI Inspire 2* test, 3 Wood Block tests and 3 Foam Block tests. Each test article was tested in the “worst case” impact orientation defined in Tasks A and B; however, many articles were tested at multiple impact angles, multiple head impact locations, and multiple impact speeds, as detailed in Table 4. Impact angles varied between 0, 58 and 90 degrees, while impact speeds ranged from 56 to 71 ft/s. All impacts were directed as close as possible to the head center of gravity. Details pertaining to each test ran during this study are available in Table 3.

Table 3 – Test article impact matrix

| Test Article | Impact Orientation | Impact Location(s) | Impact Angle(s) | Impact Speed(s) |
|-----------------|---|--|------------------|--|
| DJI Phantom 3 |  |  | 0° 58° 90° | 56 ft/s 61 ft/s 65 ft/s 71 ft/s |
| DJI Mavic Pro |  |  | 58° | 61 ft/s 71 ft/s |
| Sensefly eBee+ |  |  | 0° 58° | 64 ft/s 71 ft/s |
| Vendor 1 | N/A |  | 0° 58° 90° | 70 ft/s |
| DJI Inspire 2* |  |  | 0° | 30 ft/s |
| Foam/Wood Block |  |  | 0° | 20 ft/s 30 ft/s 40 ft/s |

 UAS Impact Location  Impact Trajectory

Table 4 – Test matrix

| PMHS # | Test ID | Test Article | Impact Angle | Impact Location | Target Impact Speed (ft/s) | Achieved Impact Speed (ft/s) | Article Mass (lb) | Impact Kinetic Energy (ft-lb) |
|--------|----------|----------------|--------------|-----------------|----------------------------|------------------------------|-------------------|-------------------------------|
| 01 | OSU #1 | Vendor 1 | 0 | Right Side | 70 | 70.9 | 0.73 | 57.0 |
| | OSU #2 | DJI Phantom 3 | 0 | Right Side | 56 | 55.1 | 2.67 | 125.9 |
| | OSU #3 | DJI Phantom 3 | 0 | Right Side | 61 | 60.1 | 2.67 | 149.8 |
| | OSU #4 | DJI Phantom 3 | 0 | Right Side | 71 | 69.2 | 2.67 | 198.5 |
| | OSU #5 | Vendor 1 | 58 | Front | 70 | 74.6 | 0.73 | 63.1 |
| | OSU #6 | DJI Phantom 3 | 58 | Front | 56 | 57.3 | 2.67 | 136.1 |
| | OSU #7 | DJI Phantom 3 | 58 | Front | 61 | 61.4 | 2.67 | 156.3 |
| 02 | OSU #8 | DJI Phantom 3 | 58 | Front | 61 | 59.2 | 2.67 | 145.3 |
| | OSU #8a | DJI Phantom 3 | 58 | Front | 61 | 59.9 | 2.66 | 147.9 |
| | OSU #9 | DJI Phantom 3 | 58 | Front | 71 | 70.1 | 2.68 | 204.8 |
| | OSU #10 | DJI Phantom 3 | 58 | Right Side | 61 | 61.2 | 2.61 | 151.5 |
| | OSU #11 | DJI Phantom 3 | 58 | Right Side | 71 | 71.8 | 2.60 | 208.5 |
| | OSU #11a | DJI Phantom 3 | 58 | Right Side | 71 | 71.9 | 2.56 | 205.3 |
| | OSU #13 | DJI Phantom 3 | 90 | Top | 56 | 55.2 | 2.48 | 117.5 |
| 03 | OSU #14 | DJI Phantom 3 | 90 | Top | 65 | 63.9 | 2.54 | 161.0 |
| | OSU #15 | DJI Phantom 3 | 90 | Top | 71 | 70.5 | 2.53 | 195.6 |
| | OSU #16 | DJI Phantom 3 | 58 | Right Side | 61 | 61.4 | 2.44 | 143.0 |
| | OSU #16a | DJI Phantom 3 | 58 | Right Side | 61 | 60.9 | 2.47 | 142.2 |
| | OSU #17 | DJI Phantom 3 | 58 | Right Side | 71 | 72 | 2.60 | 209.1 |
| | OSU #18 | DJI Phantom 3 | 58 | Front | 61 | 61.2 | 2.59 | 150.7 |
| | OSU #19 | DJI Phantom 3 | 58 | Front | 71 | 71.8 | 2.47 | 197.6 |
| 04 | OSU #20 | DJI Mavic Pro | 58 | Front | 61 | 59.6 | 1.60 | 88.5 |
| | OSU #21 | DJI Mavic Pro | 58 | Front | 71 | 69.9 | 1.61 | 121.8 |
| | OSU #12 | Vendor 1 | 90 | Top | 70 | 69.1 | 0.77 | 56.8 |
| | OSU #12a | Vendor 1 | 90 | Top | 70 | 69.3 | 0.77 | 57.2 |
| | OSU #22 | DJI Phantom 3 | 90 | Top | 65 | 64.5 | 2.60 | 167.8 |
| 04 | OSU #23 | DJI Phantom 3 | 90 | Top | 71 | 70.5 | 2.58 | 198.8 |
| | OSU #24 | Sensefly eBee+ | 0 | Right Side | 64 | 60.5 | 2.48 | 140.8 |
| | OSU #25 | Sensefly eBee+ | 0 | Right Side | 71 | 70.6 | 2.43 | 187.8 |

| | | | | | | | | |
|----|----------|----------------|----|------------|----|------|------|-------|
| | OSU #30 | DJI Inspire 2* | 0 | Right Side | 30 | 31.4 | 9.59 | 146.9 |
| | OSU #26 | Sensefly eBee+ | 58 | Left Side | 64 | 61.5 | 2.48 | 145.8 |
| | OSU #27 | Sensefly eBee+ | 58 | Left Side | 71 | 70.2 | 2.45 | 187.8 |
| | OSU #27a | Sensefly eBee+ | 58 | Left Side | 71 | 69.6 | 2.47 | 185.9 |
| | OSU #28 | DJI Mavic Pro | 58 | Front | 61 | 58.8 | 1.58 | 85.0 |
| | OSU #29 | DJI Mavic Pro | 58 | Front | 71 | 69.2 | 1.61 | 119.9 |
| 05 | OSU #31 | Block, Wood | 0 | Right Side | 20 | 18.8 | 2.81 | 15.4 |
| | OSU #32 | Block, Wood | 0 | Right Side | 30 | 30.2 | 2.81 | 39.8 |
| | OSU #33 | Block, Wood | 0 | Right Side | 40 | 39.6 | 2.81 | 68.4 |
| | OSU #34 | Block, Foam | 0 | Left Side | 20 | 20.5 | 2.78 | 18.1 |
| | OSU #35 | Block, Foam | 0 | Left Side | 30 | 29.4 | 2.76 | 37.0 |
| | OSU #36 | Block, Foam | 0 | Left Side | 40 | 41 | 2.75 | 71.7 |

* Inspire 2 test conducted at “worst-case” decent rate speed with parachute

2.3 Instrumentation

2.3.1 Subject Instrumentation

Each subject was instrumented with strain gages, Vicon markers, 3 ω sensor arrays and a 6 ω tetrahedron array. An overview of the subject instrumentation locations is shown in Figure 2.

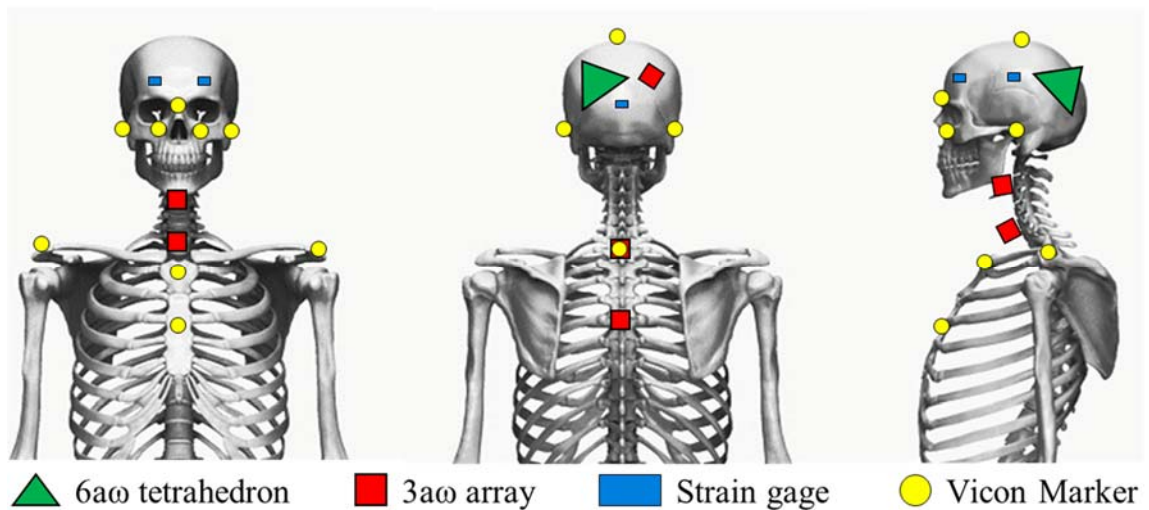


Figure 2 – Subject instrumentation overview

2.3.1.1 Head Instrumentation

Five uniaxial strain gages (CEA-13-250UW-350/P2, Micro Measurements, Wendell NC) were mounted throughout the calvarium, their approximate locations are displayed in Figure 3. Strain gages were mounted on the lateral aspects of the frontal bone, inferior aspects of both parietal bones, and mid-sagittally on the occipital bone. For PMHS04 and PMHS05, the occipital bone strain gage was moved to the midsagittal location on the frontal bone and oriented perpendicular to the Frankfurt plane. All other strain gages were approximately parallel with the Frankfurt plane. Strain gage readings were used to determine the strain distribution throughout the skull during impact as well as to determine if skull fracture occurred. The instrumented locations were sutured closed prior to testing.

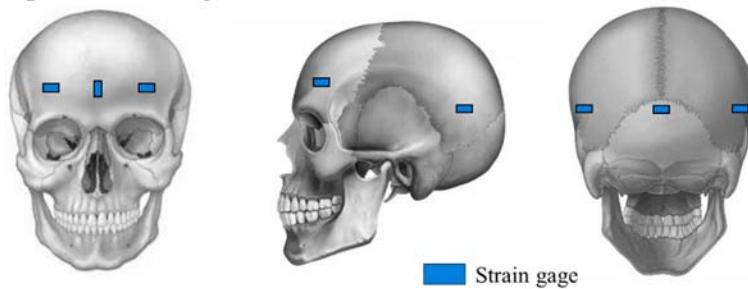


Figure 3 – PMHS cranial strain gage locations

Figure 4 displays the locations of the six Vicon motion tracking markers (Oxford Metrix, Oxford, UK) which were mounted on the cranium to measure the global displacement and orientation of the head upon impact. Marker mounts were attached to the maxilla, just below both left and right infraorbital notches. Mounts were also attached on each subject's nasion and mandible, mid-sagittally. On the calvarium, markers were attached the left and right trignon as well as the skull vertex using cyanoacrylate adhesive.

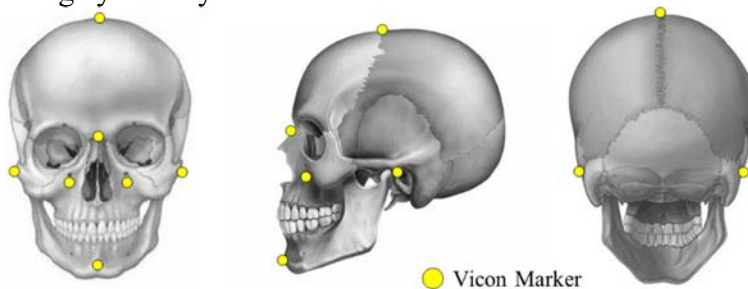


Figure 4 – PMHS cranial Vicon marker locations

A 6 ω tetrahedron sensor array was rigidly attached to each subject's skull to measure six degree-of-freedom head kinematics.¹ The 6 ω array, shown in Figure 5(b), contains three orthogonal faces, each face containing 2 accelerometers (7264C-2K, Endevco, Irvine CA) and one angular rate sensor (ARS-PRO-18K, Diversified Technical Systems, Seal Beach, CA). Three of

¹ Kang, Y. S., Moorhouse, K., & Bolte IV, J. H. (2015, June). Instrumentation technique for measuring six degrees of freedom head kinematics... In 24th International Technical Conference on the Enhanced Safety of Vehicles (ESV) (pp. 8-11).

the accelerometers are centered at the vertex of the tetrahedron while the other three are at specific locations away from the vertex. These isolated accelerometers allow for direct calculation of angular acceleration kinematics.² The 6ω array was attached to each subject's skull using six screws, as shown in Figure 5(a).

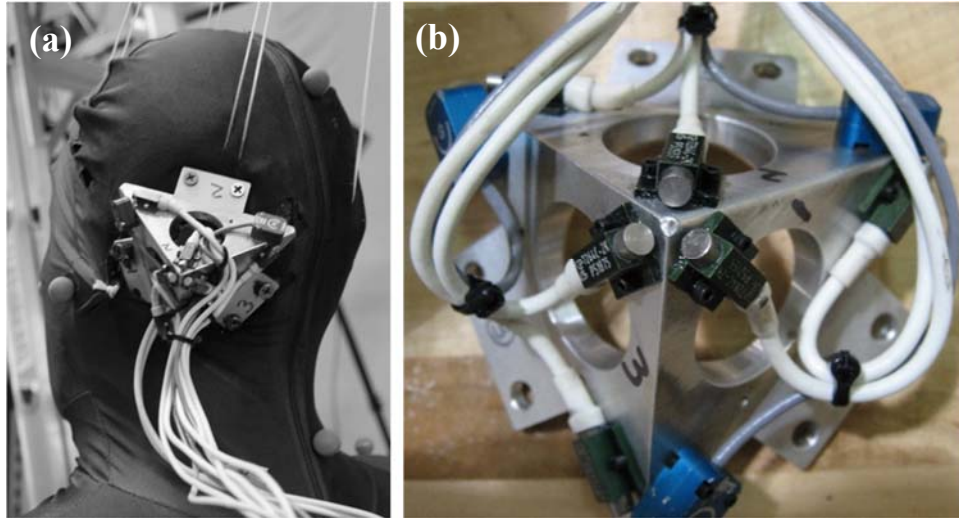


Figure 5 – 6ω tetrahedron sensor array (a) mounted, (b) close-up

In addition to the 6ω tetrahedron array, a 3ω array (6DX Pro, Model 2000g 18K deg/sec, DTS, Seal Beach CA) was also attached the skull as a redundant measure for PMHS 03,04 and 05. Locations of the two sensor arrays on the cranium are shown in Figure 6. This redundant sensor provided a means of validation for the 6ω array, while also serving as a backup measurement in case the larger footprint of the 6ω array was contacted by the test article during the event. However, the 3ω array does not have the capability to directly calculate angular acceleration; differentiation of angular rate data must be used, which can lead to numerical differentiation error.³

² Yoganandan, N., Zhang, J., Pintar, F. A., & Liu, Y. K. (2006). Lightweight low-profile nine-accelerometer package to obtain head angular accelerations in short-duration impacts. *Journal of biomechanics*, 39(7), 1347-1354.

³ Kang, Y. S., Moorhouse, K., & Bolte, J. H. (2011). Measurement of six degrees of freedom head kinematics in impact conditions employing six accelerometers and three angular rate sensors (6ω configuration). *Journal of biomechanical engineering*, 133(11), 111007.

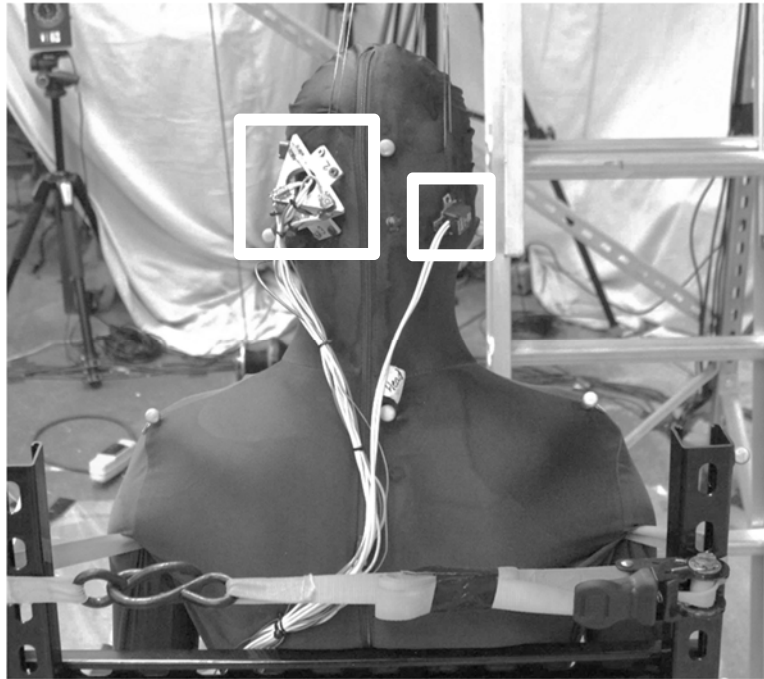


Figure 6 – 6 ω tetrahedron & 3 ω array mounted on PMHS03

2.3.1.2 Spine and Thorax Instrumentation

Subjects were instrumented with 3 ω arrays on the 3rd and 6th cervical vertebrae, as well as the 1st and 4th thoracic vertebrae. Sensor arrays on C3 and C6 vertebrae were attached by dissecting to the retropharyngeal space from the lateral aspect of the neck, providing access to the cervical vertebral bodies without disturbing neck musculature. Cervical spine sensors were mounted using a “cinch” technique in which cable ties were fed around the vertebral body, through the intervertebral foramen, and through a slot in the instrumentation mount, as shown in Figure 7. Cable ties around the vertebra and instrumentation mount were cinched to secure the 3 ω sensor to the vertebra without causing damage. 3 ω sensors were mounted to the thoracic vertebrae posteriorly by removing the vertebra’s spinous process and using a “U-mount” seated on the lamina to secure the sensor to the vertebral body. Five Vicon markers were also attached to each subject’s acromion (left, right), sternum, manubrium and T1 vertebrae. All instrumentation incision sites were sutured closed prior to testing. Spine sensors were used to document the motion of each subject’s cervical and thoracic spine during the event as well as monitor for cervical spine injury. Thoracic Vicon data were used to ensure subjects remained well constrained during impacts.

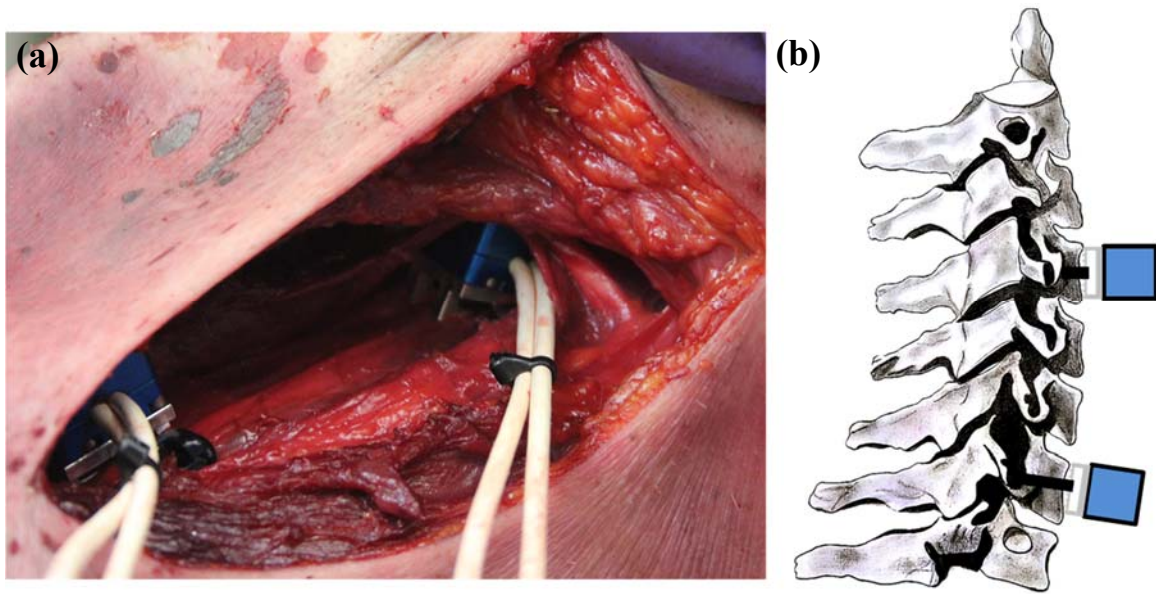


Figure 7 – (a) “Cinch” instrumentation technique on C-spine of PMHS03 (b) “Cinch” technique schematic

2.3.2 Test Article Instrumentation

Each test article was instrumented with Vicon markers, fiducial targets and chalk paint. At least 4 Vicon markers were attached to every test article using double-sided adhesive. The Vicon markers were used to define the impact trajectory, orientation and speed of the article prior to impact with the PMHS. Fiducial targets were used as a redundant measure for capturing test article trajectory and speed using high speed video tracking. Finally, chalk paint was applied to the impacting surface of each test article. Upon impact, the paint chalk was transferred to the PMHS revealing the impact location, this provided a qualitative measure of impact location, as illustrated in Figure 8.

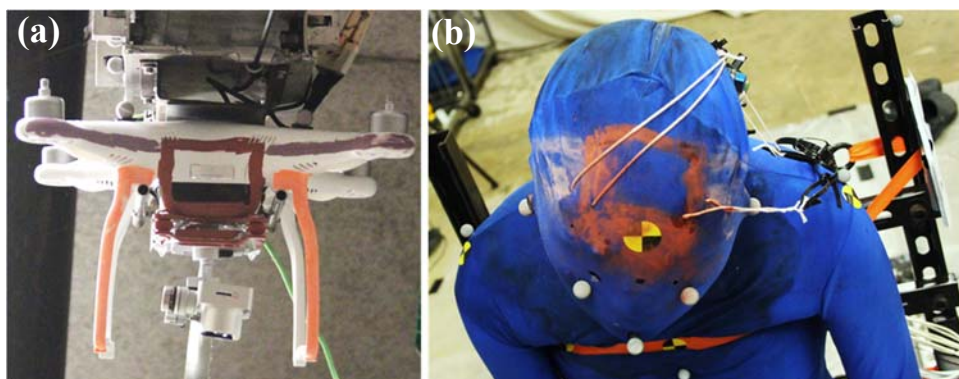


Figure 8 – Chalk paint on (a) drone pre-test, (b) PMHS post-test

2.4 Test Setup

Upon arriving at the testing facility, subjects were seated in a rigid chair, shown in Figure 9. The chair back support was 90° relative to the seat pan. The back support was made up of strut channel which provided support at the pelvis, mid-lumbar spine, and inferior thoracic spine, just below the inferior angle of the scapula. Additionally, the chair allowed for rotation about the Z-axis, as well as translation in X, Y and Z directions. This ensured that once the subject was seated, the pelvis, lumbar spine and thoracic spine remained in a constant position across tests.

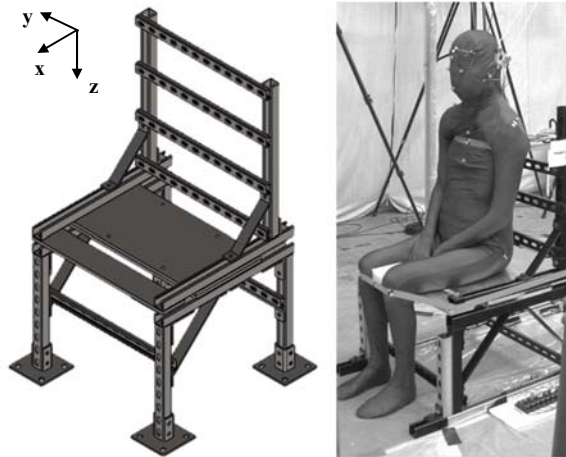


Figure 9 – Chair and subject setup

After seating, subjects were restrained at the patella and axilla using tie-down straps. Straps were inspected between tests to ensure no changes in location or tension had occurred. Each subject's head and neck were kept in a neutral, level posture prior to conducting each test. Subjects' head positions were adjusted such that their Frankfurt plane angle was within ± 5 degrees of neutral. Subjects' cervical spine angles were adjusted to ensure a natural cervical spine curvature. Spinal curvature was inspected both visually as well as with pre-test X-rays. Approximately 30 milliseconds before impact, subjects' heads were released using a custom designed head release system. The head release used for each subject consisted of a rotary quick release latch which was actuated by a solenoid. The release mechanism was triggered prior to impact using a relay circuit which monitored the position of the test article relative to the desired impact point.

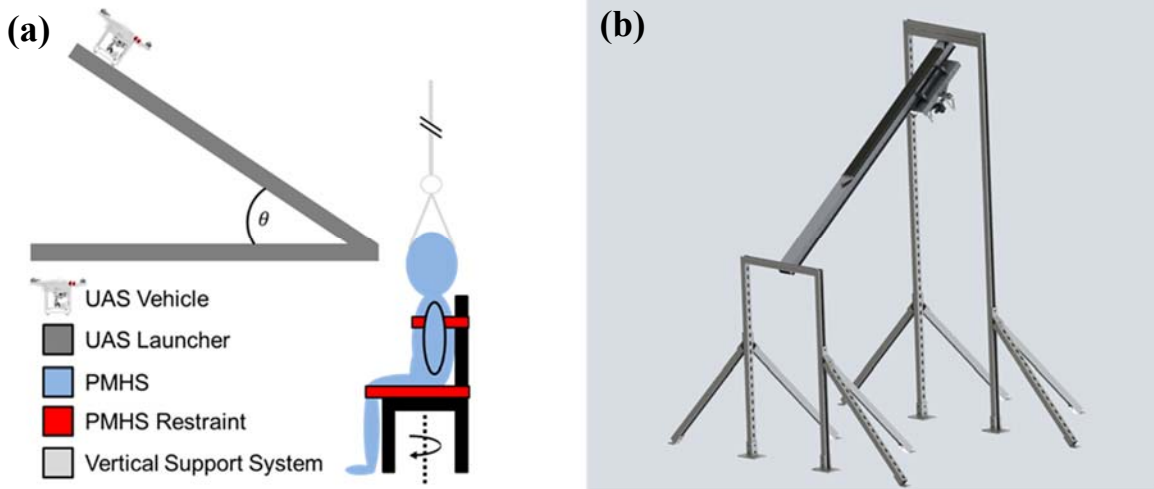


Figure 10 – (a) Test setup representation, (b) UAS launcher

UAS vehicles were accelerated in to test subjects using a custom UAS launcher, shown in Figure 10(b). The launcher utilized elastic bands to accelerate both the carriage and test article along an 8-foot track. Within the carriage, each test article was constrained to ensure correct alignment with the desired impact location on the PMHS. Alignment between the subject and launcher was ensured using two lasers: one laser pointer along the track of the launcher and one laser line generator perpendicular to the launcher track. All UAS were weighed prior to testing. Additionally, quadcopter UAS were tested without rotors and all ailerons were constrained on fixed wing UAS.

Prior to each test, a Faro arm (Faro Arm Technologies, Lake Mary, FL) was used to define 3D coordinates of all instrumentation locations, bony landmarks, and fixture landmarks, these locations are given in 6. APPENDIX D—. Additionally, prior to the first test, X-ray images of each subject's skull and cervical spine were taken using a mobile X-ray system (Ecotron Mobile X-ray EPX-F2800, Seoul, Korea). Example X-ray images are displayed in Figure 11. Additional X-rays were taken after severe impacts to monitor for injuries.

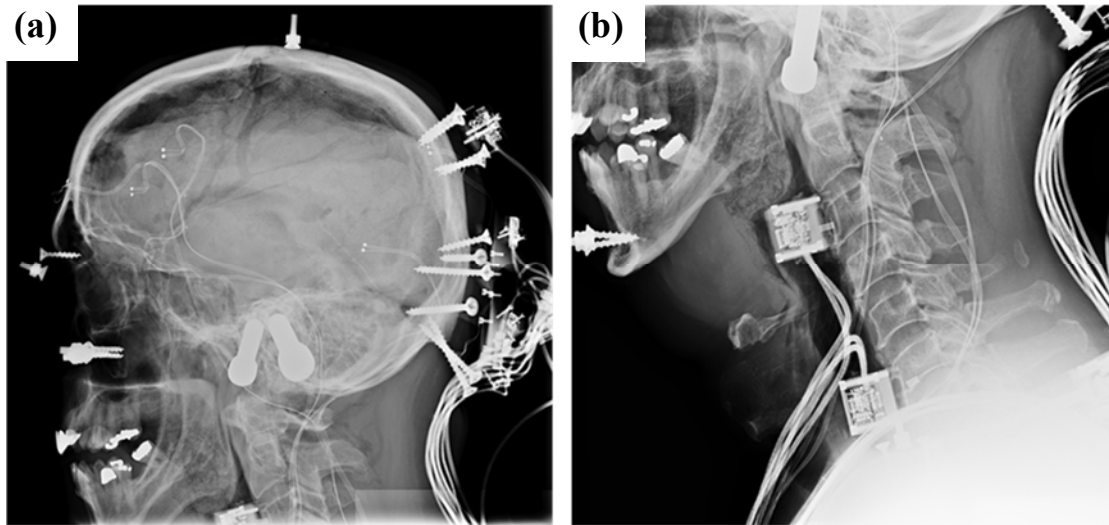


Figure 11 – Pre-test lateral X-Ray images of subject #4 (a) skull, and (b) cervical spine

2.5 Data Collection & Analysis

2.5.1 Hardware

All data from strain gages, 3 ω arrays and the 6 ω tetrahedron array were collected using a Slicepro data acquisition system (DTS, Seal Beach, CA) sampling at 100,000 Hz. Vicon data were recorded using 16 Vicon Vantage V5 Cameras (Oxford Metrics, Oxford, UK). Motion tracking data was collected using the Vicon Nexus Version 2.6 Software at a sampling rate of 1,000 Hz. In addition to the data acquisition systems, two high speed cameras (Phantom VEO 710L & Miro 320s, AMETEK Inc., Wayne, NJ) were used to record each test. Cameras were oriented both perpendicular, and parallel to the launcher track, with recording rates of 7,000 fps and 2,000 fps, respectively.

2.5.2 Data Processing

Strain gage data were processed by first removing any initial offset present in the signal, data were then numerically differentiated to calculate strain rate. Kinematic data from the Vicon system was filtered using a 2nd-order low-pass phaseless butterworth filter with a cutoff frequency of 100 Hz. Vicon marker data on the UAS vehicle was then numerically differentiated for calculation of impact velocity. Kinematic data from the 6 ω and 3 ω arrays on the subject's skull were zeroed and filtered. Linear acceleration and angular velocity channels were filtered using a 2nd order, low-pass, phaseless butterworth filter, with cutoff frequencies of 1650 Hz and 300 Hz, respectively. Finally, cervical and thoracic spine kinematic data from the 3 ω arrays were zeroed and subsequently filtered using the same 2nd order low-pass butterworth filter with a cutoff frequency of 300 Hz.

Vicon marker data was used to calculate displacement and orientation of each test article prior to impact. All Vicon marker data was first transformed from the "Vicon coordinate system" created during camera calibration to the "laboratory coordinate system" created during the pre-test Faro measurement protocol. This transformation ensured that there was only one singular global

coordinate system for both Vicon data and Slicepro kinematic data. Once transformed to the laboratory coordinate system, 3 Vicon markers on each test article were selected to derive global orientation angles of the article during the event. Due to the complex shapes of several test articles, not all Vicon markers were able to be mounted in similar positions, therefore global orientation data was dependent on the placement of the markers. To account for the variation in marker placement, a “corrected coordinate system” was created which adjusted for any error introduced in the initial placement of markers, shown in Figure 12.

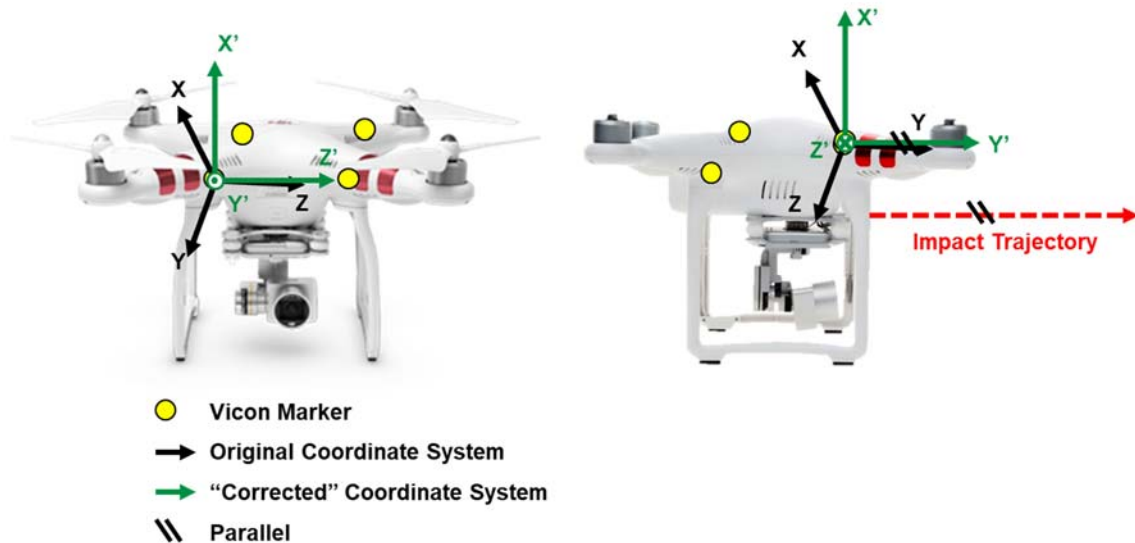


Figure 12 – Original and “corrected” Vicon coordinate system on DJI Phantom 3

Kinematic data from the 3a ω arrays on each subject’s spine were transformed from the sensor location to the superoanterior portion of each vertebral body according to the coordinate system in Figure 13.⁴ From here, local vertebral linear accelerations and angular velocities were output for the C3, C6, T1, and T4 vertebrae of each subject. In addition, local kinematics were transformed to the global coordinate system and numerically integrated to yield both global displacement and orientation angle for each vertebrae.³

⁴ Kang, Y. S., Moorhouse, K., Icke, K., Herriott, R., Bolte, J. H., & John, H. (2014). Head and Cervical Spine Responses of Post Mortem Human Subjects in Moderate Speed Rear Impacts. In *IRCOBI Conference* (Vol. 2014).

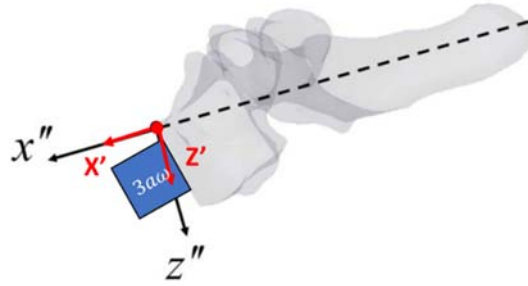


Figure 13 – Vertebral body local coordinate system

Using the $6a\omega$ tetrahedron array, head linear acceleration, angular velocity, and angular acceleration were determined. Angular acceleration channels were not measured directly, but were directly calculated using redundant sensors placed within the $6a\omega$ array.¹ All kinematic data was transformed from the vertex of the tetrahedron to the center of gravity of each subject's head, which was measured directly during autopsy (section 2.5.4). Prior to transforming to the subject's head CG, angular acceleration data was filtered using a 300 Hz low-pass butterworth filter. This technique reduced high-frequency, resonant peaks observed in angular acceleration time histories. These high peaks were an artifact of skull deformation which occurred during severe impacts. A similar technique was used for the redundant $3a\omega$ sensor array on the skull, except that angular acceleration was calculated by numerically differentiating angular velocity data.

Each subject's head kinematic data were normalized to that of a 50th percentile male using a mass-based approach.⁵ However, only the head mass was used to normalize data. A summary of the normalization factors are given in Table 5:

Table 5 – Head kinematic normalization factors

| Normalization Factor | Normalized Data Channel | | | |
|--|--|---|---|---|
| | Time | Linear Acceleration | Angular Velocity | Angular Acceleration |
| $\lambda = \frac{M_{head, 50th}}{M_{head, subject}}$ | $T_{50th} = T_{subject} * \lambda^{1/3}$ | $A_{50th} = A_{subject} * \lambda^{-1/3}$ | $\omega_{50th} = \omega_{subject} * \lambda^{-1/3}$ | $\alpha_{50th} = \alpha_{subject} * \lambda^{-2/3}$ |

2.5.3 Injury Criteria Selection

Normalized head kinematics were further reduced to injury criteria values related to head and brain injury. Many criteria exist to predict the risk of both skull fracture and brain injury. Criteria which have been used to predict skull fracture include the Severity Index (SI)⁶, Head

⁵ Eppinger, R. H., Marcus, J. H., & Morgan, R. M. (1984). *Development of dummy and injury index for NHTSA's thoracic side impact protection research program* (No. 840885). SAE Technical Paper.

⁶ Gadd, C. W. (1966). *Use of a weighted-impulse criterion for estimating injury hazard* (No. 660793). SAE Technical Paper.

Injury Criteria (HIC)⁷, Skull Fracture Correlate (SFC)⁸, Blunt Criterion (BC)⁹ and head peak linear acceleration (PLA)¹⁰, among others. Additional criteria have been developed to predict brain injury risk, including: head resultant angular acceleration (RAA)¹¹, Head Impact Power (HIP)¹², Rotational Injury Criteria (RIC)¹³, Brain Injury Criteria (BrIC)¹⁴, and the Combined Probability of Concussion (VT-CP)¹⁵. This is not an exhaustive list of criteria, but displays the abundance of methods which have been developed to predict head and brain injuries in automotive and sports impact scenarios. For the present work, PLA and HIC were utilized to assess the risk of skull fracture while BrIC and VT-CP were used to investigate brain injury risk. These criteria were selected in concurrence with the ASSURE team as the most robust criteria currently available based on the experimental methods, sample size and data analysis techniques used to derive the criteria. The Head Injury Criteria (HIC) is calculated as follows:

$$\text{HIC}_{15} = \max \left\{ (t_2 - t_1) \left[\frac{\int_{t_1}^{t_2} \bar{a}(t) dt}{(t_2 - t_1)} \right]^{2.5} \right\}$$

Equation 1 – Head Injury Criteria (HIC) Equation

where $\bar{a}(t)$ is the resultant linear acceleration of the head CG and the times t_1 and t_2 are selected to maximize the HIC value such that $t_2 - t_1 < 15$ ms. The Brain Injury Criteria (BrIC) is calculated using the following formulation:

$$\text{BrIC} = \sqrt{\left(\frac{\omega_x}{\omega_{xC}}\right)^2 + \left(\frac{\omega_y}{\omega_{yC}}\right)^2 + \left(\frac{\omega_z}{\omega_{zC}}\right)^2}$$

Equation 2 – Brain Injury Criteria (BrIC) Equation

where, ω_y , ω_x , ω_z are peak values for rotational velocity about each coordinate axis. Peaks are divided by critical values determined from ATD experiments and finite element modelling and are as follows: $\omega_{xC} = 66.25$ rad/s $\omega_{yC} = 56.45$ rad/s $\omega_{zC} = 42.87$ rad/s.⁷ The Virginia Tech Combined Probability of Concussion (VT-CP) is calculated as follows:

⁷ Versace, J. (1971). *A review of the severity index* (No. 710881). SAE Technical Paper.

⁸ Vander Vorst, M., Chan, P., Zhang, J., Yoganandan, N., & Pintar, F. (2004). A new biomechanically-based criterion for lateral skull fracture. In *Annual Proceedings/Association for the Advancement of Automotive Medicine* (Vol. 48, p. 181). Association for the Advancement of Automotive Medicine.

⁹ Raymond, D., Van Ee, C., Crawford, G., & Bir, C. (2009). Tolerance of the skull to blunt ballistic temporo-parietal impact. *Journal of biomechanics*, 42(15), 2479-2485.

¹⁰ Mertz, H. J., Irwin, A. L., & Prasad, P. (2016). *Biomechanical and scaling basis for frontal and side impact injury assessment reference values* (No. 2016-22-0018). SAE Technical Paper.

¹¹ Rowson, S., Duma, S. M., Beckwith, J. G., Chu, J. J., Greenwald, R. M., Crisco, J. J., ... & Maerlender, A. C. (2012). Rotational head kinematics in football impacts: an injury risk function for concussion. *Annals of biomedical engineering*, 40(1), 1-13.

¹² Newman, J. A., & Shewchenko, N. (2000). *A proposed new biomechanical head injury assessment function-the maximum power index* (No. 2000-01-SC16). SAE Technical Paper.

¹³ Kimpara, H., & Iwamoto, M. (2012). Mild traumatic brain injury predictors based on angular accelerations during impacts. *Annals of biomedical engineering*, 40(1), 114-126.

¹⁴ Takhounts, E. G., Craig, M. J., Moorhouse, K., McFadden, J., & Hasija, V. (2013). *Development of brain injury criteria (BrIC)*(No. 2013-22-0010). SAE Technical Paper.

¹⁵ Rowson, S., & Duma, S. M. (2013). Brain injury prediction: assessing the combined probability of concussion using linear and rotational head acceleration. *Annals of biomedical engineering*, 41(5), 873-882.

$$VT-CP = \left(1 + e^{-(-10.2 + .0433 \cdot a + .000873 \cdot \alpha - 9.2 \times 10^{-7} \cdot a \cdot \alpha)}\right)^{-1}$$

Equation 3 – Virginia Tech Combined Probability of Concussion Equation

Where a and α are the resultant linear acceleration and angular acceleration of the head CG, respectively. Injury criteria values for each impact were subsequently compared to their respective injury risk curves to investigate the risk of: AIS2+ level skull fracture^{16,17}, AIS3+ level head injury¹⁸, AIS level 1,2 and 3 brain injury¹⁴, and minor concussion¹⁵.

2.5.4 Autopsy

Following all planned tests, a detailed autopsy was performed on each subject's head and cervical spine. During autopsy, subjects' heads were removed at the occipital condyle by first dissecting through the posterior neck musculature to the inferior nuchal line. From the inferior nuchal line, dissection proceeded to both left and right mastoid processes. Once reached, the atlanto-occipital joint capsule was dissected and wedged open. Once disarticulated at the atlanto-occipital joint, dissection continued anteriorly along the inferior portion of the mandible. After completely disarticulation, the head center of gravity was determined using the following technique^{19,20}:

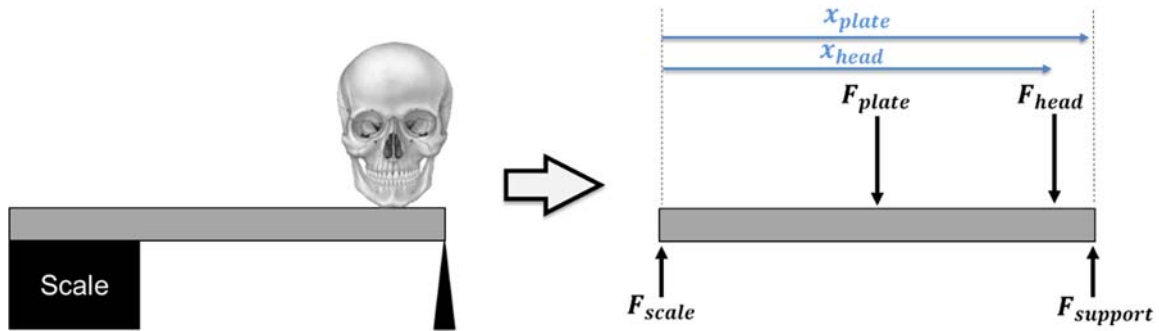


Figure 14 – Head CG measurement schematic

$$\sum M_{support} = 0 = F_{plate} * \frac{x_{plate}}{2} + F_{head} * (x_{plate} - x_{head}) - F_{scale} * x_{plate} \rightarrow$$

¹⁶ Eppinger, R., Sun, E., Bandak, F., Haffner, M., Khaewpong, N., Maltese, M., ... & Zhang, A. (1999). Development of improved injury criteria for the assessment of advanced automotive restraint systems–II. *National Highway Traffic Safety Administration*, 1-70.
¹⁷ Mertz, H. J., Irwin, A. L., & Prasad, P. (2016). *Biomechanical and scaling basis for frontal and side impact injury assessment reference values* (No. 2016-22-0018). SAE Technical Paper.
¹⁸ National Highway Traffic Safety Administration, 2008. Consumer Information; New Car Assessment Program; Final Decision Notice. 73 Federal Register 134, pp 40016-40050
¹⁹ Self, B. P., Spittle, E. K., Kaleps, L. and Alberty, C. B. (1992) Accuracy and repeatability of the standard automated mass properties measurement system. AL-TR-1992-0137, Armstrong Laboratory. Wright-Patterson AFB, Ohio.
²⁰ Kang, Y. S., Stammen, J., Moorhouse, K., Herriott, R., & Bolte IV, J. H. (2016). PMHS Lower Neck Load Calculation using Inverse Dynamics with Cervical Spine Kinematics and Neck Mass Properties. *International Research Council on Biomechanics of Injury*.

$$X_{CG} = (x_{plate} - x_{head}) = \left(\frac{x_{plate} \left(F_{scale} - \frac{F_{plate}}{2} \right)}{F_{head}} \right)$$

Equation 4 – Head center of gravity equation

After measuring the head center of gravity, subjects’ calvariums were dissected to look for skull fractures. Once dissected, subjects’ skull caps were removed, and physical measurements of skull thickness were taken. Any abnormalities along the inner table of subjects’ calvariums were noted. Subjects’ cervical spines were also dissected and analyzed for injury. Dissection made use of the pre-existing incisions in to the retropharyngeal space to clear all anterior muscles. Once cleared, bony fractures, as well as tears or laxity of the anterior longitudinal ligament were noted. All injuries were coded according to the AIS 2015 severity scale.²¹

2.5.4.1 Abbreviated Injury Scale (AIS) Background

The abbreviated injury scale was first introduced in 1971 as a “anatomically-based, consensus-driven, global severity scoring system that classifies injury. It describes injury in terms of anatomic location, specific lesion and relative severity on a 6-point ordinal scale.”²¹ A description of the AIS severity scale is given in Table 6.

Table 6 – AIS Severity Scale

| AIS Code | Description |
|----------|-------------|
| 1 | Minor |
| 2 | Moderate |
| 3 | Serious |
| 4 | Severe |
| 5 | Critical |
| 6 | Maximal |
| 9 | Unknown |

Multiple factors are used to determine the severity of an injury, these include: threat to life, disability (permanent or temporary), tissue damage, treatment complexity, length of recovery, quality of life and cost. Apart from the severity scale, injuries are categorized by body region, anatomic structure and injury level. AIS severity scores are not equivalent across body regions. For example, an AIS level 3 head injury is not comparable to an AIS 3 level injury in the lower extremity. Furthermore, the AIS severity scale is not intended to predict mortality; an AIS severity score of 6 does not necessarily coincide with a fatality.

²¹ The Abbreviated Injury Scale – 2015 Revision. AAM, Des Plaines IL, 2015.

When assessing subjects with multiple injuries there are two methods which are most widely used: The Maximum AIS (MAIS) and the Injury Severity Score (ISS). The MAIS is the highest AIS severity code in a subject with multiple injuries. The ISS is more frequently used in the clinical setting and is calculated as the sum of squares of the highest AIS scores in three different body regions. The body regions used for ISS calculation include: Head/neck, face, chest, abdomen/pelvis, extremities/pelvic girdle, external.

In the automotive safety field, AIS severity levels recorded during impact tests are often related to kinematic or kinetic variables to develop probabilistic models of injury risk.²² These probabilistic models, or injury risk curves, define the probability of sustaining an AIS 1, AIS 2, AIS 3, etc. severity injury based on a predictor variable measured during impact testing (acceleration, force, strain, etc.). Due to limitations in sample size, risk curves are often generated by grouping higher and lower severity levels together. For example, Figure 15 below displays an example AIS 3+ injury risk curve. This risk curve would group any AIS 0,1, or 2 severities as “non-injury” points, or “0” points if using logistic regression. Likewise, any injuries that are AIS 3, 4, 5, or 6 would be grouped as “injury” points. The resulting injury risk curve predicts the probability of sustaining an AIS 3 or greater injury. Similarly, by grouping AIS codes at other severity levels, separate risk curves could be generated for predicting AIS 2+, AIS 4+, or AIS 5+ injuries.

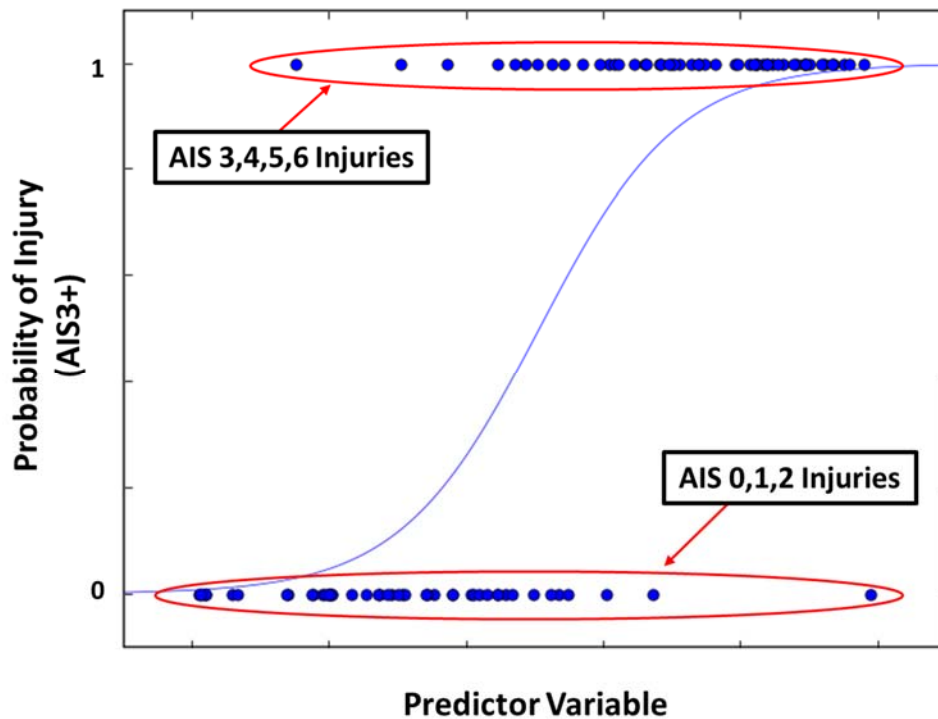


Figure 15 – Example AIS 3+ injury risk curve

²² Petitjean, A., Trosseille, X., Yoganandan, N., & Pintar, F. A. (2015). Normalization and scaling for human response corridors and development of injury risk curves. In *Accidental Injury* (pp. 769-792). Springer, New York, NY.

3. RESULTS

3.1 Injuries

Two of five subjects sustained identifiable injuries as a result of testing. In PMHS03, An AIS 2 level skull fracture (AIS Code: 150402.2 10AA) was observed. The fracture was 5.1 inch linear fracture, extending from the right orbit to the coronal suture, shown in Figure 16.

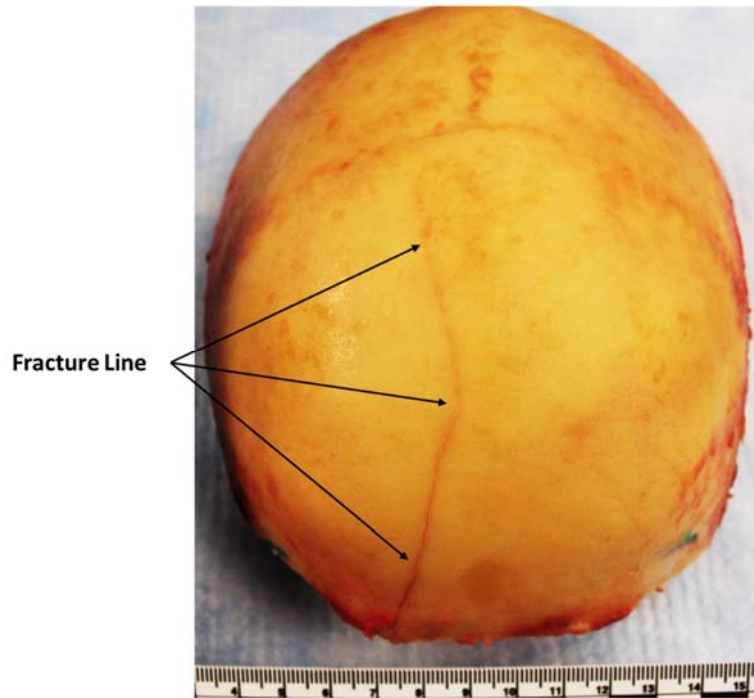


Figure 16 – PMHS03, 5.1 inch linear skull fracture

The injury occurred as a result of a 58-degree, frontal, Phantom 3 impact at 71 ft/s (OSU #19). The injury was confirmed by investigation of strain rate data shown in Figure 17. The large spike in strain rate data for OSU #19 indicates a sudden release of tension, coincident with a drop in strain, thus indicating that the skull fracture occurred during that test.

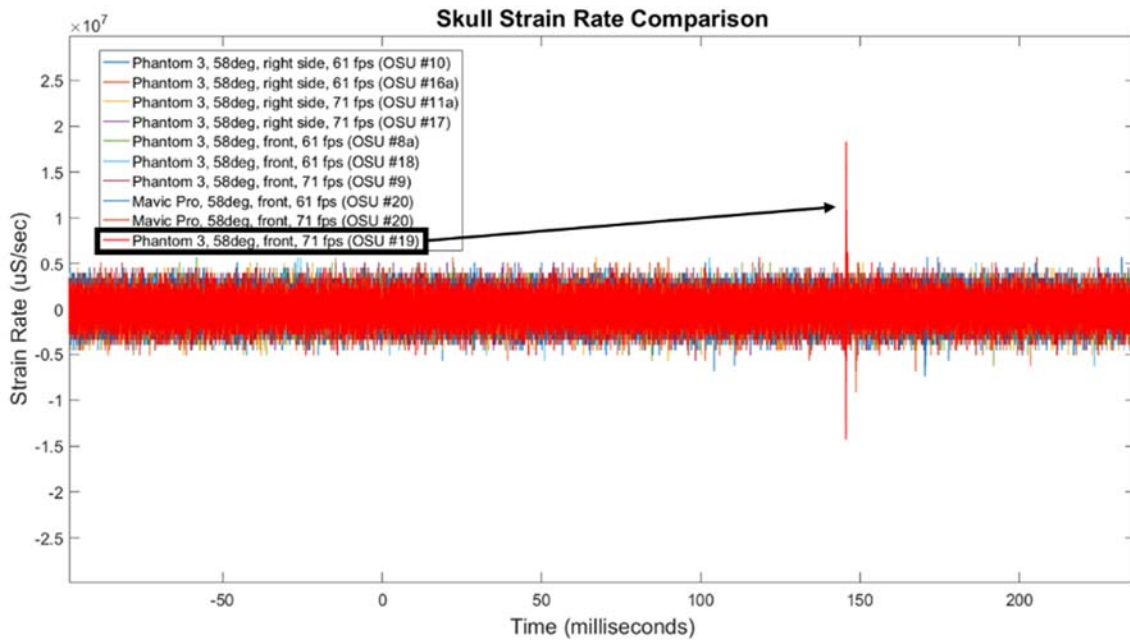


Figure 17 – Strain rate time histories for all tests conducted on PMHS02, and PMHS03

In addition, PMHS05 also sustained multiple injuries as a result of wood block impacts, as displayed in Figure 18.

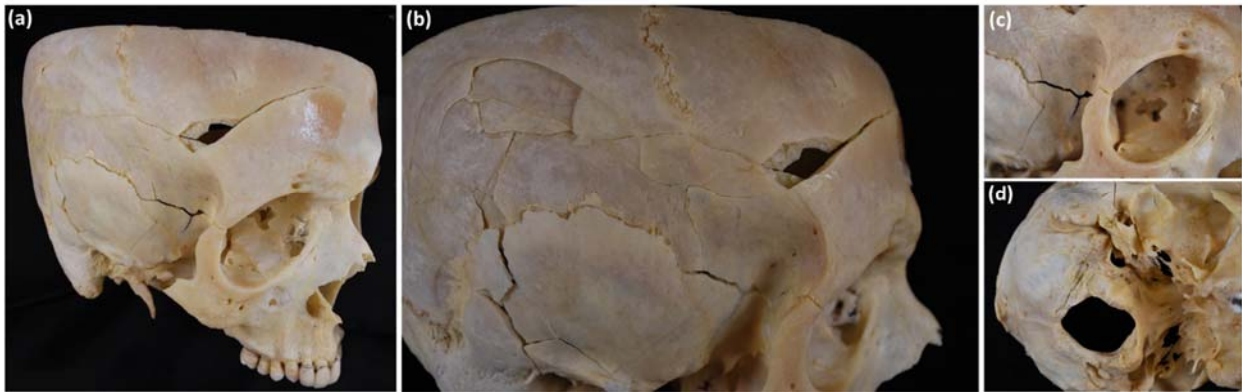


Figure 18 – Skeletal injuries sustained by PMHS05, (a) comminuted fracture of frontal bone, (b) comminuted fractures of the temporal and parietal bones, (c) lateral wall fracture of right orbit, (d) basilar skull fracture, viewed from inferior to superior

Using strain rate analysis in addition to autopsy results, it was determined that injuries occurred on both 30 ft/s and 40 ft/s impacts. Due to the unknown extent of injuries as a result of the 30 ft/s impact, an AIS level of 2 was assigned. Therefore, the injuries resulting from the 40 ft/s impact were assigned an AIS severity level of 4. The specific test in which each injury occurred is unknown; therefore, it is possible that an AIS 3+ injury occurred on the 30 ft/s impact; however, to remain conservative, the lowest observed AIS severity (AIS 2) was

assigned. Table 7 contains a summary of injuries and AIS severities for both PMHS03 and PMHS05.

Table 7 – Summary of PMHS injuries

| Subject # | Region | Structure | Description | Code | AIS Level | MAIS |
|-----------|--------|--|---|---------------|-----------|------|
| PMHS03 | Head | Skeletal | Vault fracture (frontal bone), linear | 150402.2 11AA | 2 | 2 |
| | | | Vault fracture (frontal bone), comminuted with dura intact | 150404.3 11AA | 3 | |
| PMHS05 | Head | Skeletal | Vault fracture (temporal bone), comminuted with dura intact | 150404.3 10AC | 3 | |
| | | | Vault fracture (parietal), comminuted with dura intact | 150404.3 10AB | 3 | |
| | | | Basilar fracture, multiple linear fractures, dura intact | 150200.3 | 3 | 4 |
| | | | Small epidural hematoma | 140632.4 1000 | 4 | |
| | Face | Skeletal | Nose fracture | 251000.1 10AG | 1 | |
| | | | Orbit fracture, multiple fractures of the same orbit | 251205.2 10AL | 2 | |
| | | | Orbit fracture, lateral wall | 251235.2 10AK | 2 | |
| | | Zygoma fracture, displaced arch fracture | 251806.1 10AK | 1 | | |

3.2 Head Kinematics

An example impact response of PMHS and test article, taken from high speed video footage is shown in Figure 19. Additional examples are available in 6. APPENDIX A—. Subject resultant head kinematic time histories are given for several 0-degree side impact scenarios in Figure 20 - Figure 22. Plots displaying other impact directions are available in APPENDIX B—.

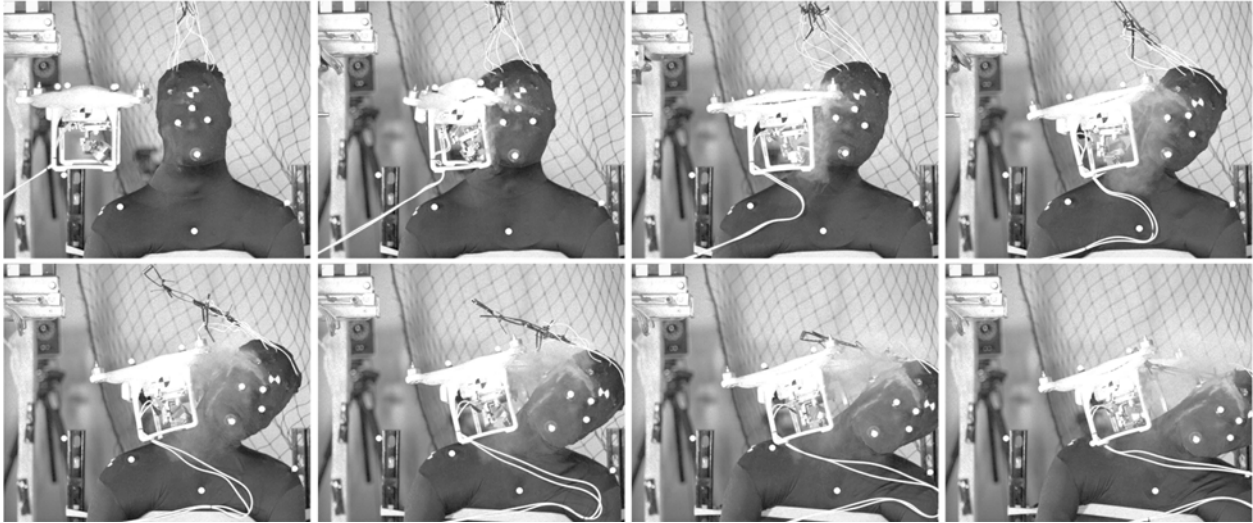


Figure 19 – Impact response of PMHS and Phantom 3 during a 71 ft/s, 0-degree, right side impact, [10 millisecond time steps] (Test: OSU #4)

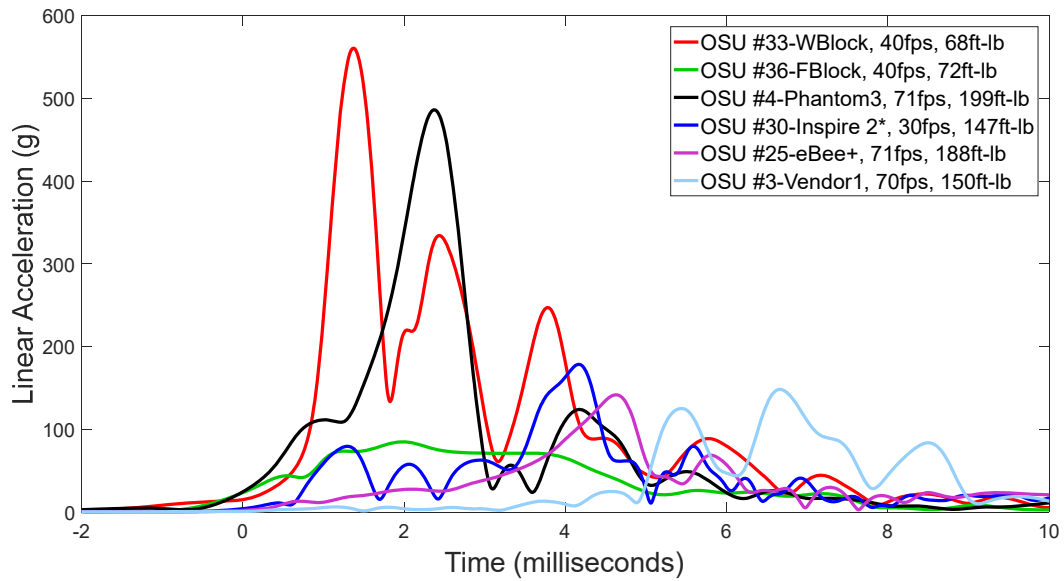


Figure 20 – Resultant CG head linear acceleration time histories in 0-degree, side impact scenarios

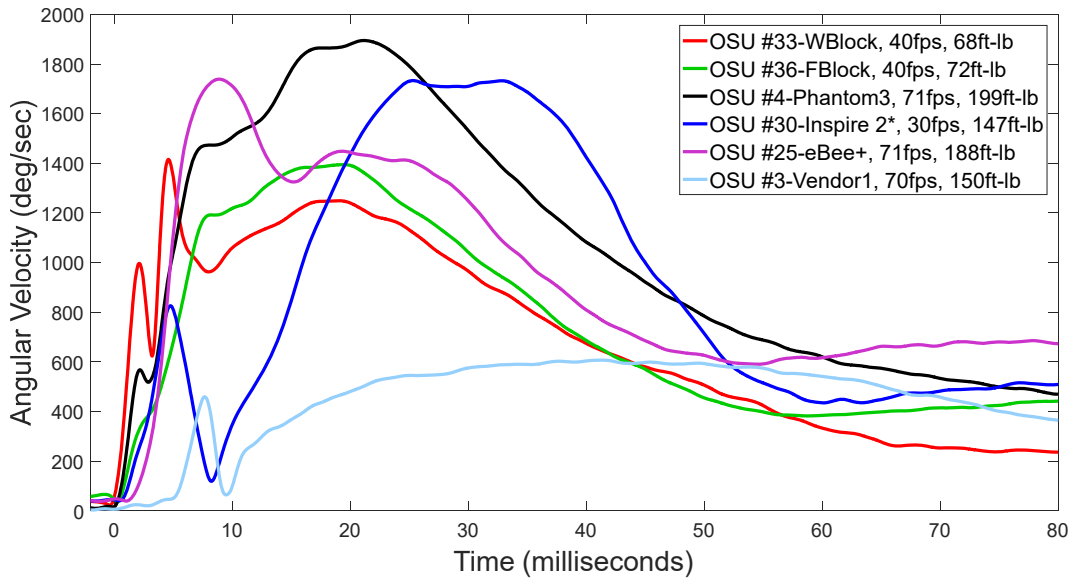


Figure 21 – Resultant head angular velocity time histories in 0-degree, side impact scenarios

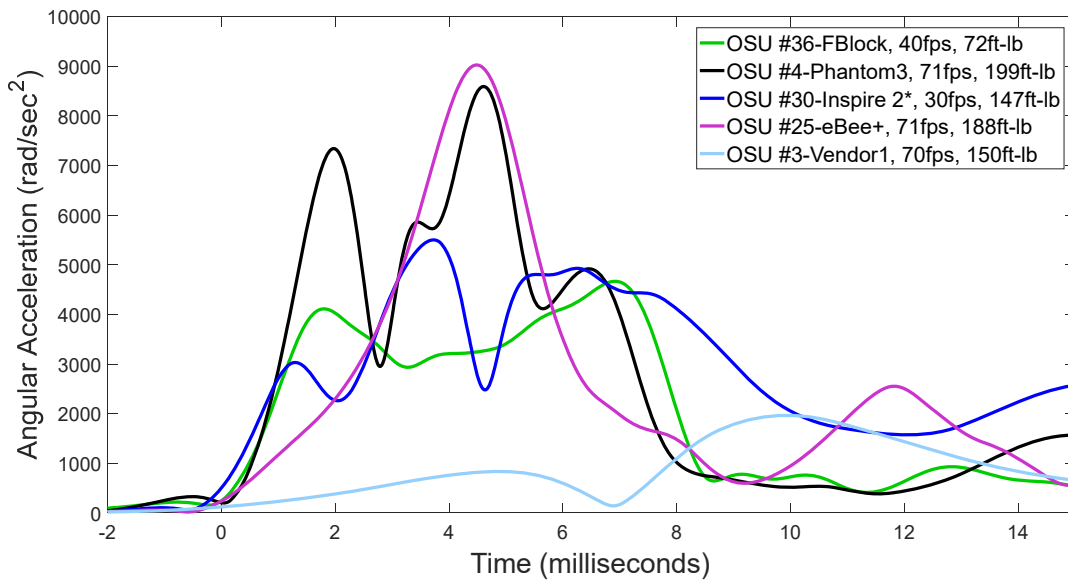


Figure 22 – Resultant head angular acceleration time histories in 0-degree, side impact scenarios
 Note: Wood Block time history not included due to its high angular acceleration magnitude

Peak head kinematics for all tests are available in Table 8. For 0-degree, side impacts due to UAS vehicles, average response kinematics were $234 \pm 141g$ for head linear acceleration, 1541 ± 432 deg/sec for angular velocity and 5995 ± 2571.8 rad/sec² for angular acceleration. For this impact scenario the Phantom 3 obtained the highest linear acceleration (486g) and angular velocity (1895 deg/sec) peak values; whereas, the eBee+ obtained the highest peak for angular acceleration (9025 rad/sec²).

In 58-degree, frontal impact scenarios, PMHS peak head kinematics averaged $410 \pm 203g$ for linear acceleration, 1181 ± 388 deg/sec for angular velocity and 8066 ± 2847 rad/sec² for angular acceleration. In this impact condition, the Mavic Pro obtained the largest peak linear acceleration (711g), while the Phantom 3 obtained the largest peak kinematics for angular velocity (1603 deg/sec) and angular acceleration (11,245 rad/sec²).

In 58-degree, right/left side impact scenarios, PMHS peak head kinematics averaged $202 \pm 115g$ for linear acceleration, 1142 ± 220 deg/sec for angular velocity and 6169 ± 2407 rad/sec² for angular acceleration. The Phantom 3 obtained the largest peak kinematics for all measures in this scenario (378 g, 1379 deg/sec, 10,410 rad/sec²).

Finally, in 90-degree, top impact scenarios, peak head kinematics averaged $370 \pm 110g$, 876 ± 282 deg/sec and 6186 ± 1276 rad/sec² for linear acceleration, angular velocity and angular acceleration measures, respectively. Additionally, the Phantom 3 obtained the largest peak kinematics for all measures in this scenario (551g, 1115 deg/sec, 7886 rad/sec²).

Table 8 – Peak head kinematics for all tests articles, categorized by impact direction

| Impact Angle | Impact Location | Vehicle | PMHS # | Impact Speed (ft/s) | Impact KE (ft-lbs) | Linear Acceleration (g) | Angular Velocity (deg/sec) | Angular Acceleration (rad/sec ²) | | |
|--------------|-----------------|-------------|-----------------|---------------------|--------------------|-------------------------|----------------------------|--|------|------|
| 0° | Left/Right Side | Block, Foam | 05 | 20 | 18 | 52 | 660 | 2659 | | |
| | | Block, Foam | 05 | 30 | 37 | 68 | 1084 | 3733 | | |
| | | Block, Foam | 05 | 40 | 72 | 85 | 1395 | 4667 | | |
| | | Block, Wood | 05 | 20 | 15 | 229 | 760 | 6875 | | |
| | | Block, Wood | 05 | 30 | 40 | 358 | 1127 | 18479 | | |
| | | Block, Wood | 05 | 40 | 68 | 561 | 1416 | 26070 | | |
| | | Inspire 2* | 04 | 30 | 147 | 178 | 1733 | 5502 | | |
| | | Phantom 3 | 01 | 56 | 126 | 284 | 1458 | 3522 | | |
| | | Phantom 3 | 01 | 61 | 150 | 328 | 1717 | 6337 | | |
| | | Phantom 3 | 01 | 71 | 199 | 486 | 1895 | 8592 | | |
| | | eBee+ | 04 | 64 | 141 | 73 | 1638 | 7020 | | |
| | | eBee+ | 04 | 71 | 188 | 142 | 1739 | 9025 | | |
| | | Vendor 1 | 01 | 70 | 57 | 148 | 607 | 1966 | | |
| 58° | Front | Mavic Pro | 04 | 61 | 85 | 502 | 627 | 7429 | | |
| | | Mavic Pro | 03 | 61 | 88 | 655 | 1113 | 9026 | | |
| | | Mavic Pro | 04 | 71 | 120 | 490 | 689 | 7562 | | |
| | | Mavic Pro | 03 | 71 | 122 | 711 | 1344 | 10682 | | |
| | | Phantom 3 | 01 | 56 | 136 | 219 | 1351 | 8035 | | |
| | | Phantom 3 | 02 | 61 | 148 | 160 | 1288 | 7291 | | |
| | | Phantom 3 | 03 | 61 | 151 | 385 | 1445 | 5196 | | |
| | | Phantom 3 | 01 | 61 | 156 | 241 | 1603 | 11230 | | |
| | | Phantom 3 | 03 | 71 | 198 | 644 | 1558 | 11245 | | |
| | | Phantom 3 | 02 | 71 | 205 | 175 | 1444 | 9433 | | |
| | | Vendor 1 | 01 | 70 | 63 | 325 | 528 | 1601 | | |
| | | 58° | Left/Right Side | eBee+ | 04 | 64 | 146 | 91 | 1331 | 4938 |
| | | | | eBee+ | 04 | 71 | 186 | 117 | 1127 | 3561 |
| eBee+ | 04 | | | 71 | 188 | 72 | 788 | 3757 | | |
| Phantom 3 | 03 | | | 61 | 142 | 216 | 1037 | 6406 | | |
| Phantom 3 | 02 | | | 61 | 152 | 239 | 991 | 6343 | | |
| Phantom 3 | 02 | | | 71 | 205 | 303 | 1340 | 7764 | | |
| Phantom 3 | 03 | | | 71 | 209 | 378 | 1379 | 10410 | | |
| 90° | Top | | | Phantom 3 | 02 | 56 | 117 | 393 | 1115 | 4911 |
| | | | | Phantom 3 | 02 | 65 | 161 | 468 | 1091 | 5433 |
| | | | | Phantom 3 | 03 | 65 | 168 | 356 | 1072 | 6635 |
| | | Phantom 3 | 02 | 71 | 196 | 551 | 693 | 7874 | | |
| | | Phantom 3 | 03 | 71 | 199 | 307 | 1108 | 7887 | | |
| | | Vendor 1 | 03 | 70 | 57 | 249 | 482 | 5345 | | |
| | | Vendor 1 | 03 | 70 | 57 | 265 | 573 | 5220 | | |

3.3 Head & Brain Injury Risk

Injury criteria values were calculated using normalized head kinematics from each subject. HIC, BrIC and VT-CP values for each test are displayed in Figure 23 - Figure 25.

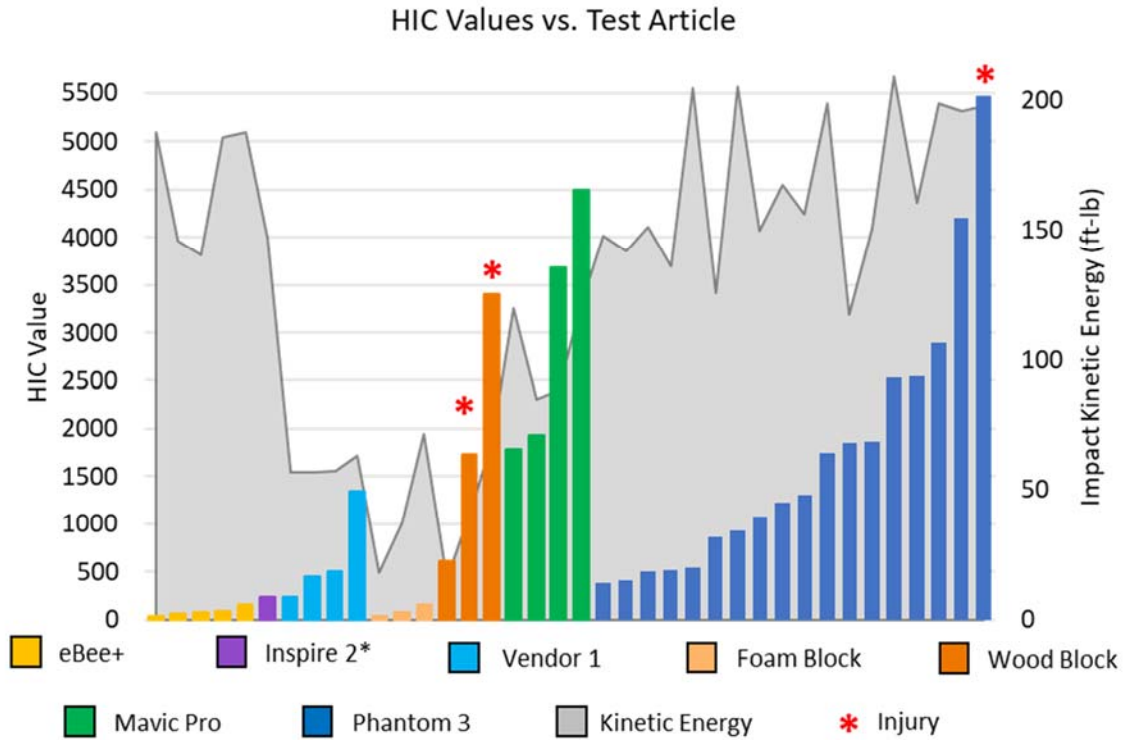


Figure 23 – HIC values for all impacts. Note: Injurious HIC values are tests in which impacts resulted in an AIS2+ skull fracture

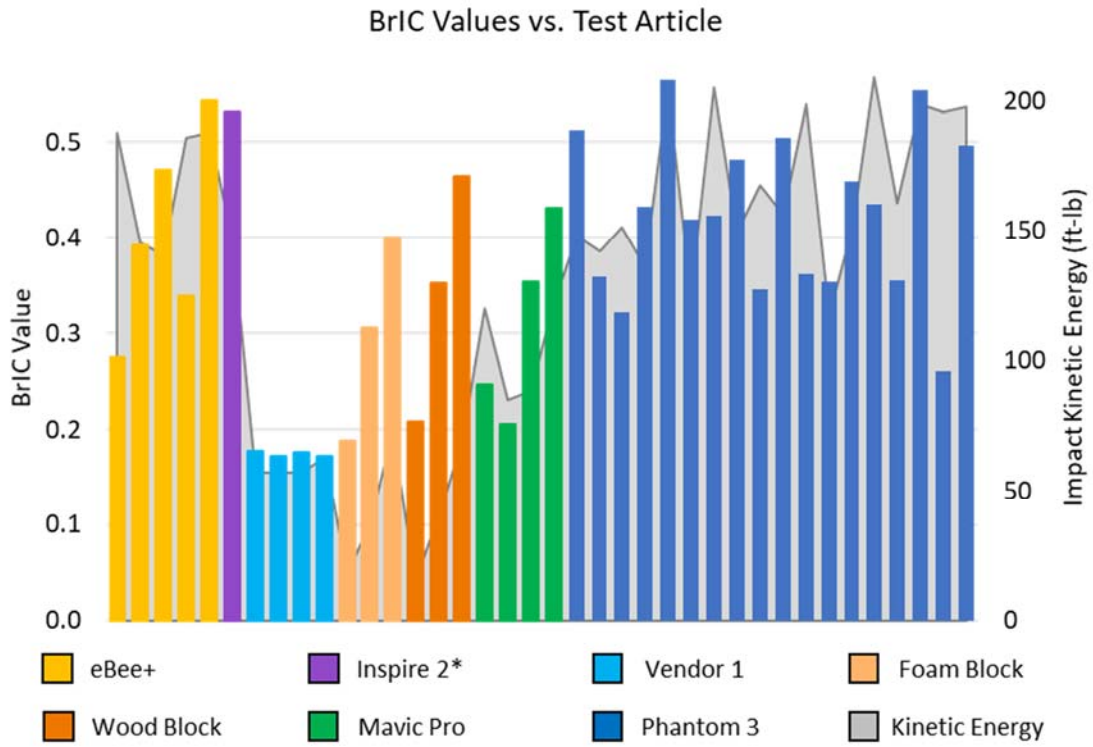


Figure 24 – BrIC values for all impacts

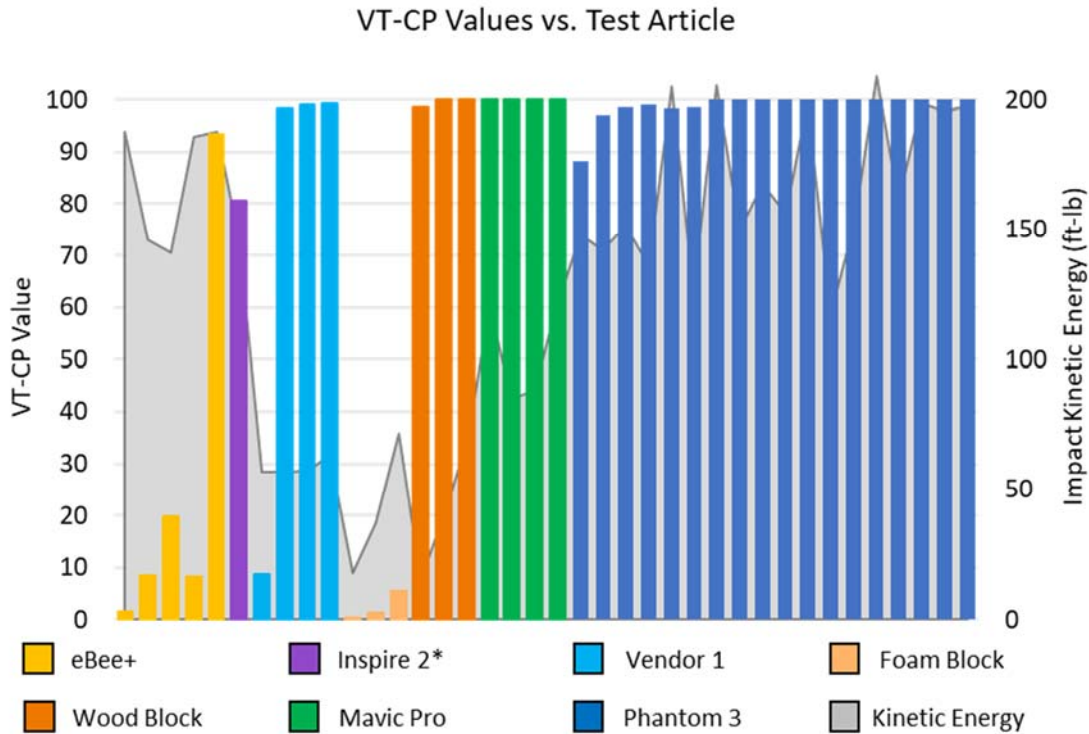


Figure 25 – VT-CP values for all impacts

When looking at UAS vehicles only, the Mavic Pro averaged the highest HIC values (2972 ± 1330), followed by the Phantom 3 (1713 ± 1393), Vendor 1 (634 ± 483), Inspire 2* (237), and eBee+ (84 ± 42). The largest BrIC value was measured for the Inspire 2* (0.53). Following the Inspire 2*, the Phantom 3 averaged 0.42 ± 0.08 , eBee+ averaged 0.40 ± 0.11 , Mavic Pro averaged 0.31 ± 0.1 , and Vendor 1 averaged 0.17 ± 0.003 . Finally, both the Phantom 3 and Mavic Pro averaged a 1.0 VT-CP value, while the eBee+ averaged 0.83 ± 0.38 . The Vendor 1 and Inspire 2* averaged 0.8 ± 0.45 and 0.81 , respectively.

Injury criteria values for the Phantom 3, categorized by impact direction are given in Table 9. The highest HIC values came as a result of a 58-degree frontal impact (HIC:5473) and a 90-degree top impact (HIC 4197). The largest BrIC values came from a 58-degree frontal impact (BrIC: 0.56) and a 0-degree right side impact (BrIC:0.55). Finally, the largest VT-CP values came from a 58-degree frontal impact (VT-CP:1.000) and a 90-degree top impact (VT-CP:0.99999).

Table 9 – Injury criteria values for Phantom 3 impacts

| Impact Angle | Impact Location | PMHS # | Impact Speed (ft/s) | Impact KE (ft-lbs) | HIC ₁₅ | BrIC | VT-CP | |
|--------------|-----------------|--------|---------------------|--------------------|-------------------|------|-------|------|
| 0 | Right Side | 01 | 56 | 126 | 866 | 0.42 | 0.99 | |
| | | 01 | 61 | 150 | 1076 | 0.48 | 1.00 | |
| | | 01 | 71 | 199 | 2892 | 0.55 | 1.00 | |
| 58 | Front | 01 | 56 | 136 | 522 | 0.43 | 0.99 | |
| | | 01 | 61 | 156 | 1304 | 0.50 | 1.00 | |
| | | 02 | 61 | 148 | 380 | 0.51 | 0.88 | |
| | | | 02 | 71 | 205 | 539 | 0.56 | 0.98 |
| | | | 03 | 61 | 151 | 1861 | 0.46 | 1.00 |
| | | | 03 | 71 | 198 | 5473 | 0.50 | 1.00 |
| | Right Side | | 02 | 61 | 152 | 500 | 0.32 | 0.99 |
| | | | 02 | 71 | 205 | 929 | 0.42 | 1.00 |
| | | | 03 | 61 | 142 | 412 | 0.36 | 0.97 |
| 90 | Top | 03 | 71 | 209 | 2527 | 0.43 | 1.00 | |
| | | 02 | 56 | 117 | 1848 | 0.35 | 1.00 | |
| | | 02 | 65 | 161 | 2550 | 0.35 | 1.00 | |
| | | 02 | 71 | 196 | 4197 | 0.26 | 1.00 | |
| | | 03 | 65 | 168 | 1219 | 0.35 | 1.00 | |
| | | 03 | 71 | 199 | 1748 | 0.36 | 1.00 | |

Values in red represent greater than a 30% risk of AIS 3 head and brain injury for HIC and BrIC values, respectively; or, greater than a 95% risk of concussion injury

Injury criteria values were related to their respective injury risk functions to assess their efficacy in predicting injuries in UAS impact scenarios. Risk curves for peak linear acceleration, HIC, BrIC and VT-CP are given in Figure 26 - Figure 29. Note that several tests have been removed from this analysis (OSU #20-23) because injury occurred prior their completion; thus, they cannot be used in the prediction of injury risk.

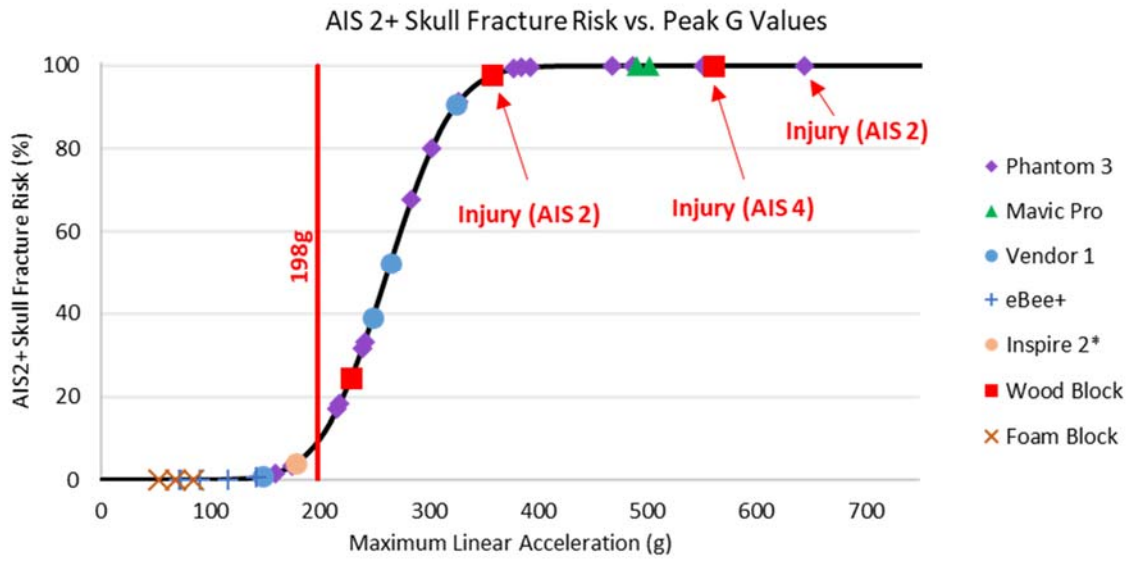


Figure 26 – Comparison of AIS 2+ level skull fracture risk¹⁷ and PMHS test data

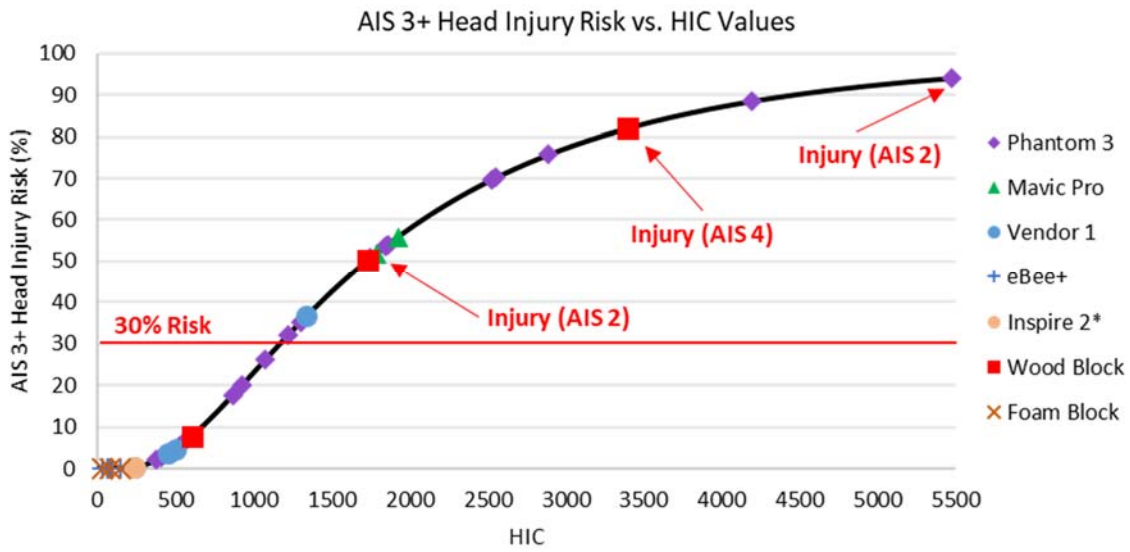


Figure 27 – Comparison of AIS 3+ level head injury risk¹⁸ and PMHS test data

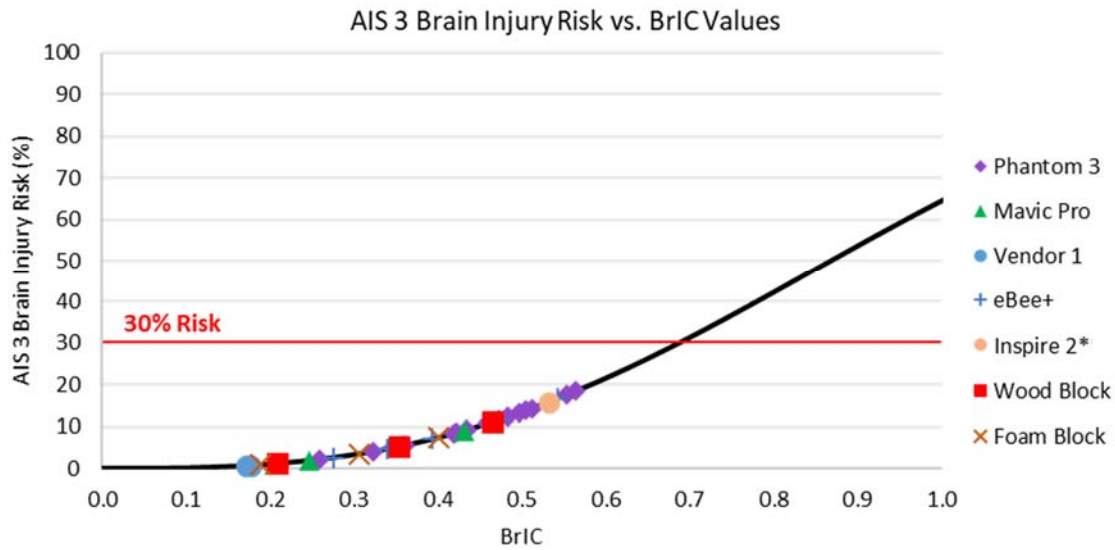


Figure 28 – Comparison of AIS 3 level brain injury risk⁷ and PMHS test data

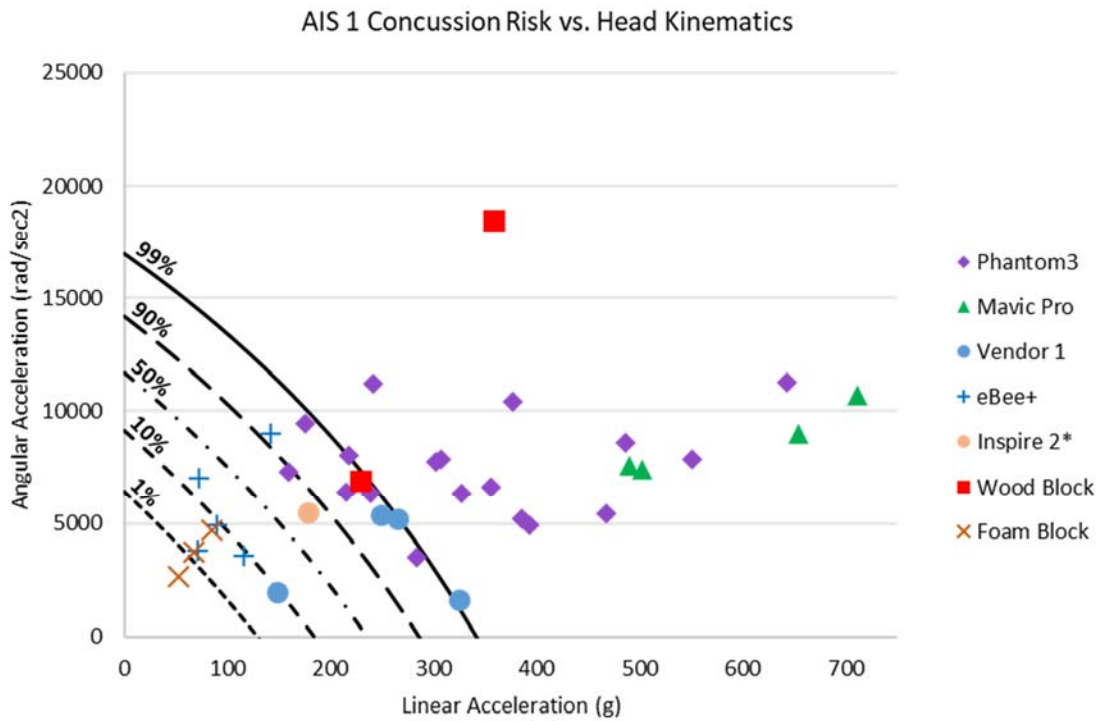


Figure 29 – Comparison of concussion risk gradients⁸ and PMHS test data

Focusing on the risk of skull fracture, the test with both the highest linear acceleration peak as well as the highest HIC value was the Phantom 3, 58-degree, 71ft/s, frontal impact case (OSU #19). Additionally, this was the test in which an AIS 2 level skull fracture occurred. There was a 100% and 94% risk of skull fracture for this test according to the PeakG and HIC risk

curves, respectively. Additionally, 28 test points had concussion risk values above 90%, while zero test points had greater than a 30% chance of causing an AIS3 brain injury.

4. DISCUSSION

4.1 PMHS Injuries

As a result of 35 individual UAS impacts, only one AIS 2+ skeletal injury was observed: a 5.1 inch linear skull fracture of the frontal bone. The injury occurred during a 58-degree, 71 ft/s, frontal impact with the Phantom 3, and was coded at a “moderate” AIS 2 severity level. The HIC value for this test was 5473, which corresponded to a 97.4% risk of an AIS 2 level skull fracture according to an automotive-based injury risk curve.⁵ Several other high-risk HIC values were measured in UAS impacts without injury occurring. For example, two Mavic Pro impacts (OSU #20, #21) exceeded greater than a 90% risk of causing an AIS 2 skull fracture, and greater than 80% risk of causing an AIS 3 head injury. However, these impacts were conducted subsequent to the injurious Phantom 3 test (OSU #19); therefore, the injury potential of these impacts could not be assessed. Additionally, both 0-degree side impacts (OSU #4) and 90-degree top impacts (OSU #15) incurred AIS 3 head injury risk probabilities of 75% and 88%, respectively, yet these tests did not result in injury. The lack of injury in these cases could be due to differences in fracture limits for different locations throughout the skull. Previous studies have noted a higher fracture tolerance in different regions of the skull, with the temporo-parietal region having nearly 1.6× the tolerance of the frontal region.²³ Additionally, differences in fracture tolerance could be due to test article stiffness properties, PMHS skull variation, or a combination of both. When comparing 0-degree side impacts, PMHS01 was impacted with a Phantom 3 and sustained a HIC severity of 2893 without injury, while PMHS05 was impacted with a wood block and sustained a HIC severity of 1729, which resulted in an AIS 2 skull fracture. Previous studies have also noted this variation in fracture tolerance between different PMHS subjects as well as with different impacting surfaces.²⁴ Therefore, while the occurrence of a skull fracture indicates that UAS impacts may pose a threat to public safety, more testing is needed to determine the specific prevalence and probability associated with UAS-induced skull fracture injuries.

4.2 Head Injury Risk Thresholds & Limits

When comparing to a 30% risk of an AIS 3 level head injury, 15 of the 35 PMHS-UAS impacts exceeded the threshold. Of the 15 tests that exceeded the 30% risk limit, 10 involved the Phantom 3, 4 involved the Mavic Pro, 1 involved the Vendor 1, and none were recorded with the eBee+. When normalizing for the number of tests conducted with each UAS, 56% of Phantom 3 tests exceeded the 30% limit, while 100% of Mavic Pro tests and 25% of Vendor 1 tests also exceeded the limit. Yet, of these 15 total exceedances, zero AIS level 3 head injuries were observed. Similarly, 18 of 35 UAS impacts exceeded the AIS 2 injury HIC limit of 700, while only one AIS 2 skull fracture was observed. Four tests predicted greater than an 85% risk of skull

²³ Zhang, J., Yoganandan, N., & Pintar, F. A. (2009, October). Dynamic biomechanics of the human head in lateral impacts. In *Annals of Advances in Automotive Medicine/Annual Scientific Conference* (Vol. 53, p. 249). Association for the Advancement of Automotive Medicine.

²⁴ Yoganandan, N., & Pintar, F. A. (2004). Biomechanics of temporo-parietal skull fracture. *Clinical Biomechanics*, 19(3), 225-239.

fracture, with none being observed in autopsy. Based on the tests ran and injuries observed in this study, a HIC value of 700 coincides with a 5% probability of an AIS 2 level skull fracture. This disagrees with the current automotive standard which assigns a 30% risk with a HIC value of 700.¹⁶ This indicates that HIC limits for UAS impacts appear to be conservative when using automotive-based injury risk functions. However, the test in which injury occurred was also the test with the highest recorded HIC value, indicating that HIC may be a viable predictor for injury in UAS impact scenarios. These data reveal that additional investigation is needed to determine the efficacy of HIC as a predictor for the severity of head injuries in UAS impacts.

Similar to HIC limits, the proposed peak head acceleration limit of 198g is conservative according to PMHS test data. Of the 35 UAS tests conducted, 17 tests recorded linear accelerations above 198g. Of these 17 tests, one AIS 2 level skull fracture was observed. This ratio corresponds to an injury risk probability of 6%. According to an automotive-based risk curve which uses linear acceleration to predict AIS 2 skull fracture, a peak linear acceleration of 198g corresponds to a 10% risk of injury.¹⁷ In terms of peak linear acceleration data, impact data from the current study aligns well with the automotive-based risk curves. However, because only one UAS-related injury was observed in this study, more data is needed to determine if peak linear acceleration is an appropriate criterion for predicting injury in this scenario.

4.3 Concussion Risk Assessment

Based on BrIC and VT-CP values, UAS impacts averaged a 99% and 84% risk of causing an AIS 1 level concussion, respectively. However, concussion diagnosis is not possible in PMHS testing because it is currently reliant upon verbal and motor skills tests.²⁵ Additionally, there is disagreement within the research community pertaining to the efficacy of both models.^{7,8,26,27} Furthermore, inconsistency between the two metrics was evident in UAS impact cases. According to BrIC, eBee+ vehicles averaged a 99% risk of causing a concussion; whereas, according to the VT-CP metric, eBee+ averaged only a 26% risk of concussion. Thus, due to inconsistency between concussion metrics measured during PMHS testing, as well as disagreement within the scientific community concerning which metric is more accurate, a concussion criteria or threshold cannot be put forth at this time.

4.4 UAS Vehicle Risk Comparison

When looking at skull fracture risk, heavier and stiffer vehicles such as the Phantom 3 and Mavic Pro produced higher HIC and peak linear acceleration values as illustrated in Table 10. Phantom 3 HIC values were 63% and 95% larger than Vendor 1 and eBee+ HIC values, respectively. Thus, when looking at the risk of severe head injury and skull fracture, heavier and more stiff vehicles pose the greatest risk. However, the same was not true for more mild injuries such as concussion. Compared to the Phantom 3, the eBee+ had only 5% lower BrIC values. Additionally, the Vendor 1 had only 23% lower VT-CP values than did the Phantom 3. Thus, while

²⁵ McCrory, P., Meeuwisse, W., Dvorak, J., Aubry, M., Bailes, J., Broglio, S., ... & Davis, G. A. (2017). Consensus statement on concussion in sport—the 5th international conference on concussion in sport held in Berlin, October 2016. *Br J Sports Med*, bjsports-2017.

²⁶ Hernandez, F., Wu, L. C., Yip, M. C., Laksari, K., Hoffman, A. R., Lopez, J. R., ... & Camarillo, D. B. (2015). Six degree-of-freedom measurements of human mild traumatic brain injury. *Annals of biomedical engineering*, 43(8), 1918-1934.

²⁷ Sanchez, E. J., Gabler, L. F., McGhee, J. S., Olszko, A. V., Chancey, V. C., Crandall, J. R., & Panzer, M. B. (2017). Evaluation of head and brain injury risk functions using sub-injurious human volunteer data. *Journal of neurotrauma*, 34(16), 2410-2424.

lightweight and flexible UAS may not pose a risk for severe head injuries, they still display the potential to cause minor brain injuries.

Table 10 – Average (SD) injury criteria values by UAS vehicle

| UAS Vehicle | HIC | BrIC | VT-CP |
|-------------|----------------|----------------|---------------|
| Phantom 3 | 1713 (1393) | 0.42 (0.10) | 0.99 (0) |
| Mavic Pro | 2972 (1331) | 0.31 (0.08) | 1.00 (0) |
| eBee+ | 84 (43) | 0.40 (0.11) | 0.26 (0.4) |
| Vendor 1 | 634 (483) | 0.17 (0) | 0.76 (0.4) |
| Inspire 2 * | 237 | 0.53 | 0.81 |

4.5 UAS Impact Variation

UAS impact orientation and location were found to play a large role in PMHS head kinematics. When comparing UAS impact orientation and impact location for several scenarios, large variations in kinematics between tests were associated with large differences in UAS impact orientation/location. Several comparisons of UAS location variation, relative to PMHS head CG, are shown in Figure 30 and Figure 31. Impact orientation data for additional tests are given in APPENDIX C—.

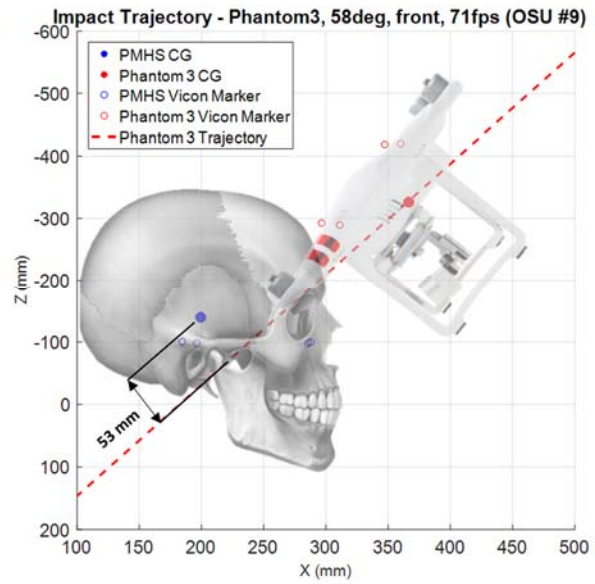
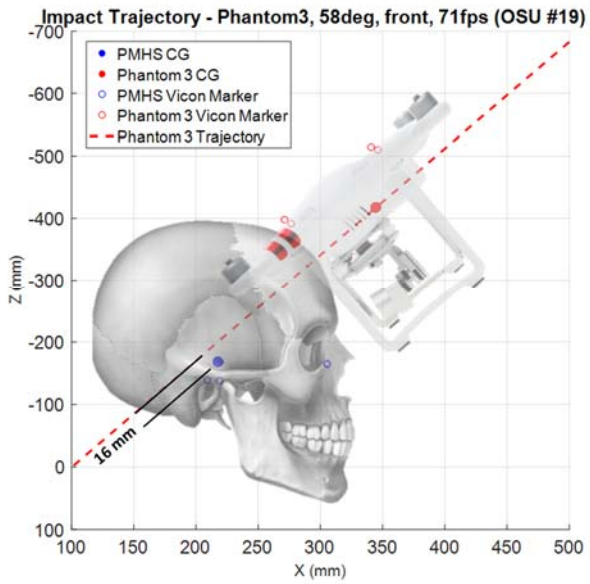


Figure 30 – Impact location variation relative to PMHS CG for 58-degree, Phantom 3 impacts

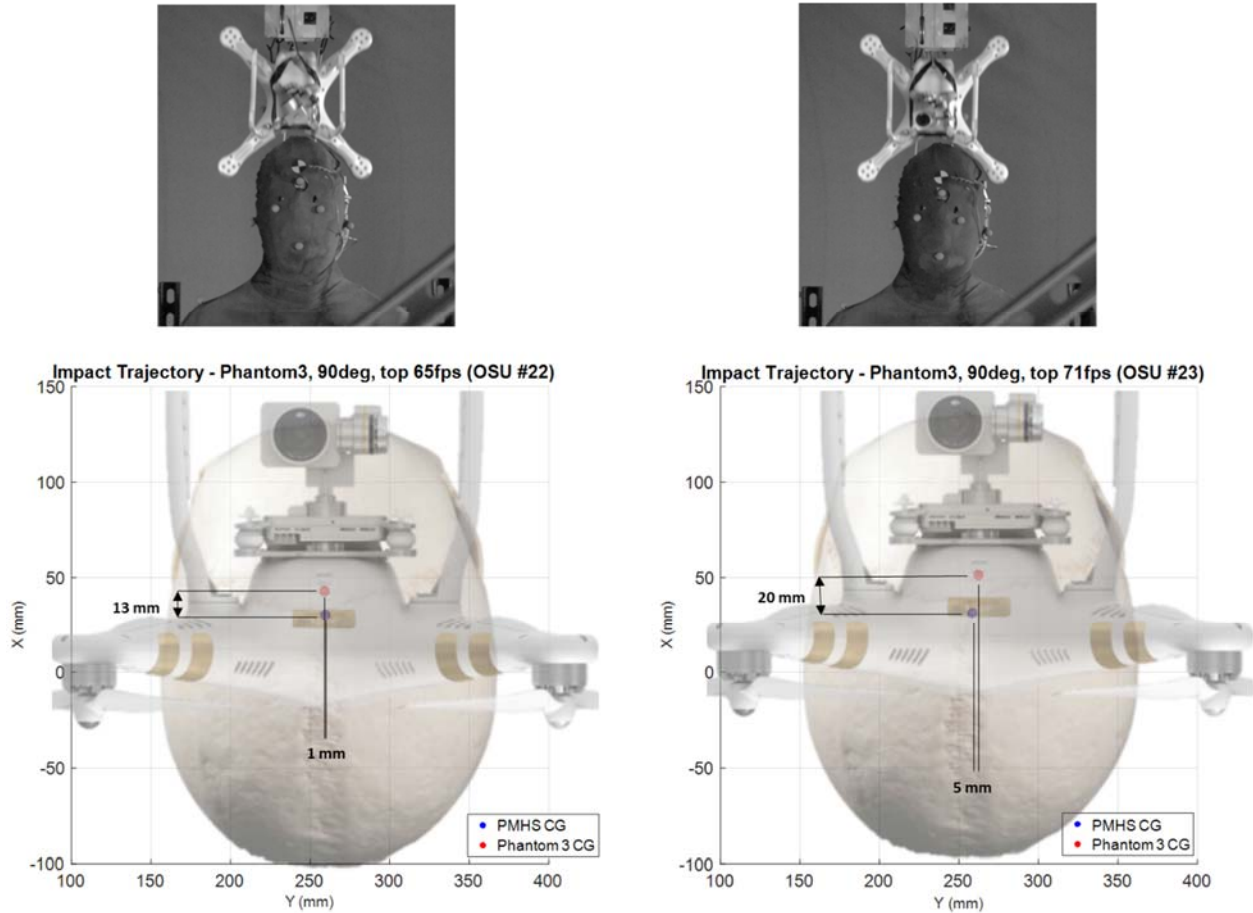


Figure 31 – Impact location variation relative to PMHS CG for 90-degree, Phantom 3 impacts

The impact location variation for 58-degree impacts in Figure 30 was attributed to differences in PMHS head shape and initial seating position. However, impact location variation for 90-degree impacts, displayed in Figure 31 was attributed to UAS drift during free flight. In this comparison, subject head shape remained constant as both tests were conducted on PMHS03. Additionally, comparison of pre-test FARO data indicated less than 2mm variation in initial head position between the two tests. Comparisons of UAS impact orientations are displayed in Figure 32 and Figure 33.

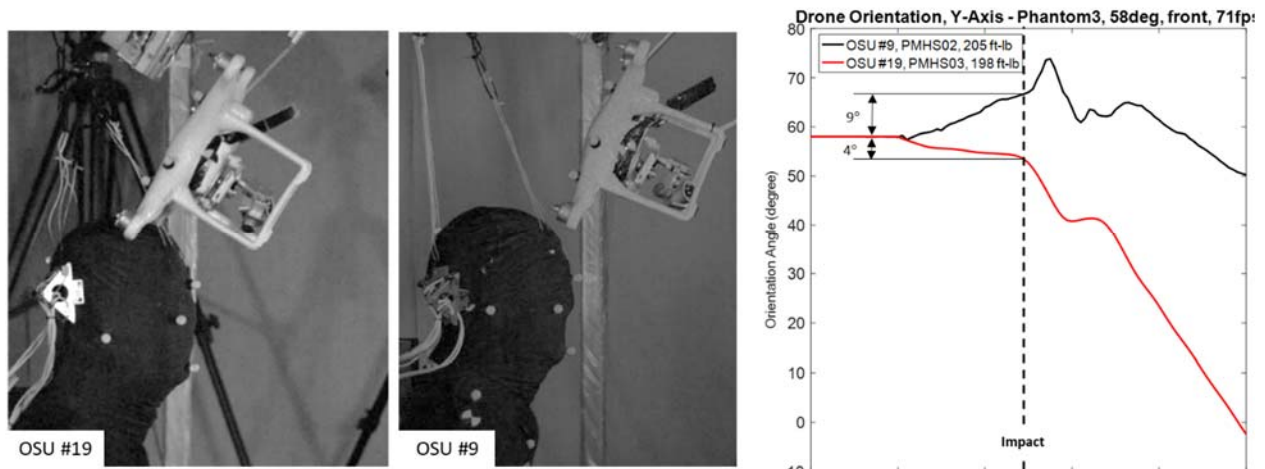


Figure 32 – UAS impact pitch angle variation for 58-degree, Phantom 3 impacts

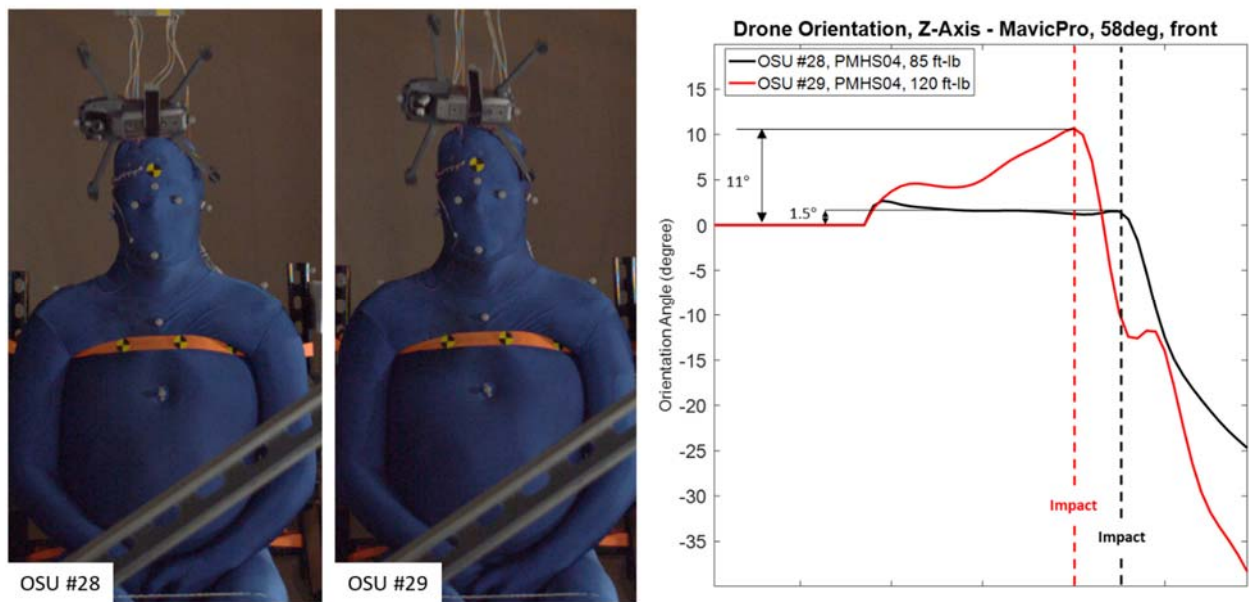


Figure 33 – UAS impact yaw angle variation for 58-degree, Mavic Pro impacts

In addition to the variation in impact location observed in Figure 30, UAS orientation also varied in the 58-degree Phantom 3 case, shown in Figure 32. This variation in UAS orientation was attributed to instrumentation mounted to the Phantom 3 for OSU #9. The instrumentation wires created drag on the UAS, causing a downward pitch; instrumentation was removed in future tests for this reason. However, similar to variation observed in Figure 31, UAS orientation differences in 58-degree Mavic Pro impacts were attributed to UAS rotation during free flight.

Table 11 displays a comparison of head kinematics for tests in which UAS orientation or location misalignments were observed. For 58-degree frontal impacts with the Phantom 3, a 267% increase in linear acceleration peaks was observed between tests. This was at least partly attributable to the difference in impact location and orientation between the two tests seen in Figure

30 and Figure 32. However, the tests were conducted on separate PMHS, thus variation in individual subject response could have also played a role in these differences. Despite the large changes observed in linear acceleration, angular velocity and angular acceleration peaks were less affected. This indicates that much of energy transferred from UAS to PMHS is expressed through the linear acceleration response. Furthermore, this indicated that for impacts that are not “worst case” the risk of brain injury remains present due to the high angular kinematics observed. In 90-degree, Phantom 3 and 58-degree, Mavic Pro comparisons, the PMHS subject was the same; however, the impact kinetic energy was different between tests. In both cases, the test with the higher kinetic obtained lower linear acceleration peaks. This is due to misalignment between UAS CG and PMHS CG. Yet, angular kinematics still follow the same trend as the kinetic energy. While minor brain injury remains a risk in most UAS impact scenarios, small variations away from “worst case” impacts can have a large effect on the risk of more severe injuries such as skull fracture. Therefore, work is needed to define how likely these “worst case” impacts are to occur in real life.

Table 11 – Comparison between UAS impact orientation/location and head kinematics

| PMHS # | Impact Configuration | Impact Variation | Percent Change (%) | | | |
|--------|---------------------------------|----------------------------------|--------------------|-------------------------|----------------------------|--|
| | | | Impact KE (ft-lb) | Linear Acceleration (g) | Angular Velocity (deg/sec) | Angular Acceleration (rad/sec ²) |
| PMHS02 | Phantom 3, 58°, frontal, 71ft/s | 9° pitch downward, 2.1 in offset | -3.5% | +267% | +8.0% | +19.0% |
| PMHS03 | Phantom 3, 58°, frontal, 71ft/s | 4° pitch upward, 0.63 in offset | | | | |
| PMHS03 | Phantom 3, 90°, top, 65ft/s | .51 in offset | +18.5% | -13.7% | +3.4% | +18.9% |
| PMHS03 | Phantom 3, 90°, top, 71ft/s | .81 in offset | | | | |
| PMHS04 | Mavic Pro, 58°, front, 61ft/s | 2° yaw | +41.1% | -2.4% | +9.9% | +1.8% |
| PMHS04 | Mavic Pro, 58°, front, 71ft/s | 11° yaw | | | | |

Note: Percent change calculations made relative to the 1st test in each scenario.

4.6 Skull Deformation

Through a comparison between the 6 ω tetrahedron array and the redundant 3 ω array on the PMHS skull, it was determined that the skull may not be acting as a rigid body during severe impacts. Large differences were observed between the two sensor arrays, especially in side impacts, as noted in Figure 34(b). This is likely due to the sensors’ mounting position as well as deformation of the skull during severe impacts. This deformation has been described as the “hoop effect” in other studies.²³ The “hoop effect” may alter the kinematic measurements of sensors which are mounted lateral to the direction impact, shown Figure 35. This effect is manifested as

high, oscillatory angular acceleration peaks, which can have an effect on kinematics when peripheral sensor data is transformed to the head CG.²⁸ Comparisons in this study indicate that sensors are in better agreement when kept away from the impact location, as was the case in frontal impact scenarios.

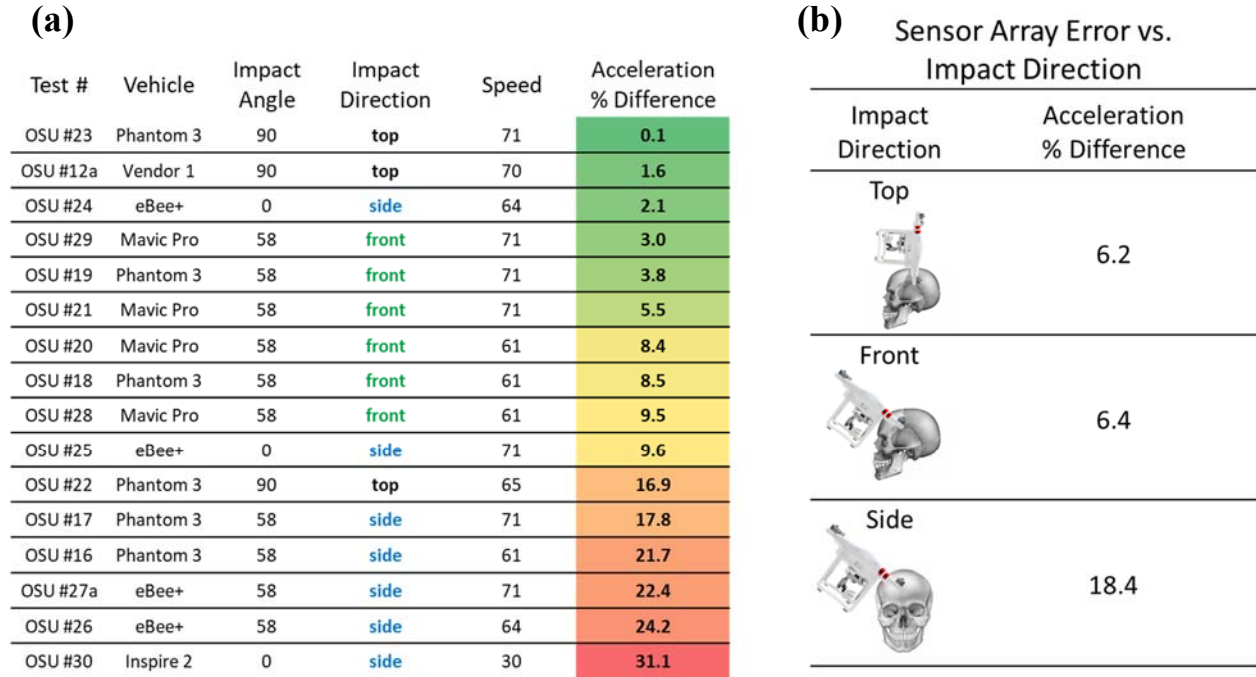


Figure 34 – Comparison between $6a\omega$ tetrahedron array and redundant $3a\omega$ array (a) from smallest to largest percent difference, (b) averaged by impact direction

²⁸ Nusholtz, G. S., Lux, P., Kaiker, P., & Janicki, M. A. (1984). Head impact response—Skull deformation and angular accelerations. *SAE transactions*, 800-833.

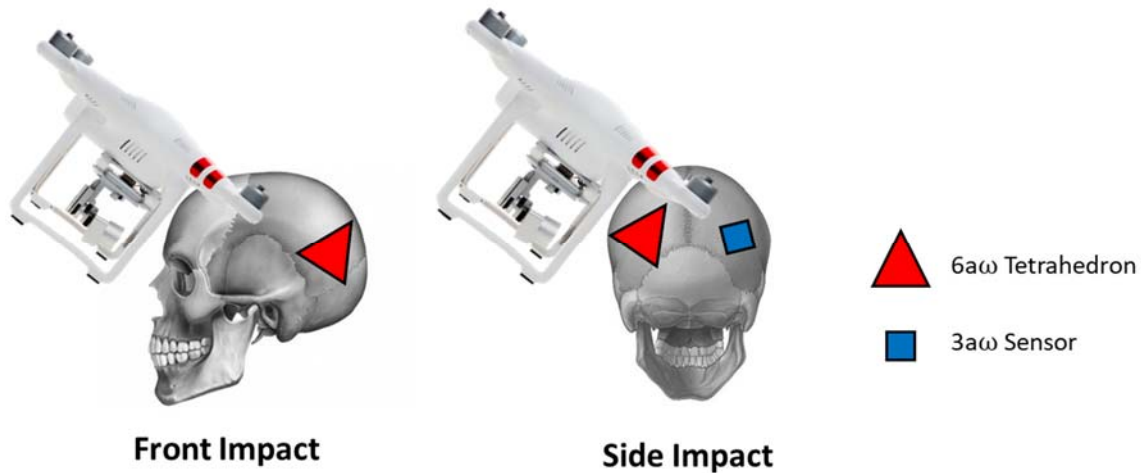


Figure 35 – Approximate locations of $6a\omega$ array and $3a\omega$ for PMHS tests

Despite the effect of skull deformation, PMHS head kinematics in the current study are comparable to previously published work shown in Figure 36.^{29,30} This could indicate that some amount of skull deformation is present in many previous PMHS head impact experiments. Skull deformation present in previous studies would have an effect on the kinematics which are used as limits and criteria to predict injury. Future investigations involving UAS injury assessments should evaluate methods for reducing the effect of skull deformation on kinematic measurements. Variables to be investigated include sensor array design, sensor attachment methods, and post-processing techniques. Results would be applicable to the UAS industry as well as the automotive safety industry.

²⁹ Prasad, P., & Mertz, H. J. (1985). The position of the United States delegation to the ISO Working Group 6 on the use of HIC in the automotive environment. *SAE transactions*, 106-116.

³⁰ Yoganandan, N., Zhang, J., Pintar, F. A., Gennarelli, T. A., Kuppa, S., & Eppinger, R. H. (2003). Biomechanics of lateral skull fracture. In *Proceedings of the IRCOBI*.

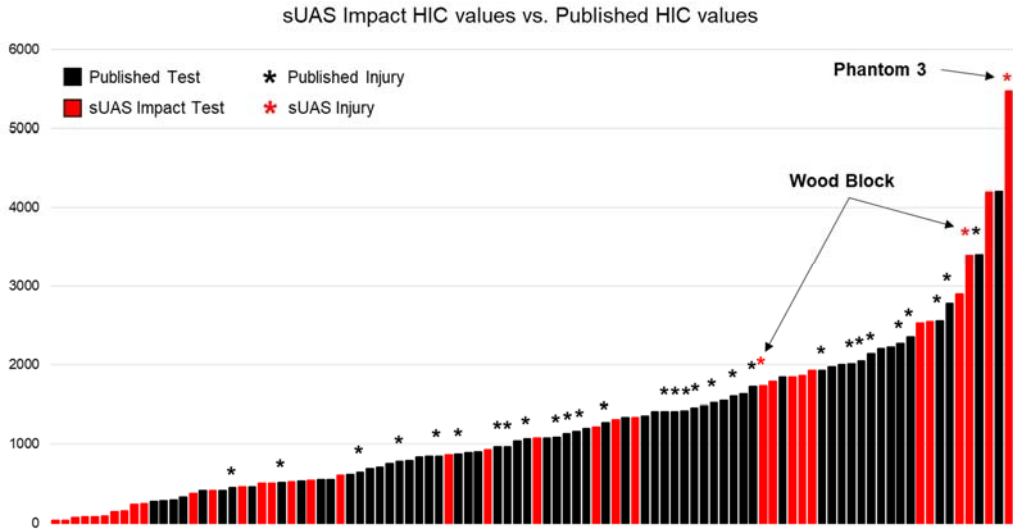


Figure 36 – Comparison of UAS impacts to previously published head injury studies

5. LIMITATIONS

While the present work helps define the kinematic response and human injury thresholds in UAS impact scenarios, several limitations must be acknowledged. To maximize the number of vehicles tested, multiple impacts were conducted on the same PMHS subject. It is possible that microdamage within calvarium from successive impacts led to a decrease in fracture tolerance; however, as the first study examining PMHS injury thresholds in UAS impacts, this conservative approach was deemed acceptable. PMHS subjects were also restrained below the 4th thoracic vertebra. This boundary condition limits the motion of the thorax, pelvis, and lower extremities in response to impact. However, these constraints would likely cause most of the impact energy to be absorbed by the subjects' head and neck and could be viewed as a “worst-case” condition. Additionally, post-mortem changes to subjects' brains were assumed to not significantly affect head kinematics during this study. This assumption was supported by the short duration peaks observed in head kinematics, indicating that any brain motion occurred after the main response of each PMHS. Finally, skull deformation could affect head kinematics measured during this study. However, the extent to which kinematics were altered is unknown and requires further investigation. Nonetheless, the results of this study provide an initial assessment of injury risk in UAS impact scenarios.

6. CONCLUSIONS & RECOMMENDATIONS

From this study, several overall conclusions and recommendations can be made:

1. During the 35 UAS impacts carried out during this study, only one AIS 2+ skeletal injury was observed: a 5.1-inch AIS 2 level skull fracture of the frontal bone. The injury occurred on a 71 ft/s, 58°, frontal impact with the DJI Phantom 3. The occurrence of this injury indicates that UAS impacts with the uninvolved public may pose a threat to public safety.

- a. **Recommendation:** More testing is needed to determine the specific prevalence and probability associated with skull fracture injuries in UAS impact scenarios.
2. Kinematics measured during PMHS tests indicate that automotive injury metrics may not be able to accurately predict skull fracture in the UAS scenario. To assess the risk of skull fracture, the Head Injury Criteria (HIC) and its associated risk curve were compared to PMHS head kinematics. Based on the HIC criteria, 5 UAS impacts had greater than an 85% probability of causing a skull fracture; yet only 1 skull fracture was observed.
 - a. **Recommendation:** Additional investigation is needed to determine appropriate criteria or limits to be used for predicting the severity of head injuries in UAS impact scenarios.
3. The proposed head acceleration limit of 198g is a conservative limit according to PMHS test data. Of the 35 UAS tests conducted on 4 separate PMHS, 17 tests recorded linear accelerations above 198g. Of these 17 tests, only 1 skull fracture was observed. Based on a simple analysis of probability, 198g corresponds to about a 6% risk of sustaining a skull fracture due to UAS impact.
4. Based on injury criteria developed to predict concussions in the football and automotive environments, most UAS impacts were likely to cause a concussion. However, current concussion diagnosis is based on verbal and motor skills tests, something not possible in PMHS testing. Thus, while UAS impacts caused concussion level kinematics, actual concussions could not be assessed in this scenario.
5. The risk of concussion associated with UAS impacts was dependent upon which concussion metric was being used. For example, according to the Brain Injury Criteria (BrIC), eBee+ vehicles averaged a 99% chance of causing a concussion; whereas, according to the Virginia Tech Concussion Probability Metric, eBee+ averaged only a 26% chance of causing a concussion.
 - a. **Recommendation:** Due to inconsistency between concussion metrics measured during PMHS testing, as well as disagreement within the scientific community concerning which metric is more accurate, a concussion threshold for use in regulatory standards should be delayed until such a time when a more definitive and consensus-based criterion has been established.
6. The injury potential of a UAS impact depends on which vehicle model is being used as well as which injury mechanism is being investigated. Vehicles with less mass and lower stiffness characteristics, such as the eBee+ and Vendor 1 displayed a low risk of skull fracture, while heavier and stiffer vehicles such as the Phantom 3 and Mavic Pro incurred a higher risk of skull fracture. However, lightweight and flexible vehicles still display the potential to cause minor injuries such as concussion.
7. Small changes in UAS impact orientation and impact location were found to cause large changes in impact energy transfer. For example, a 9° pitch downward during a 58°, Phantom 3 test caused a 73% reduction in linear acceleration of the head.

- a. **Recommendation:** While head injuries may occur as a result of UAS impacts, work is needed to define how likely these “worst case” impacts are to occur real life.

8. Localized skull deformation during UAS impacts may have influenced kinematic measurements used to predict injury risk. By comparing measurements from 2 sensor arrays mounted on the skull periphery during UAS impacts, it was determined that the skull may deform upon impact and thus not act as a rigid body. The deformation of the skull caused an average difference of 6% between the two sensors.
 - a. **Recommendation:** Future investigations involving UAS injury assessments should evaluate methods for reducing the effect of skull deformation on kinematic measurements. Variables to be investigated include sensor array design, sensor attachment methods and post-processing techniques. Results would be applicable to the UAS industry as well as the automotive safety industry.

9. **Recommendation:** Due to the large scope of vehicles, test orientations and impact locations selected for this testing, few strong conclusions can be drawn concerning the risk of injury associated with UAS head impacts. It is recommended that future UAS impact studies focus on more clearly defining the injury thresholds and risks associated with UAS collisions. To accomplish this, probabilistic modelling can be employed to develop injury risk curves which define the likelihood of sustaining an injury based on parameters which are specific to UAS impacts. Parameters which are likely to affect injury risk in UAS failure scenarios include the impacting vehicle’s stiffness, geometry and impact location. A UAS vehicle’s stiffness affects its impact energy transfer properties, thus affecting the risk of both skull and brain injury. The vehicle’s geometry defines its impact contact area, which may create localized stresses within the cranium depending on UAS shape (i.e point-load contact). Finally, impact location may affect the risk of head and brain risk as different cranial bones have different fracture tolerances and brain injury tolerance has also been shown to be directionally dependent. Investigations of these parameters would allow for the development of a risk curve which accurately defines what is safe and unsafe in terms of UAS operation.

APPENDIX A— IMPACT RESPONSE STILL IMAGES

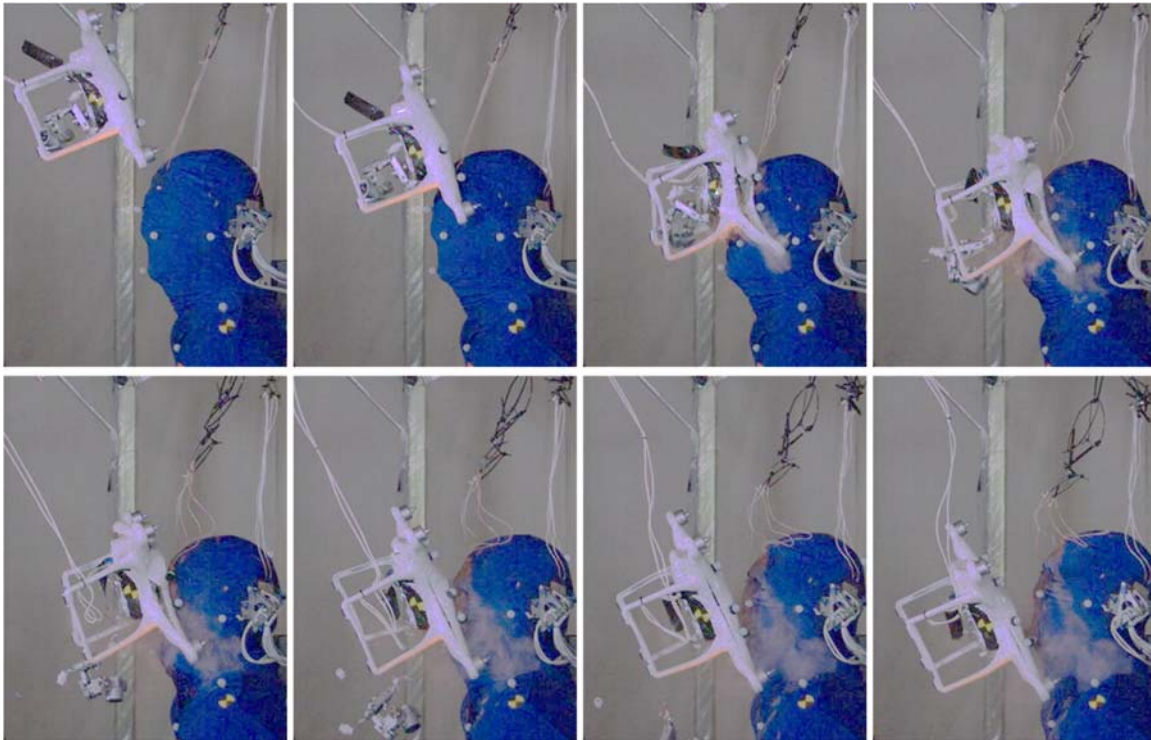


Figure 37 - Impact response of PMHS and Phantom 3 during a 58 degree, 71 ft/s, frontal impact, [5 millisecond time steps] (Test: OSU #9)

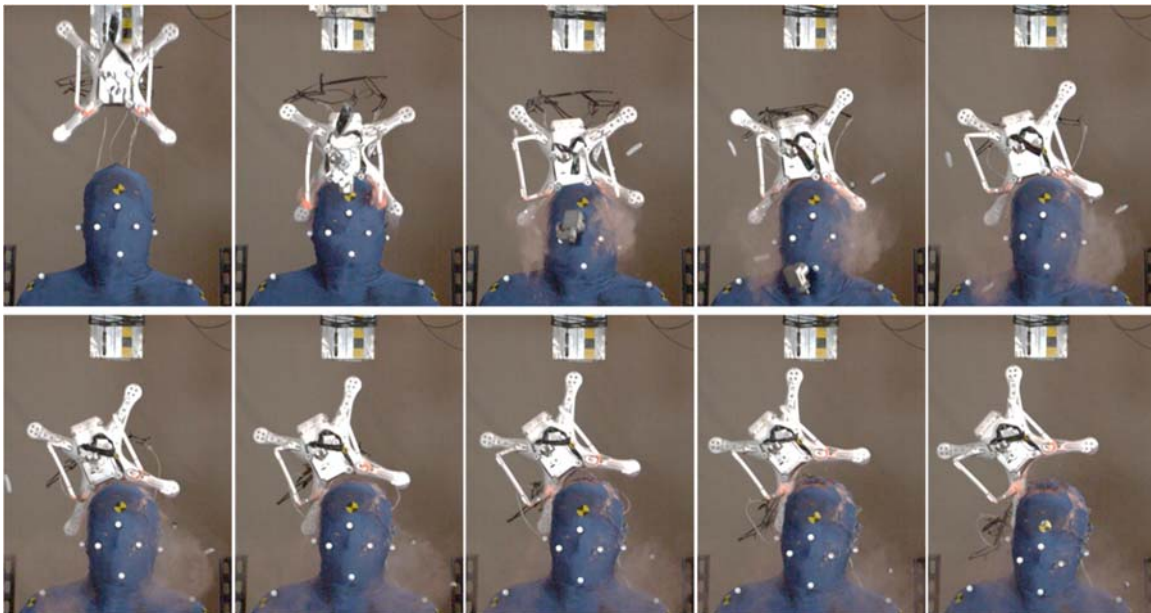


Figure 38 - Impact response of PMHS and Phantom 3 during a 90 degree, 71 ft/s, top impact, [10 millisecond time steps] (Test: OSU #15)

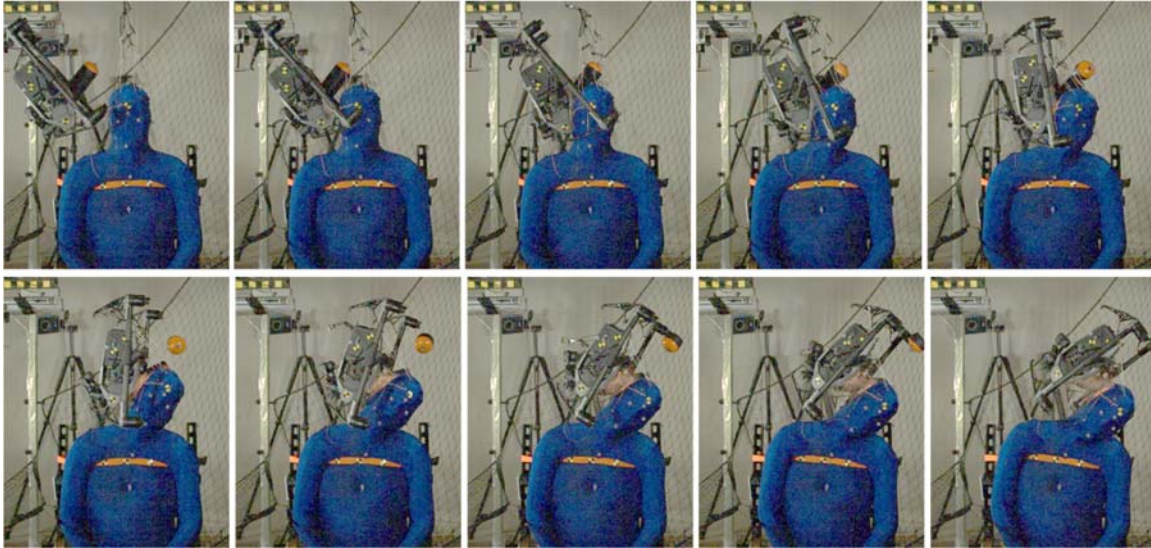


Figure 39 - Impact response of PMHS and Inspire 2 (Parachute) during a 0 degree, 30 ft/s, right side impact, [10 millisecond time steps] (Test: OSU #30)

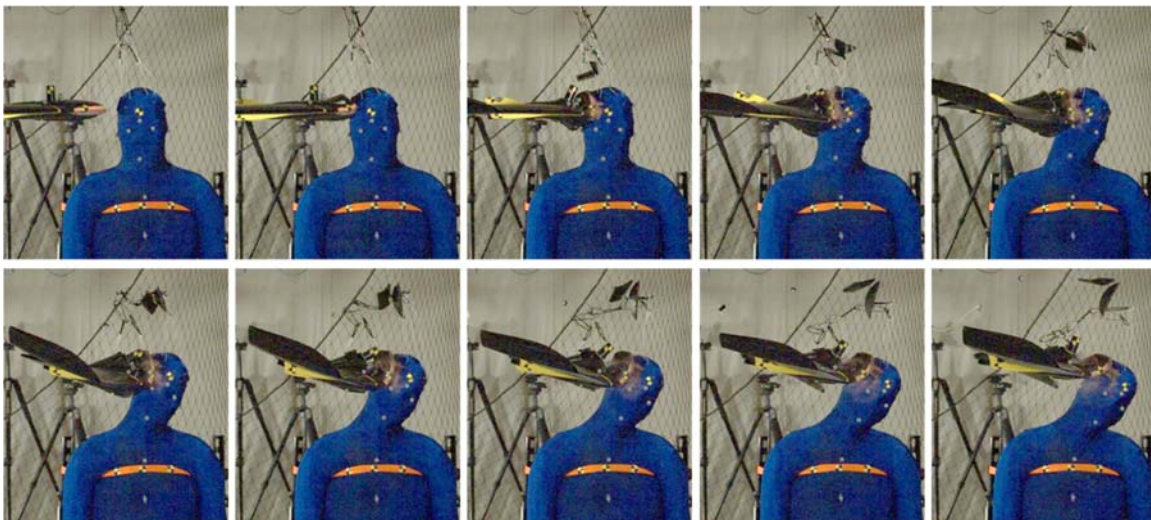


Figure 40 - Impact response of PMHS and eBee+ during a 0 degree, 71 ft/s, right side impact, [10 millisecond time steps] (Test: OSU #25)

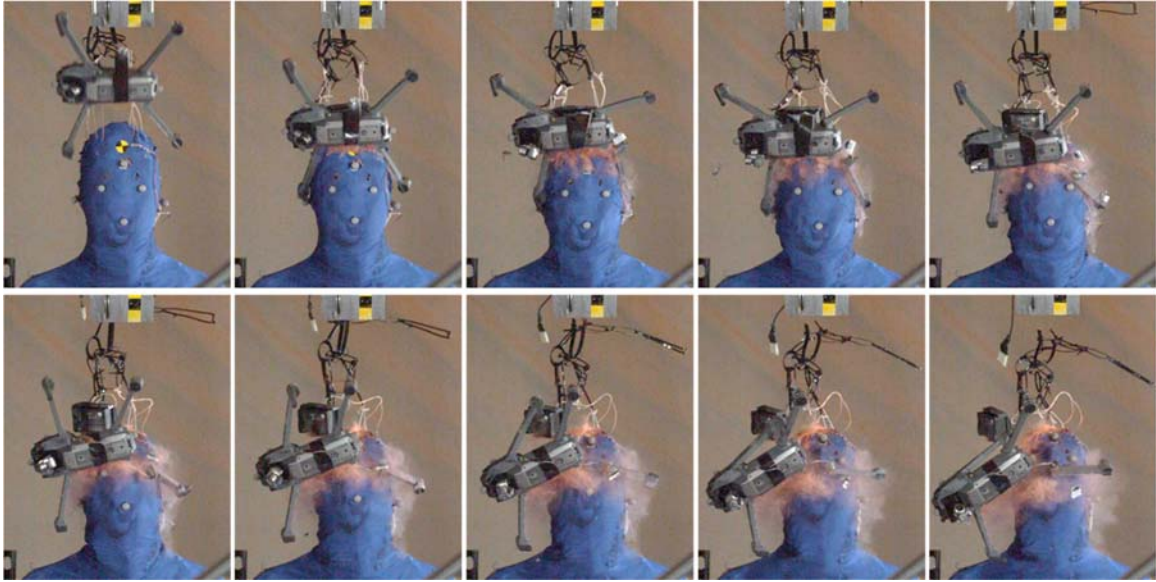


Figure 41 - Impact response of PMHS and Mavic Pro during a 58 degree, 71 ft/s frontal impact, [10 millisecond time steps] (Test: OSU #21)

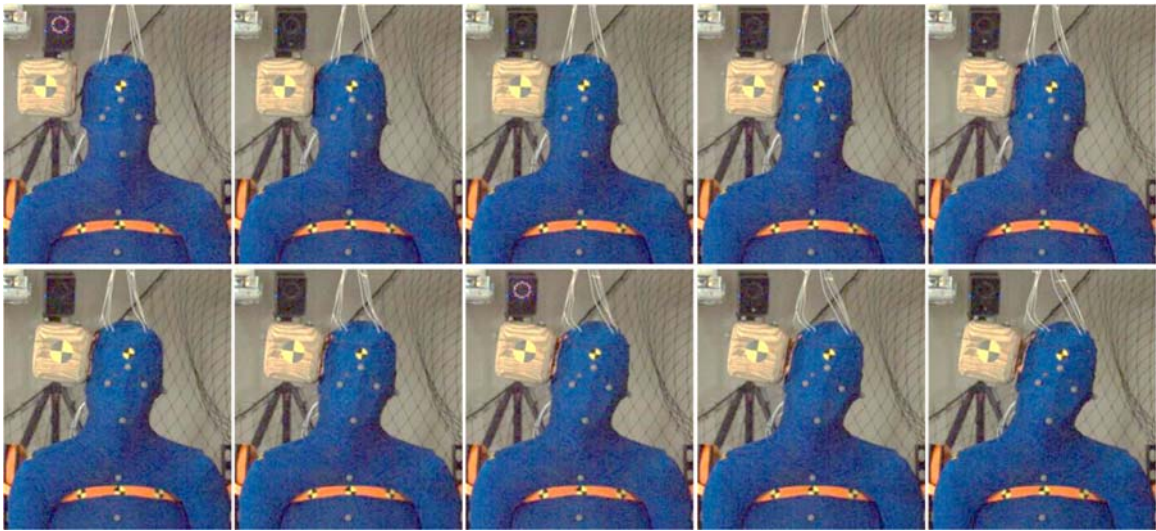


Figure 42 - Impact response of PMHS and Wood Block during a 0 degree, 40 ft/s right side impact, [5 millisecond time steps] (Test: OSU #33)

APPENDIX B—SUBJECT HEAD KINEMATIC TIME HISTORIES

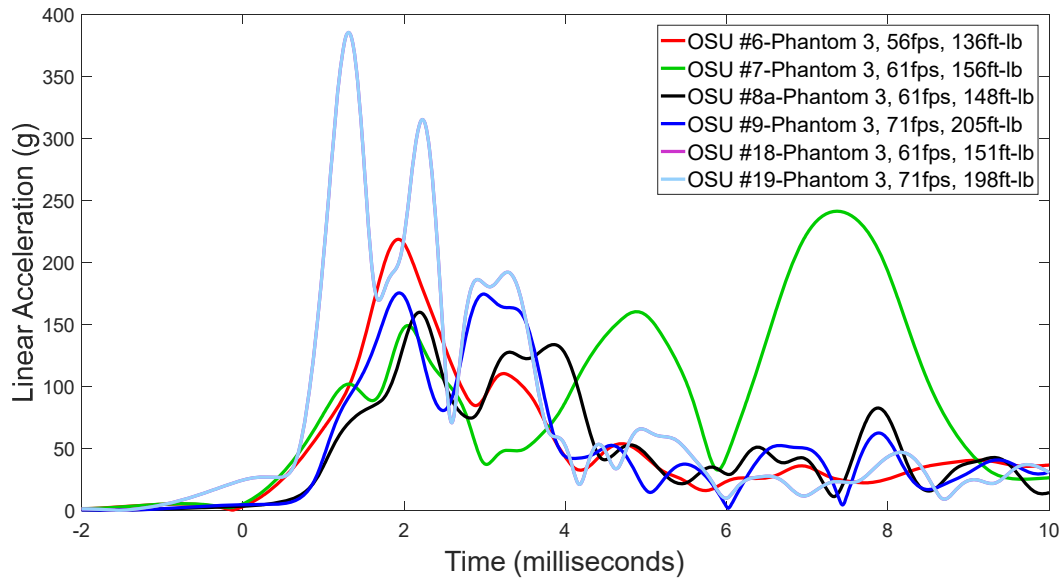


Figure 43 – Head resultant linear acceleration time histories in 58-degree, Phantom 3 frontal impact scenarios

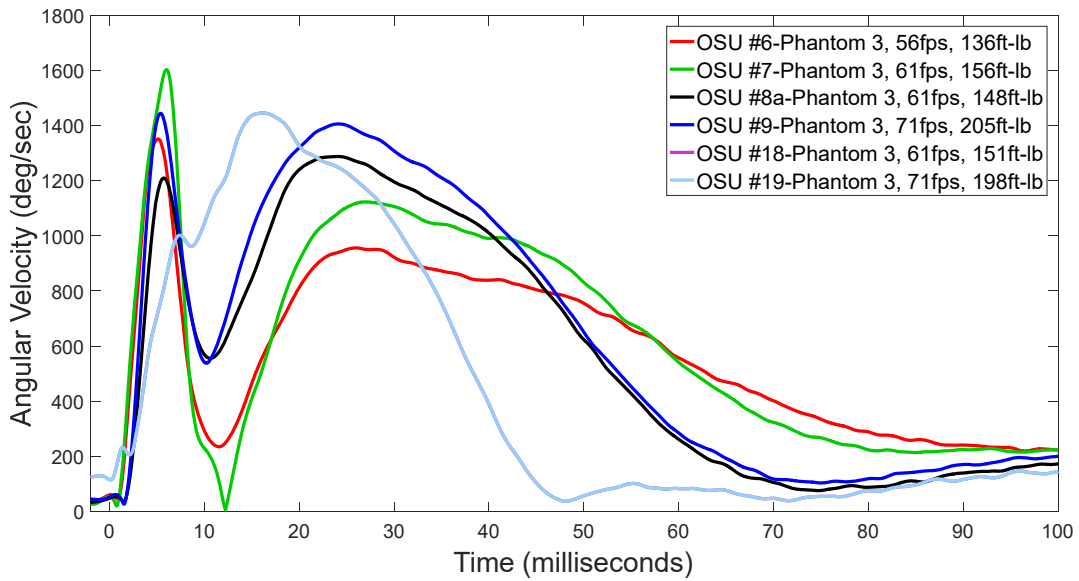


Figure 44 – Head resultant angular velocity time histories in 58-degree, Phantom 3 frontal impact scenarios

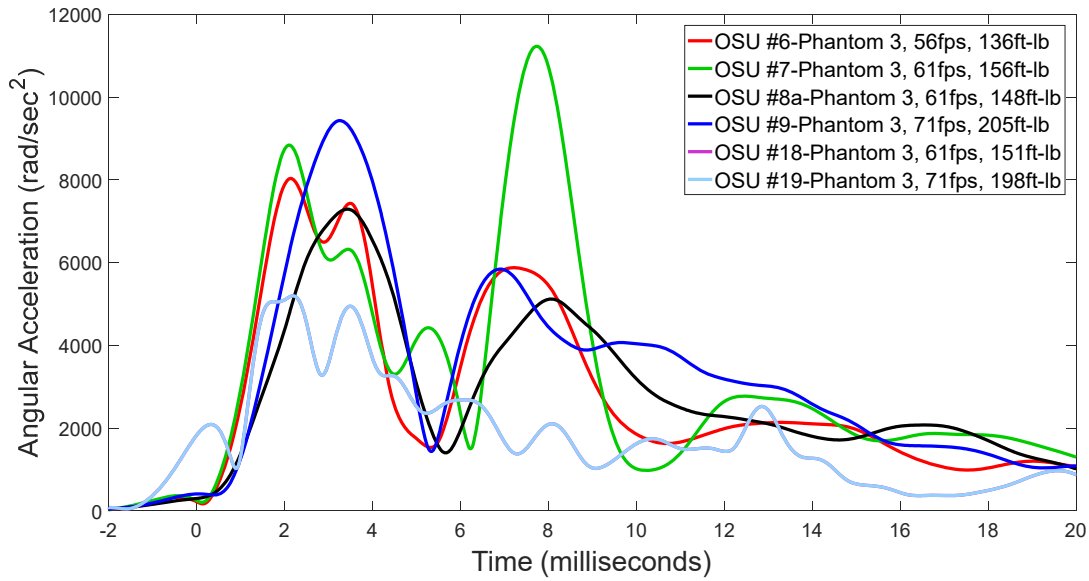


Figure 45 – Head resultant angular acceleration time histories in 58-degree, Phantom 3 frontal impact scenarios

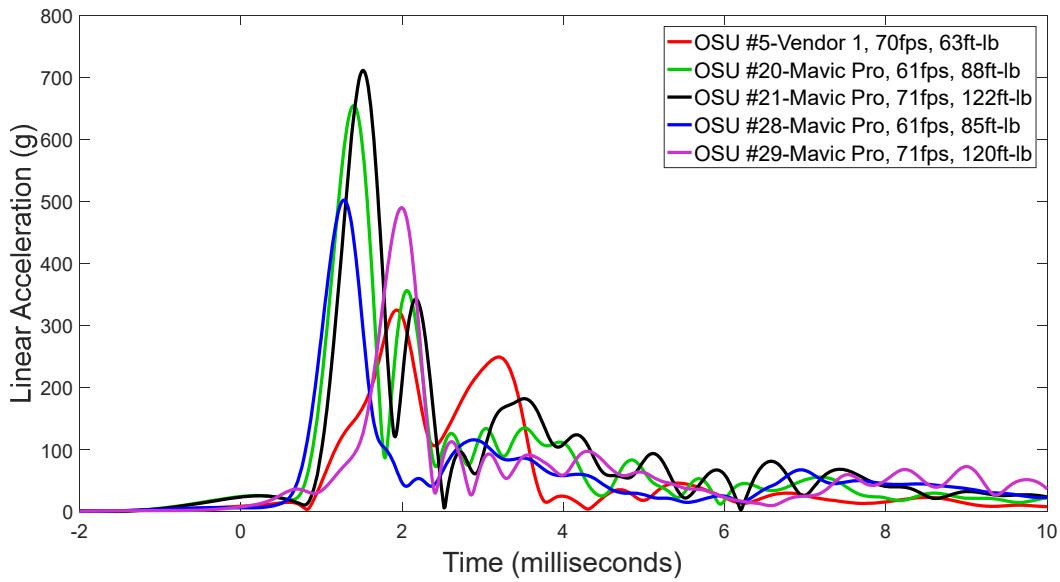


Figure 46 – Head resultant linear acceleration time histories in 58-degree, Mavic Pro frontal impact scenarios

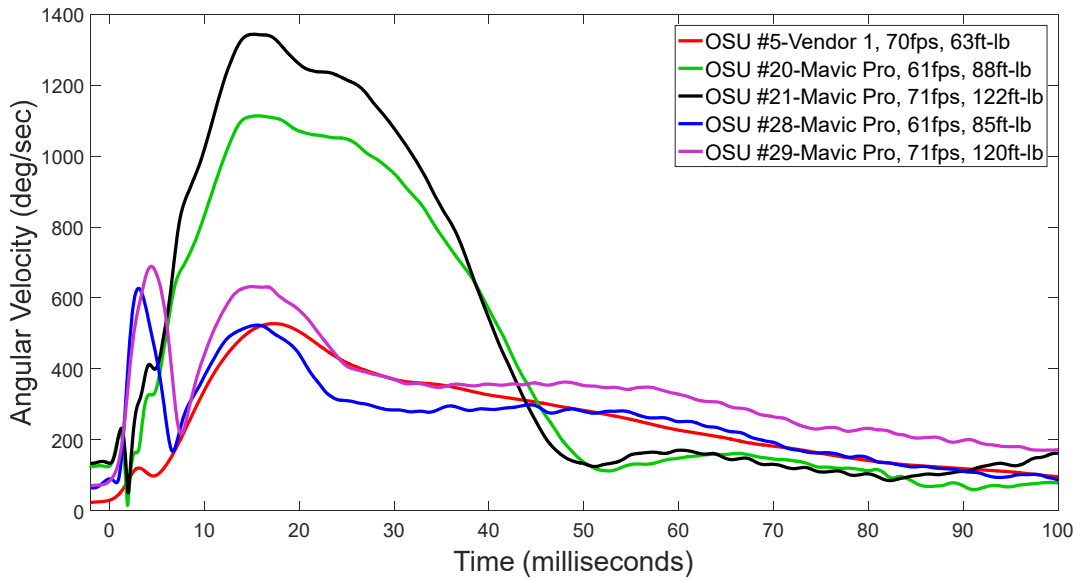


Figure 47 – Head resultant angular velocity time histories in 58-degree, Mavic Pro frontal impact scenarios

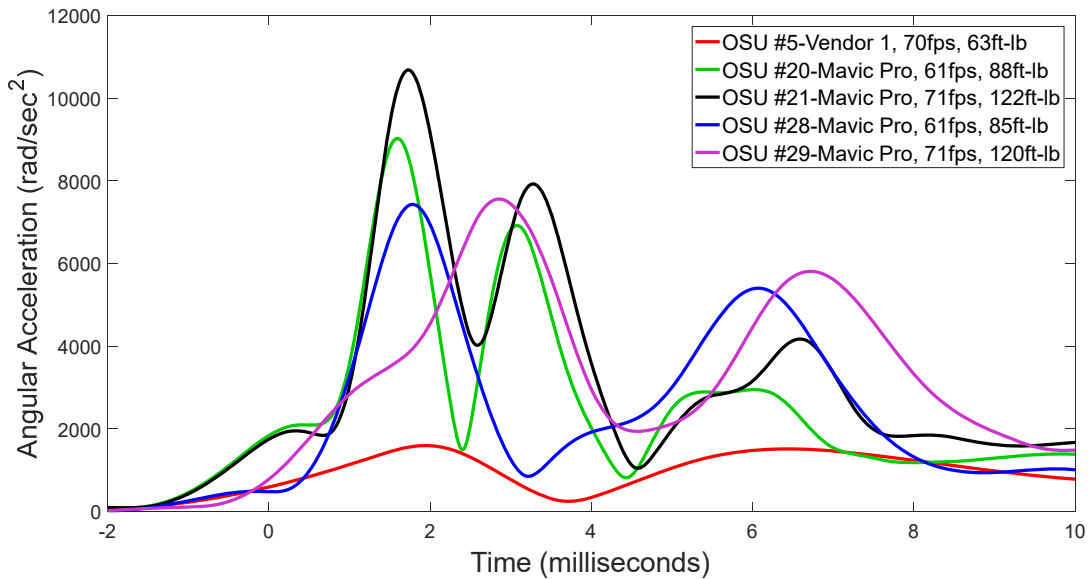


Figure 48 – Head resultant angular acceleration time histories in 58-degree, Mavic Pro frontal impact scenarios

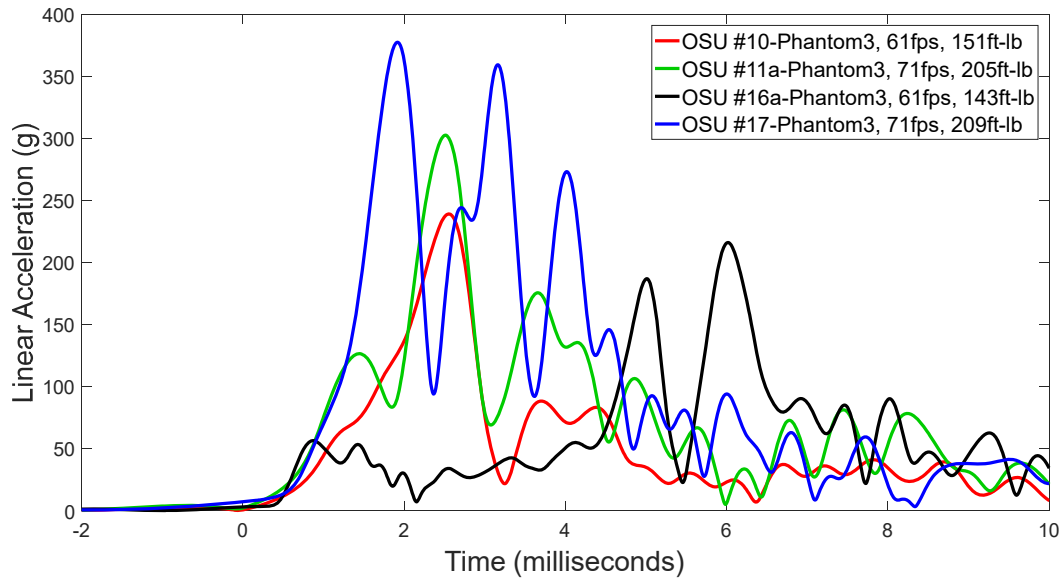


Figure 49 – Head resultant linear acceleration time histories in 58-degree, Phantom 3 right side impact scenarios

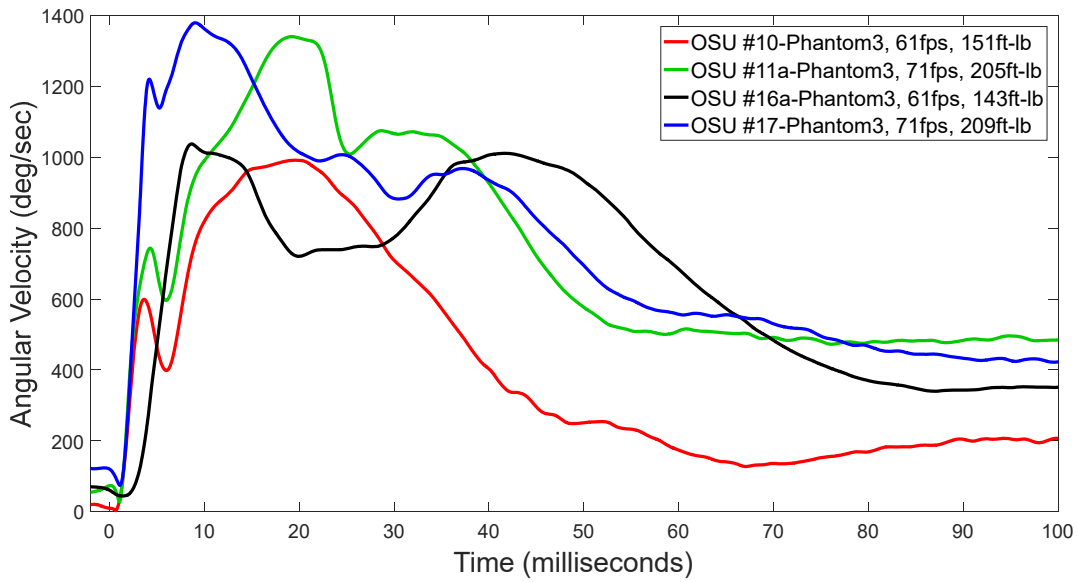


Figure 50 – Head resultant angular velocity time histories in 58-degree, Phantom 3 right side impact scenarios

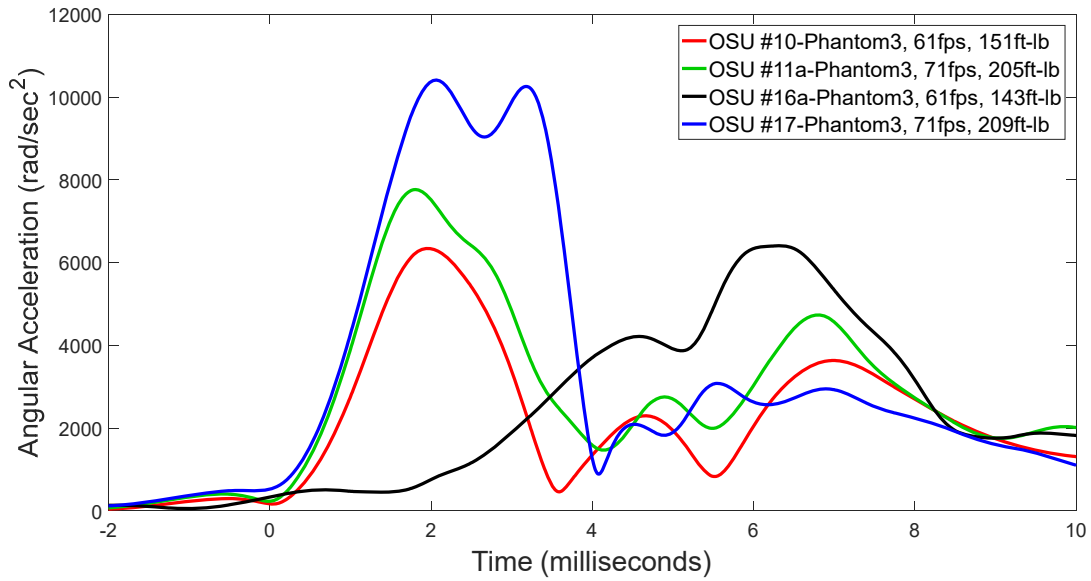


Figure 51 – Head resultant angular acceleration time histories in 58-degree, Phantom 3 right side impact scenarios

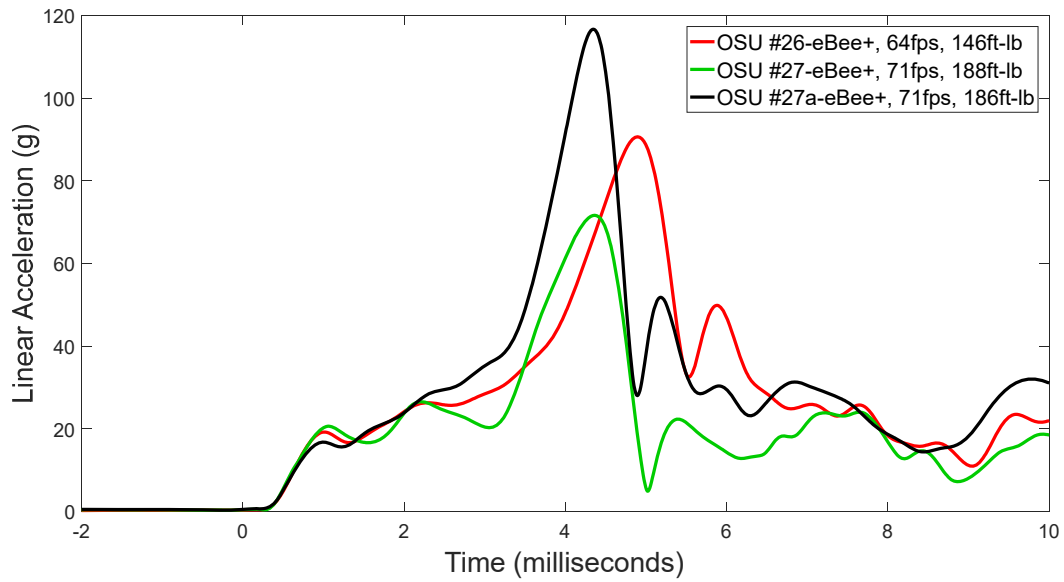


Figure 52 – Head resultant linear acceleration time histories in 58-degree, eBee+ left side impact scenarios

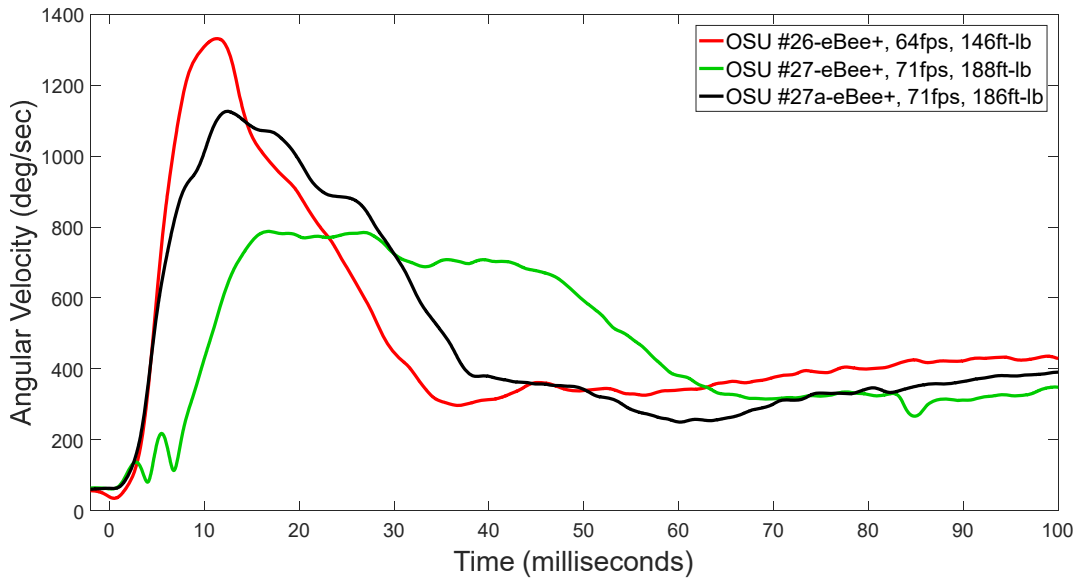


Figure 53 – Head resultant angular velocity time histories in 58-degree, eBee+ left side impact scenarios

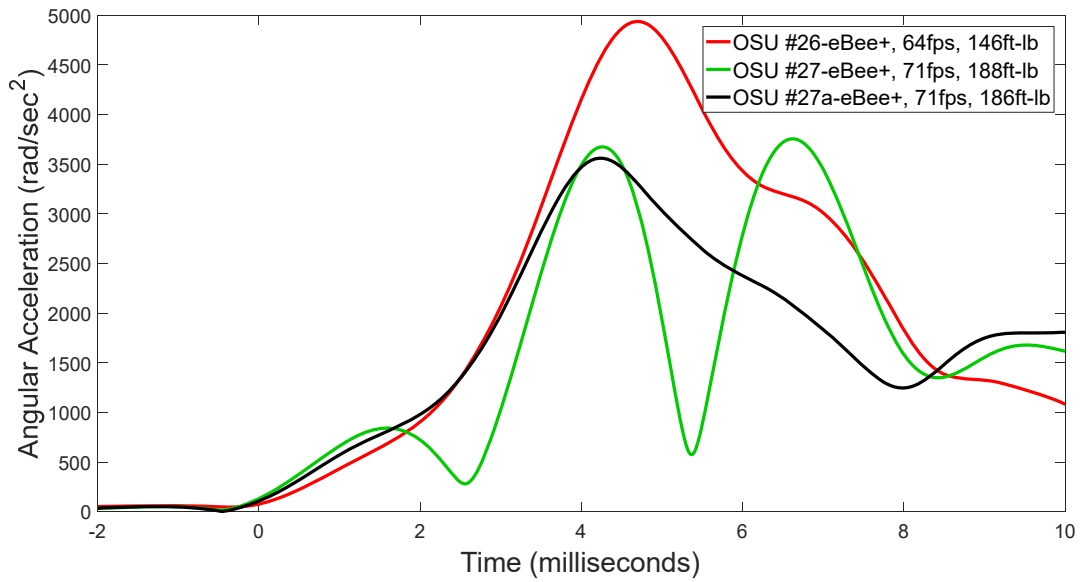


Figure 54 – Head resultant angular acceleration time histories in 58-degree, eBee+ left side impact scenarios

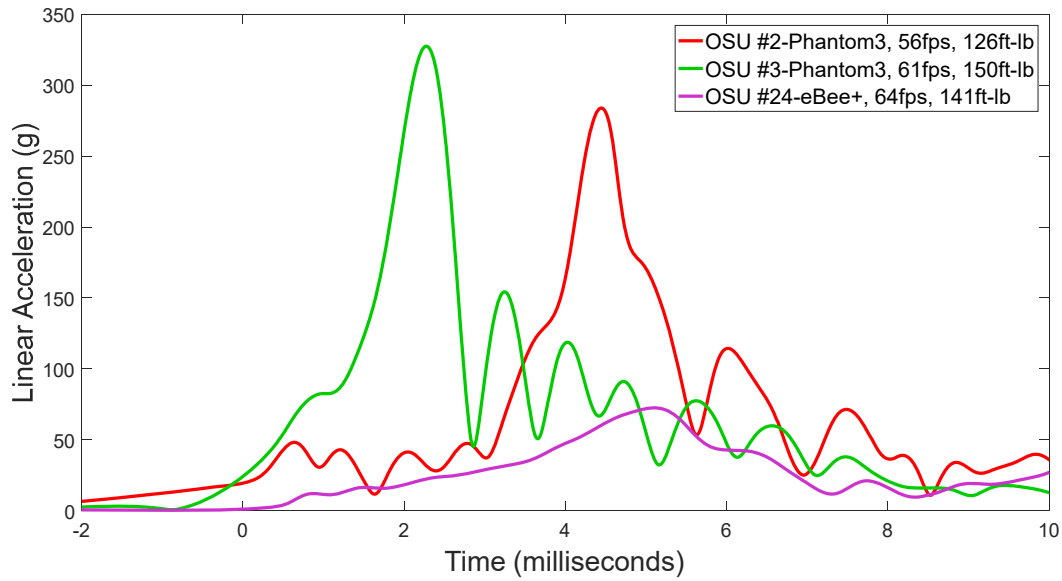


Figure 55 – Head resultant linear acceleration time histories in 0-degree, low speed, right side impact scenarios

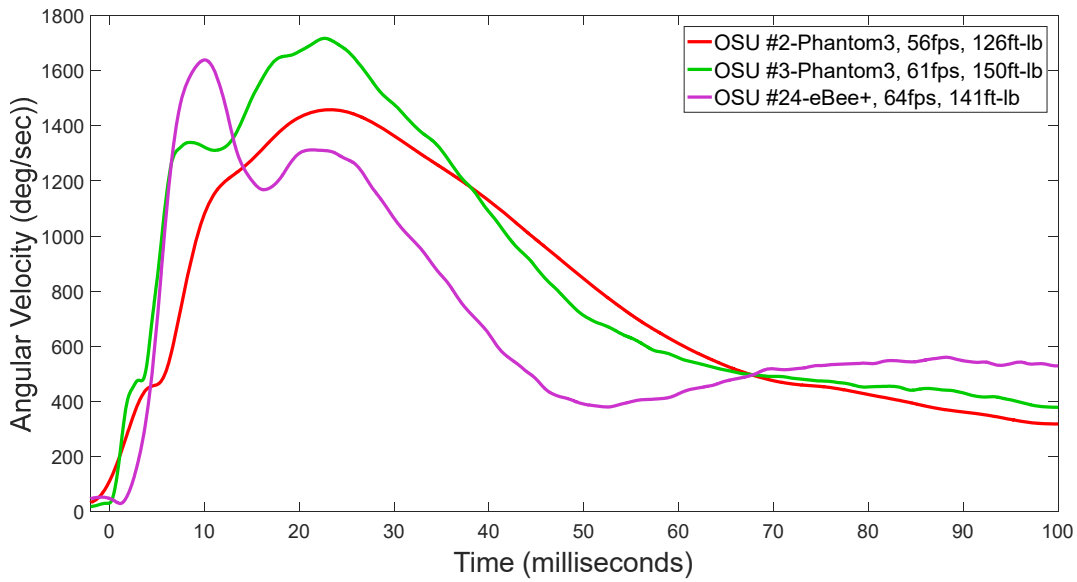


Figure 56 – Head resultant angular velocity time histories in 0-degree, low speed, right side impact scenarios

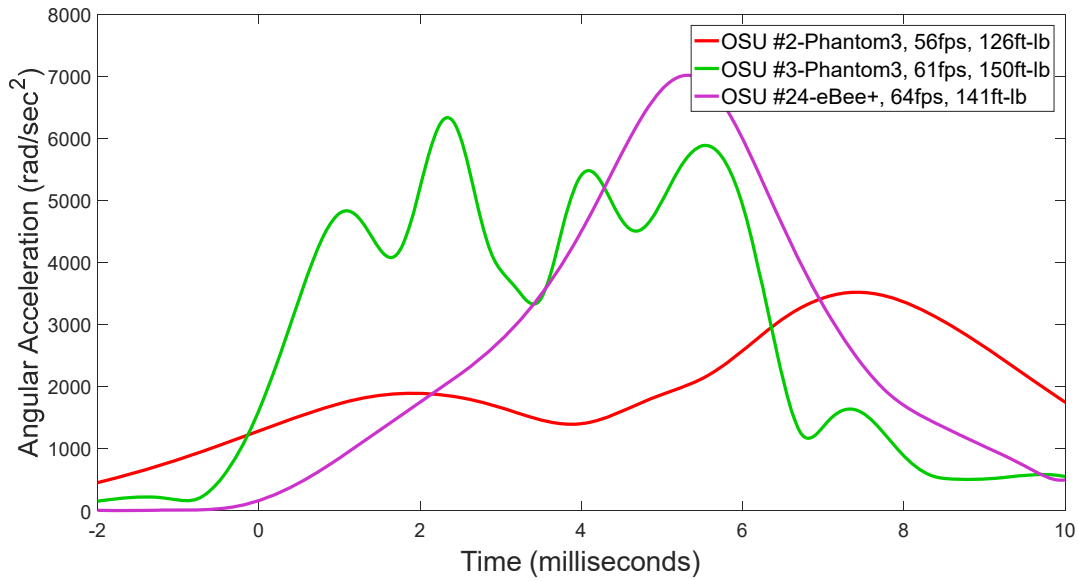


Figure 57 – Head resultant angular acceleration time histories in 0-degree, low speed, right side impact scenarios

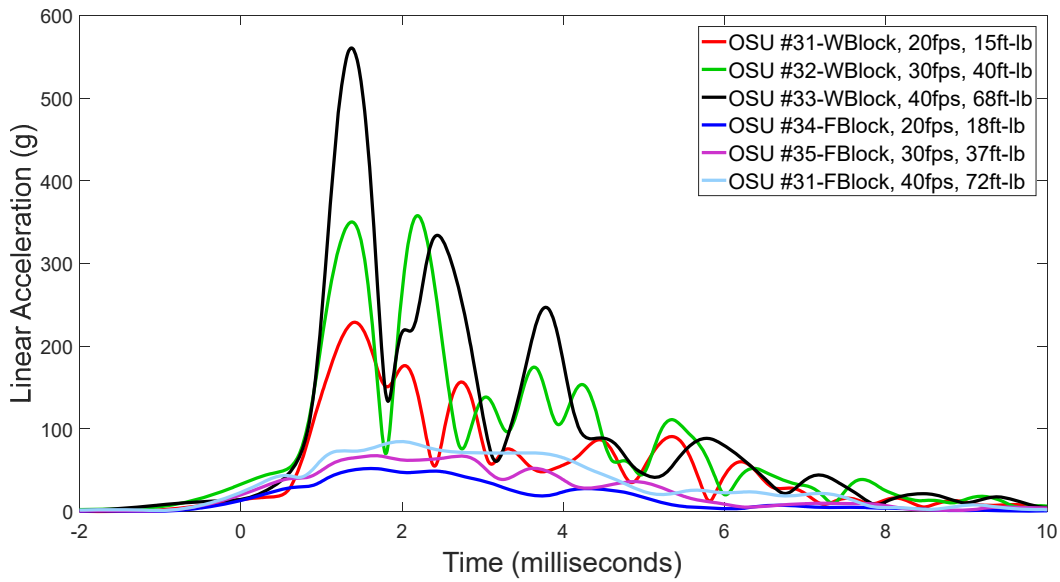


Figure 58 – Head resultant linear acceleration time histories in 0-degree, wood & foam block side impact scenarios

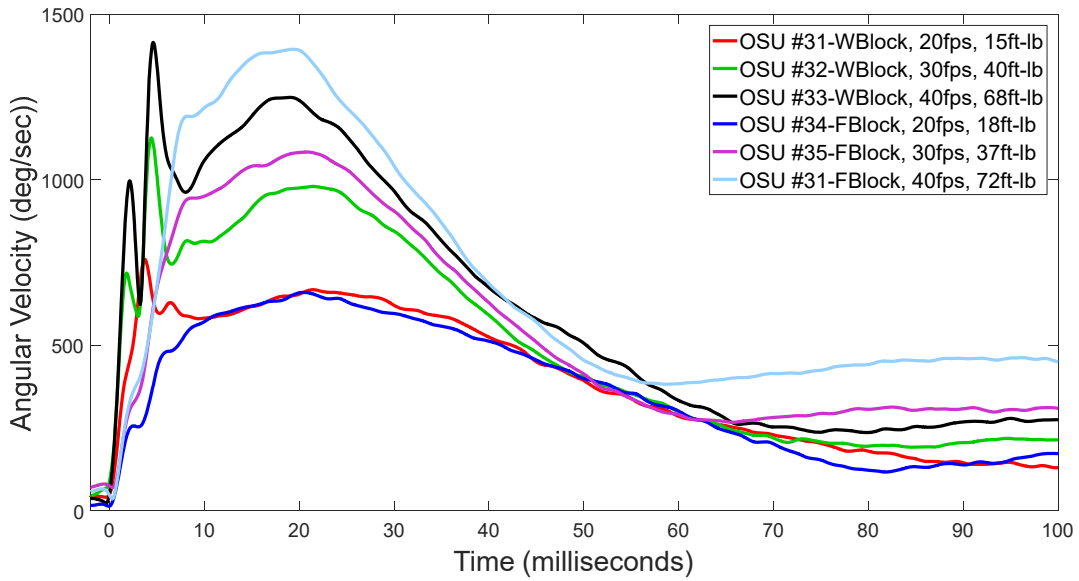


Figure 59 – Head resultant angular velocity time histories in 0-degree, wood & foam block side impact scenarios

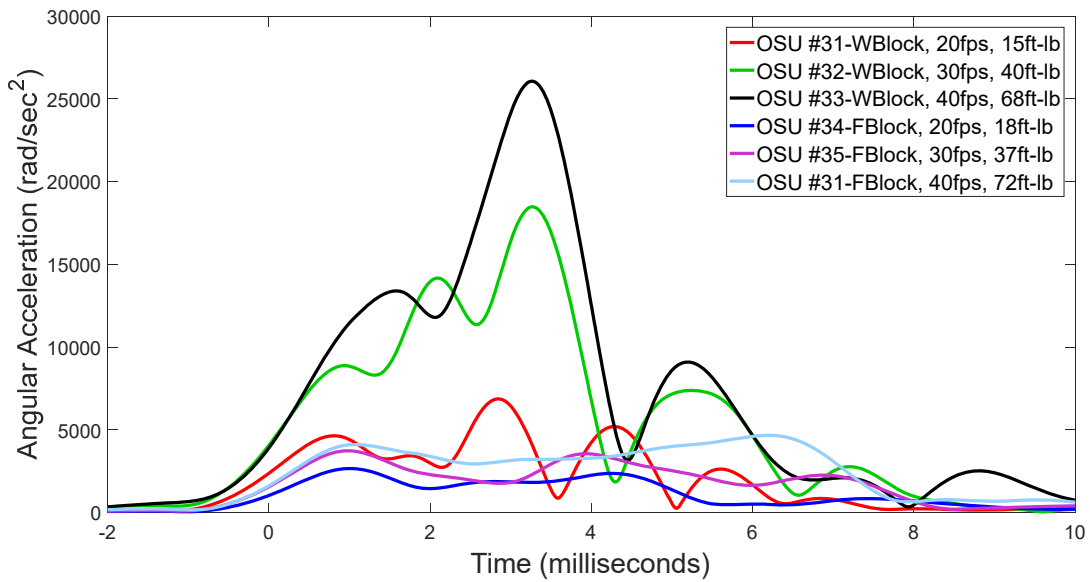


Figure 60 – Head resultant angular acceleration time histories in 0-degree, wood & foam block side impact scenarios

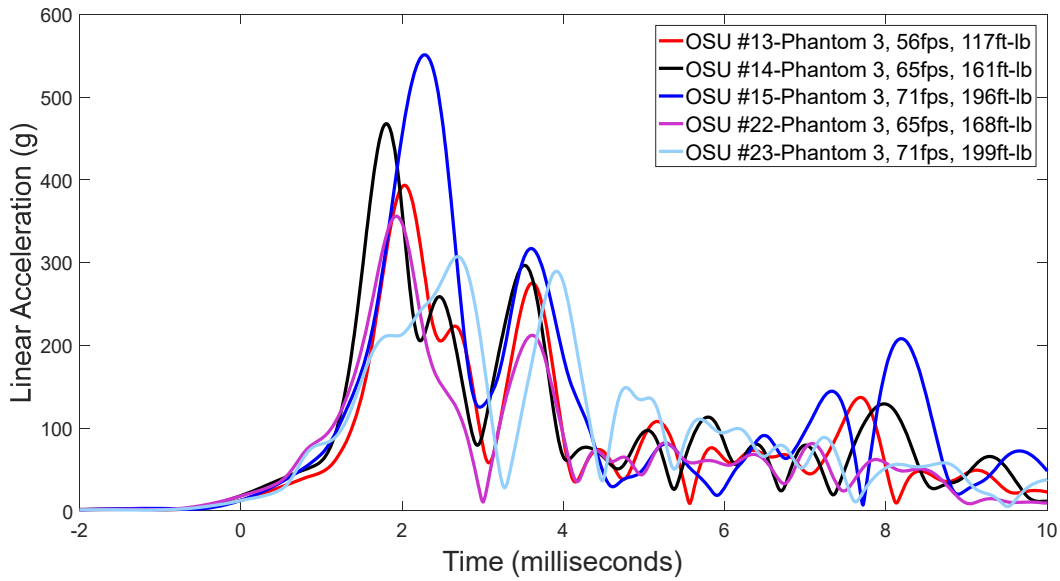


Figure 61 – Head resultant linear acceleration time histories in 90-degree, Phantom 3, top impact scenarios

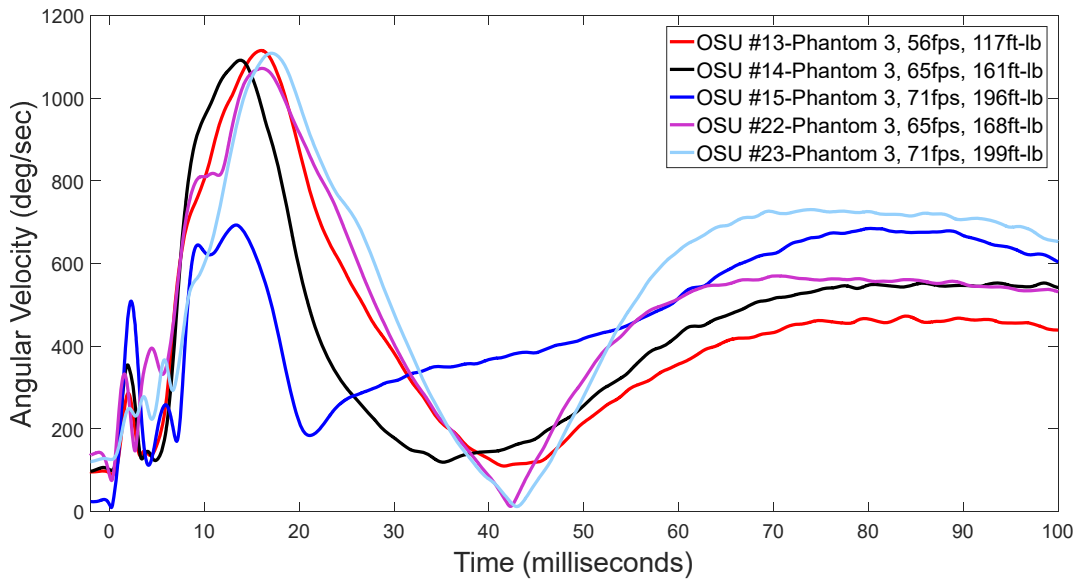


Figure 62 – Head resultant angular velocity time histories in 90-degree, Phantom 3, top impact scenarios

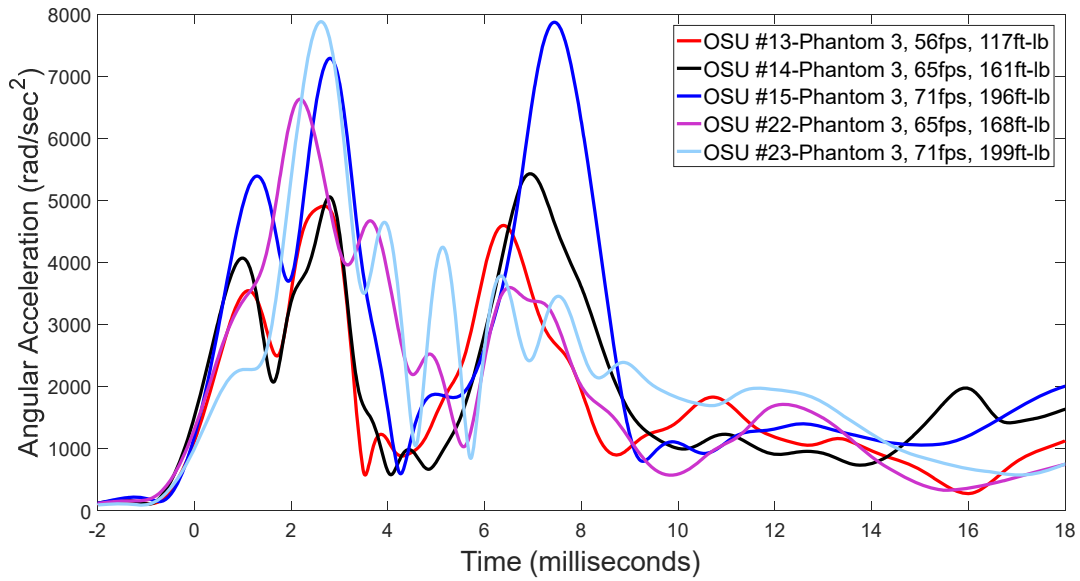


Figure 63 – Head resultant angular acceleration time histories in 90-degree, Phantom 3, top impact scenarios

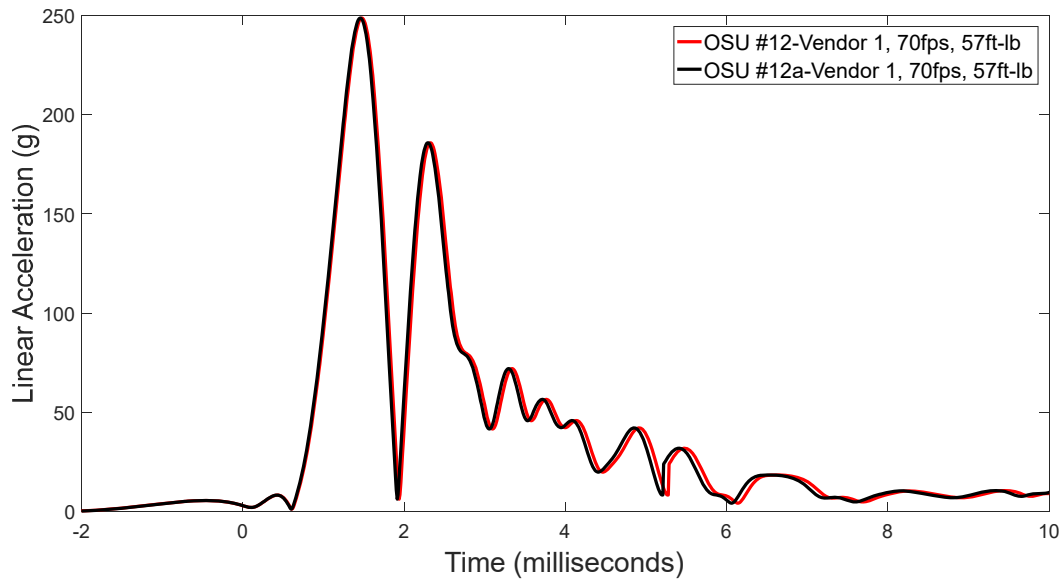


Figure 64 – Head resultant linear acceleration time histories in 90-degree, Vendor 1, top impact scenarios

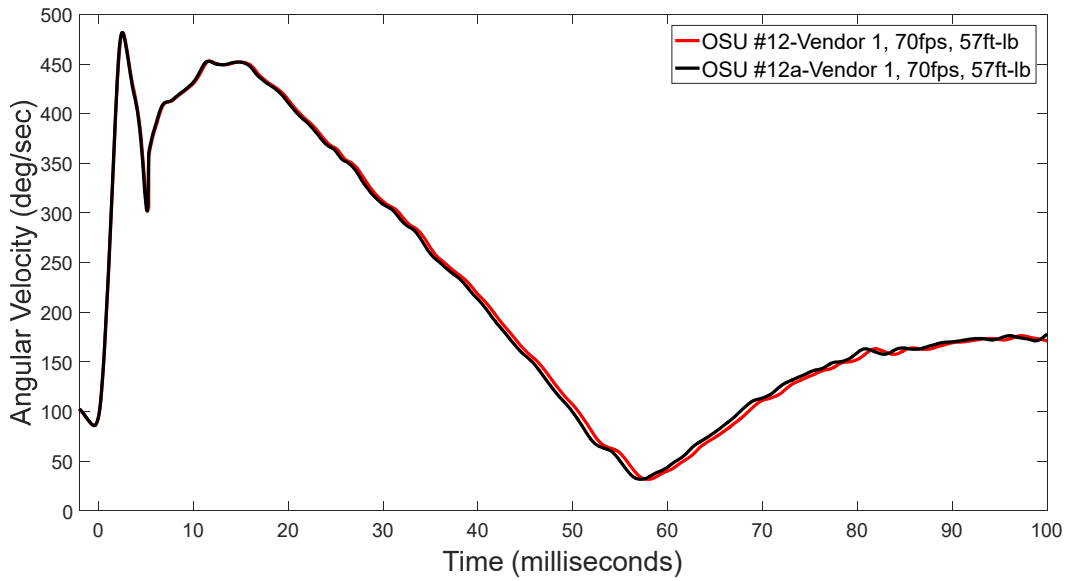


Figure 65 – Head resultant angular velocity time histories in 90-degree, Vendor 1, top impact scenarios

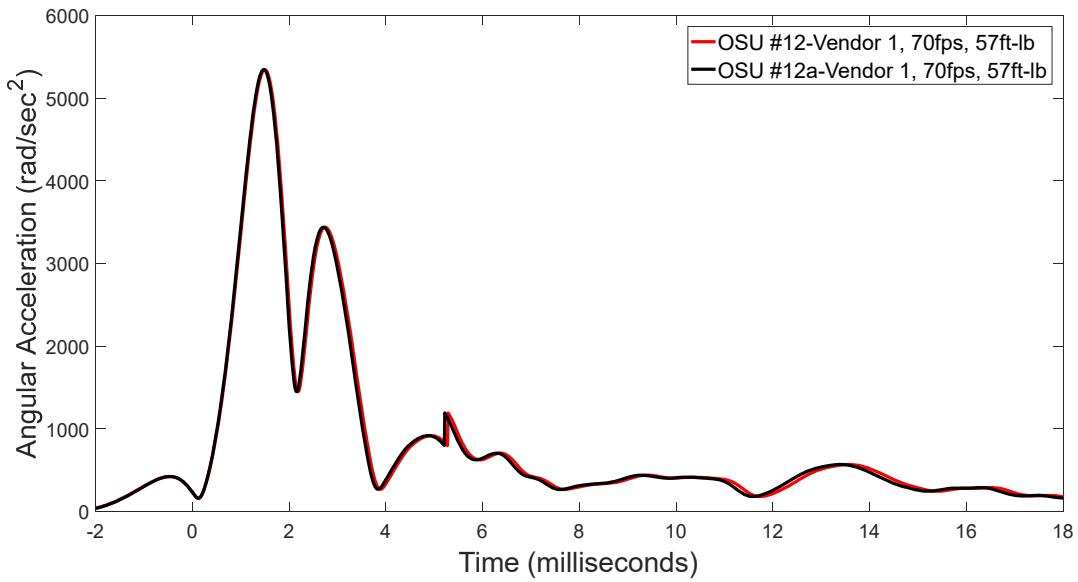


Figure 66 – Head resultant angular acceleration time histories in 90-degree, Vendor 1, top impact scenarios

APPENDIX C—UAS IMPACT ORIENTATION ANGLES

Table 12 – Change in UAS orientation between its release from the launcher and impact

| PMHS # | Test ID | Test Article | Impact Angle | Impact Location | Target Impact Speed (ft/s) | Δ Roll Angle (°) | Δ Pitch Angle (°) | Δ Yaw Angle (°) |
|--------|----------|----------------|--------------|-----------------|----------------------------|-------------------------|--------------------------|------------------------|
| 02 | OSU #2 | DJI Phantom 3 | 0 | Right Side | 56 | 4.9 | 3.6 | -3.6 |
| | OSU #3 | DJI Phantom 3 | 0 | Right Side | 61 | 0.6 | -1.1 | -1.0 |
| | OSU #4 | DJI Phantom 3 | 0 | Right Side | 71 | -2.4 | 0.3 | -4.3 |
| | OSU #6 | DJI Phantom 3 | 58 | Front | 56 | -1.4 | 2.1 | -0.4 |
| | OSU #7 | DJI Phantom 3 | 58 | Front | 61 | 0.2 | 3.1 | 1.0 |
| | OSU #8a | DJI Phantom 3 | 58 | Front | 61 | -0.6 | 5.3 | 1.4 |
| | OSU #9 | DJI Phantom 3 | 58 | Front | 71 | -1.8 | 8.6 | 2.4 |
| | OSU #10 | DJI Phantom 3 | 58 | Right Side | 61 | 0.2 | -0.3 | -0.7 |
| | OSU #11a | DJI Phantom 3 | 58 | Right Side | 71 | 0.5 | -0.1 | -1.2 |
| | OSU #13 | DJI Phantom 3 | 90 | Top | 56 | 0.0 | -2.3 | 0.1 |
| | OSU #14 | DJI Phantom 3 | 90 | Top | 65 | -0.8 | 0.3 | -0.6 |
| | OSU #15 | DJI Phantom 3 | 90 | Top | 71 | -0.7 | 0.8 | -0.8 |
| | OSU #16a | DJI Phantom 3 | 58 | Right Side | 61 | -0.2 | -0.2 | -2.8 |
| | OSU #17 | DJI Phantom 3 | 58 | Right Side | 71 | -0.4 | 1.0 | -2.8 |
| | OSU #19 | DJI Phantom 3 | 58 | Front | 71 | -0.4 | -5.7 | -1.4 |
| 03 | OSU #20 | DJI Mavic Pro | 58 | Front | 61 | 1.0 | 0.6 | -0.1 |
| | OSU #21 | DJI Mavic Pro | 58 | Front | 71 | 1.2 | -0.3 | -0.7 |
| | OSU #22 | DJI Phantom 3 | 90 | Top | 65 | -0.8 | 0.6 | -0.5 |
| | OSU #23 | DJI Phantom 3 | 90 | Top | 71 | 0.4 | -1.0 | -0.8 |
| | OSU #24 | Sensefly eBee+ | 0 | Right Side | 64 | 0.4 | 0.7 | -1.9 |
| 04 | OSU #25 | Sensefly eBee+ | 0 | Right Side | 71 | 0.5 | -0.2 | -2.6 |
| | OSU #30 | DJI Inspire 2* | 0 | Right Side | 30 | -2.6 | 5.7 | -3.7 |
| | OSU #26 | Sensefly eBee+ | 58 | Left Side | 64 | -0.2 | 0.2 | -0.3 |
| | OSU #27 | Sensefly eBee+ | 58 | Left Side | 71 | 0.5 | 0.1 | 0.2 |
| | OSU #27a | Sensefly eBee+ | 58 | Left Side | 71 | 0.3 | 0.0 | -0.1 |
| | OSU #28 | DJI Mavic Pro | 58 | Front | 61 | 2.4 | -1.1 | 0.9 |
| | OSU #29 | DJI Mavic Pro | 58 | Front | 71 | 1.3 | 1.4 | -6.0 |

APPENDIX D— FARO MEASUREMENT LOCATIONS

| # | Point Description |
|----|---|
| 1 | Vicon Reference Point - Chair Top L - Point 1 |
| 2 | Vicon Reference Point - Chair Top L - Point 2 |
| 3 | Vicon Reference Point - Chair Top L - Point 3 |
| 4 | Vicon Reference Point - Chair Top L - Point 4 |
| 5 | Vicon Reference Point - Chair Mid L - Point 1 |
| 6 | Vicon Reference Point - Chair Mid L - Point 2 |
| 7 | Vicon Reference Point - Chair Mid L - Point 3 |
| 8 | Vicon Reference Point - Chair Mid L - Point 4 |
| 9 | Vicon Reference Point - Chair Top R - Point 1 |
| 10 | Vicon Reference Point - Chair Top R - Point 2 |
| 11 | Vicon Reference Point - Chair Top R - Point 3 |
| 12 | Vicon Reference Point - Chair Top R - Point 4 |
| 13 | Vicon Reference Point - Chair Mid R - Point 1 |
| 14 | Vicon Reference Point - Chair Mid R - Point 2 |
| 15 | Vicon Reference Point - Chair Mid R - Point 3 |
| 16 | Vicon Reference Point - Chair Mid R - Point 4 |
| 17 | Skull Vertex |
| 18 | Left Infraorbital Notch |
| 19 | Right Infraorbital Notch |
| 20 | Right Tragon |
| 21 | Left Tragon |
| 22 | Tetrahedron Vertex |
| 23 | Tetrahedron-Face 1, Point 1 |
| 24 | Tetrahedron-Face 1, Point 2 (CW) |
| 25 | Tetrahedron-Face 1, Point 3 (CW) |
| 26 | Tetrahedron - Corner 1 2 |
| 27 | Tetrahedron-Face 2, Point 1 |
| 28 | Tetrahedron-Face 2, Point 2 (CW) |
| 29 | Tetrahedron-Face 2, Point 3 (CW) |
| 30 | Tetrahedron - Corner 2 3 |
| 31 | Tetrahedron-Face 3, Point 1 |
| 32 | Tetrahedron-Face 3, Point 2 (CW) |
| 33 | Tetrahedron-Face 3, Point 3 (CW) |
| 34 | Tetrahedron - Corner 1 3 |
| 35 | Head 6DX: +1 Normal Plane (CCW) Point 1 |
| 36 | Head 6DX: +1 Normal Plane (CCW) Point 2 |
| 37 | Head 6DX: +1 Normal Plane (CCW) Point 3 |
| 38 | Head 6DX: +2 Normal Plane (CCW) Point 1 |

| # | Point Description |
|----|---|
| 39 | Head 6DX: +2 Normal Plane (CCW) Point 2 |
| 40 | Head 6DX: +2 Normal Plane (CCW) Point 3 |
| 41 | Head 6DX: -3 Normal Plane (CCW) Point 1 |
| 42 | Head 6DX: -3 Normal Plane (CCW) Point 2 |
| 43 | Head 6DX: -3 Normal Plane (CCW) Point 3 |
| 44 | Head 6DX: Center |
| 45 | Right Frontal Bone Strain Gage |
| 46 | Left Frontal Bone Strain Gage |
| 47 | Mid Frontal Bone Strain Gage |
| 48 | Right Parietal Bone Strain Gage |
| 49 | Left Parietal Bone Strain Gage |
| 50 | Head Impact Location (Approximate) |
| 51 | Left Acromion |
| 52 | Right Acromion |
| 53 | Midline of Axilla Strap - Midsagittal |
| 54 | Midline of Axilla Strap - Right |
| 55 | Midline of Axilla Strap - Left |
| 56 | Midline of Knee Strap - Midsagittal |
| 57 | Midline of Knee Strap - Right |
| 58 | Midline of Knee Strap - Left |
| 59 | Left Greater Trochanter |
| 60 | Left Patella |
| 61 | Right Greater Trochanter |
| 62 | Right Patella |
| 63 | Right Back Support 1 (most inferior) |
| 64 | Right Back Support 2 |
| 65 | Right Back Support 3 |
| 66 | Left Back Support 1 (most inferior) |
| 67 | Left Back Support 2 |
| 68 | Left Back Support 3 |
| 69 | Catapult Track Right Edge 1 |
| 70 | Catapult Track Right Edge 2 |
| 71 | Catapult Track Right Edge 3 |